ANALYTIC AND NUMERICAL STUDY OF UNDERWATER IMPLOSION

by

Lynn Andrew Gish

B.S., United States Naval Academy (1993)
M.M.E, Catholic University of America (1994)
S.M., Massachusetts Institute of Technology (2004)
Naval Engineer, Massachusetts Institute of Technology (2004)

Submitted to the Department of Mechanical Engineering
in partial fulfillment of the requirements for the degree of

Doctor of Philosophy in the field of Ocean Engineering

at the

MASSACHUSETTS INSTITUTE OF TECHNOLOGY

June 2013

Author .....
Department of Mechanical Engineering
May 20, 2013

Certified by .....
Tomasz Wierzbicki
Professor of Applied Mechanics
Thesis Supervisor

Accepted by .....
David E. Hardt
Chairman, Department Committee on Graduate Students

ANALYTIC AND NUMERICAL STUDY OF UNDERWATER IMPLOSION

by

Lynn Andrew Gish

Submitted to the Department of Mechanical Engineering
on May 20, 2013, in partial fulfillment of the
requirements for the degree of
Doctor of Philosophy in the field of Ocean Engineering

Abstract

Underwater implosion, the rapid collapse of a structure caused by external pressure, generates a pressure pulse in the surrounding water that is potentially damaging to adjacent structures or personnel. Understanding the mechanics of implosion, specifically the energy transmitted in the pressure pulse, is critical to the safe and efficient design of underwater structures. Hydrostatically-induced implosion of unstiffened metallic cylinders was studied both analytically and numerically. An energy balance approach was used, based on the principle of virtual velocities. Semi-analytic solutions were developed for plastic energy dissipation of a symmetric mode 2 collapse; results agree with numerical simulations within 10%. A novel pseudo-coupled fluid-structure interaction method was developed to predict the energy transmitted in the implosion pulse; results agree with fully-coupled numerical simulations within 6%. The method provides a practical alternative to computationally-expensive simulations when a minimal reduction in accuracy is acceptable. Three design recommendations to reduce the severity of implosion are presented: (1) increase the structure's internal energy dissipation by triggering higher collapse modes, (2) initially pressurize the internals of the structure, and (3) line the cylinder with a flexible or energy absorbing material to cushion the impact between the structure's imploding walls. These recommendations may be used singly or in combination to reduce or completely eliminate the implosion pulse. However, any design efforts to reduce implosion severity must be part of the overall system design, since they may have detrimental effects on other performance areas like strength or survivability.

Thesis Supervisor: Tomasz Wierzbicki
Title: Professor of Applied Mechanics

Acknowledgments

First and foremost, I thank God, the source of all wisdom and knowledge, for giving me the amazing opportunity to pursue this research. I sincerely pray that this work, and all I do, will be glorifying to Him.

I wish to thank my advisor, Professor Tom Wierzbicki, for his guidance, direction, and encouragement throughout this project. He willingly took on this project even though it was outside his primary area of focus at the time. His technical insight and straight-forward approach to problem solving were critical to the success of this work. I was very fortunate to have an advisor so accessible, helpful, and fun to work with.

I also acknowledge and thank my other advisors and members of my thesis committee. CAPT Mark Thomas, USN, provided a practical and critical Navy perspective to everything I did, and helped keep my work grounded on the real-world problem. Dr. Yuming Liu provided expert insight and advice into the fluid-structure interaction aspects of the project, and was a very helpful and valuable resource.

The general idea for this research was first proposed by Dr. Stephen Turner, Naval Undersea Warfare Center and Office of Naval Research. I thank Steve for his technical guidance on the subject of implosion, and for allowing me the opportunity to participate in the semi-annual ONR Implosion Program Reviews. These meetings were essential to my understanding of the problem and to developing contacts in the field. I also acknowledge and thank Dr. Joe Ambrico, Dr. Emily Guzas, and Dr. Ryan Chamberlin (Naval Undersea Warfare Center) for their assistance with my work and the data they provided.

Finally, to my wife Michele, thanks for your constant support, encouragement, and love throughout this endeavor. I can't imagine doing this without you. And to our wonderful children, Casey and Drew, thanks for giving Daddy enough time off from playing to finish his work.

The fear of the Lord is the beginning of knowledge,
but fools despise wisdom and instruction.
-Proverbs 1:7

Contents

List of Figures

List of Tables

Nomenclature

$()_0$	initial value of ()
$()_f$	final value of ()
$()_n$	value of () at step n
α	angular DOF for Phase 1
α_f	value of α at end of Phase 1
δ	transverse displacement of point on center cross-section
$\Delta()$	change from initial state to final state
γ	ratio of specific heats
$\kappa_{\alpha\beta}$	curvature tensor
$\nabla()$	gradient of ()
ν	kinematic viscosity
ϕ	fluid potential
ρ	fluid density
ρ_s	cylinder material density
σ_0	energy-equivalent flow stress

σ_θ hoop stress

σ_{ij} stress tensor

σ_x longitudinal stress

θ circumferential coordinate

ε_0 yield strain

ε_{ij} strain tensor

ε_p plastic strain

ζ half-length of the center flattened section of the cylinder during Phase 2 and 3

ζ_2 half-length of flattened section during Phase 2

$\bar{\zeta_2}$ dimensionless half-length of flattened section during Phase 2

ζ_3 half-length of rectangular flattened section during Phase 3

$\bar{\zeta_3}$ dimensionless half-length of rectangular flattened section during Phase 3

A cross-sectional area

b half-width of the flattened portion of the ring during Phase 2 and 3

b_0 half-width of flattened center cross-section

$\bar{b_0}$ dimensionless half-width of flattened center cross-section

c speed of sound in water

D cylinder diameter

E_{air} energy required to compress internal air

E_b bending energy

E_{dyn} D'Alembert inertial energy

E_{ext} external work

E_{int} internal plastic energy dissipation

E_m membrane energy

E_{pulse} energy released in the implosion pulse

E_p strain hardening modulus

h cylinder thickness

I acoustic intensity

KE kinetic energy

L cylinder half-length

m mass per unit area of solid cylinder

M_0 fully plastic bending moment per unit length

$M_{\alpha\beta}$ bending moment tensor

$m_{\alpha\beta}$ dimensionless bending moment tensor

m_a fluid added mass per unit area

N_0 fully plastic membrane force per unit length

$N_{\alpha\beta}$ membrane force tensor

$n_{\alpha\beta}$ dimensionless membrane force tensor

p pressure

p_c critical pressure of the cylinder

p_d dynamic fluid pressure

p_{excess} excess pressure that causes acceleration of cylinder surface

p_{exp} peak pressure from explosive loading

p_{hyd} hydrostatic pressure

p_i internal gas pressure

p_{prop} propagation pressure

R cylinder radius

r variable radius segment of moving hinge model

R_{ref} radius (offset) of pressure measurement location

Re Reynold's number

t time

u axial displacement

V volume

v speed of moving plastic hinge

w_0 transverse displacement of leading generator at center cross-section

w transverse displacement

$\dot{w}$ transverse velocity

$\ddot{w}$ transverse acceleration

x longitudinal (axial) coordinate

Chapter 1

Introduction

1.1 Background and History

Underwater implosion refers to the rapid collapse of a solid structural shell resulting from fluid loading. Implosion occurs when the hydrostatic pressure exceeds the critical buckling pressure of the structure, or through a combination of hydrostatic pressure less than critical buckling pressure and a triggering event, such as an underwater explosive load (UNDEX). The duration of a typical implosion event is on the order of milliseconds. Implosion of a structure generates a pressure pulse in the surrounding water, similar to the pressure pulse created by the collapse of a gas bubble from an UNDEX event. Figure 1-1 shows a typical implosion dynamic pressure history, as measured at a point in the surrounding fluid.

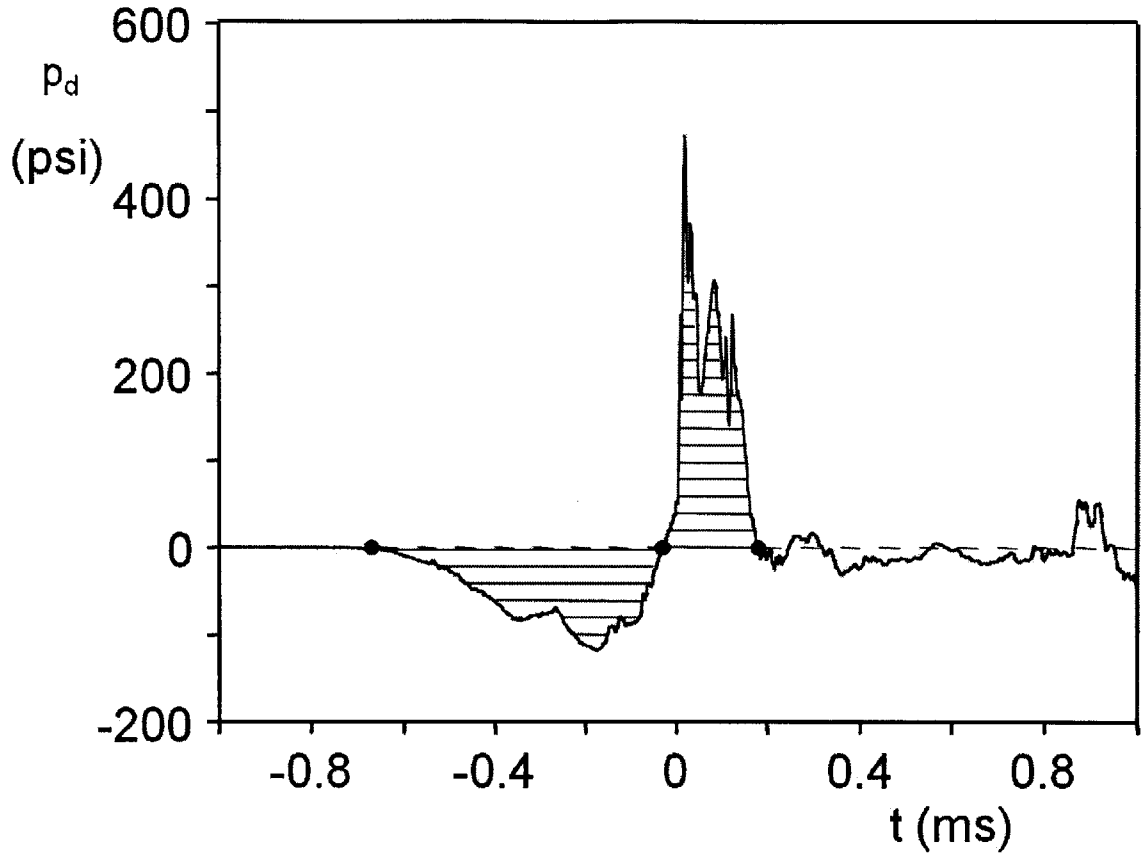

Figure 1-1: Typical dynamic pressure history for an underwater implosion event.

The negative phase represents the decrease in pressure due to the collapsing cylinder walls and the associated in-rushing water. The large positive spike is caused by the rapid deceleration (and subsequent compression) of the water when the structure reaches its maximum collapse and stops moving. The primary impetus for studying underwater implosion is the damaging effect that this implosion pressure pulse may have on an adjacent structure, such as a submarine hull. A related concern is the safety of personnel, particularly divers, who may be directly exposed to an implosion pressure pulse.

The study of underwater implosion began with Lord Rayleigh's study of collapsing spherical bubbles in 1917 [6]. In the 1950s, imploding glass spheres were considered for use as deep-ocean sound sources. Isaacs, in 1952, proposed an oceanographic signaling device that would mechanically implode a glass sphere when it reached the ocean bottom [7]. Implosion was seen as a safer, more convenient alternative to explosion for creating underwater signaling devices. Urick was the first to attempt to quantify the pressure pulse resulting from implosion [8]. He imploded a number of sealed air-filled glass bottles, ranging in size from 4 oz. to 1 gallon, at depths of 500-7500 ft, and recorded the resulting pressure signals with a single hydrophone suspended at a depth of 50 ft. Urick calculated the acoustic energy transmitted in the implosion pressure pulses, and concluded that the transmitted energy was a very small fraction ($\approx 0.2\%$) of the total available potential energy in a gas cavity of volume V and pressure p[1]. Furthermore, he observed that the energy transmitted in an implosion pulse was significantly less than that of an oscillating gas bubble of equivalent size. This observation indicated that a significant amount of energy is absorbed by the deformation and fracture of the glass bottle.

Price and Shuler [1] reported pressure-time history and energy density spectra

[1]Urick calculated the available potential energy in a gas cavity as $\frac{pV}{(\gamma-1)}$, where γ is the ratio of specific heats for the enclosed gas (1.4 for air).

data from at-sea implosion experiments with steel cylinders ranging from 8-30 inch diameter. The pressure-time histories show a negative pressure phase corresponding to the cylinder surface accelerating away from the water (i.e., collapsing), followed by a positive pressure phase corresponding to the cylinder surface accelerating toward the water (or equivalently, the surface coming to rest and the water decelerating against it). The sharp positive pressure spike corresponds generally to the moment of contact between the two sides of the cylinder. Whereas Urick observed oscillations in the pressure signal from his imploding glass bottles very similar to the bubble pulses from an explosion, Price observed that cylindrical implosions generally exhibit only a single negative and positive pressure phase (see Fig. 1-2). He concluded that the oscillation decreases as the ratio of structure to volume of enclosed air increases. Price also experimented with cylinders with multiple compartments and different materials. His data provides an important insight into implosion of cylinders, and the effect of features like bulkheads and stiffeners.

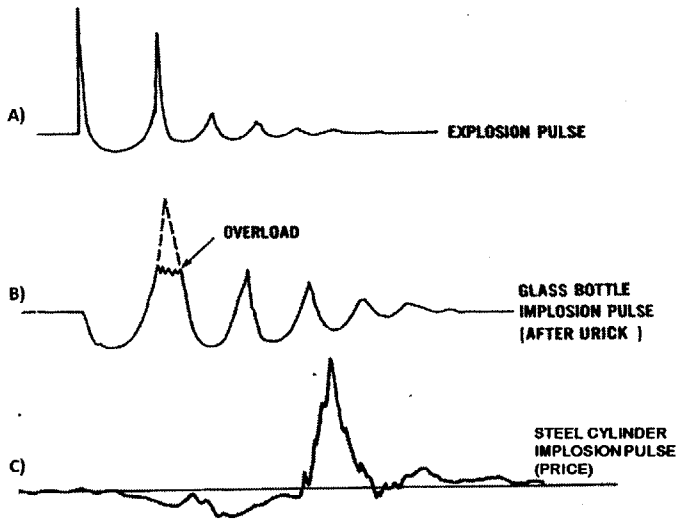

Figure 1-2: Comparison of explosion, glass bottle implosion, and steel cylinder implosion pressure pulses. Cylinder does not exhibit repeated oscillations [1].

Underwater implosion has been known to cause a cascade of secondary implosions. The most dramatic example of this phenomenon occurred in November 2001 at the Super-Kamiokande Cherenkov detector facility in Japan. The facility utilized 11,146 50 cm diameter photomultiplier tubes (PMTs), submerged in a 42 m deep tank of water. During routine refilling operations, a single PMT imploded due to hydrostatic pressure. The resulting pressure pulse caused a cascade of secondary implosions that destroyed 6777 PMTs [2, 9]. This costly incident has heightened the interest in underwater implosion and the resulting pressure pulse.

Closely related to the problem of underwater implosion is the problem of buckling in submarine pipelines. This problem was studied extensively, starting with Palmer and Martin in 1975 [5]. They calculated the quasistatic propagation pressure for a pipeline using an energy balance between strain energy in the pipe and work done by external pressure. The resulting expression for propagation pressure was:

$$p_{prop} = \pi \sigma_0 \left(\frac{h}{D}\right)^2 \tag{1.1}$$

where σ_0 is the flow stress of the material, h is the cylinder thickness, and D is the cylinder diameter.

Palmer and Martin also proposed a simple kinematic model of plastic ring deformation consisting of four stationary plastic hinges and four rigid quarter circle segments (Fig. 1-3). Their calculations assumed a rigid-perfectly plastic material and included only bending energy and not membrane energy; thus, they underestimate the propagation pressure.

Wierzbicki and Bhat [10] expanded on Palmer and Martin's work by developing a simple moving plastic hinge ring deformation model, shown in Fig. 1-4.

They also incorporated a rigid-linear strain hardening material model. Their

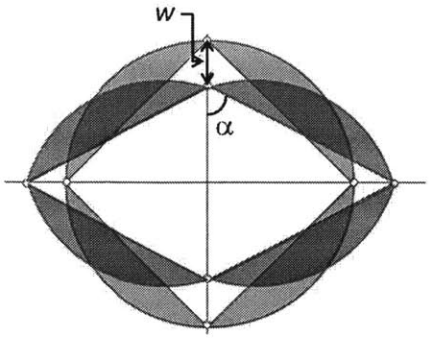

Figure 1-3: Palmer and Martin's stationary hinge ring model.

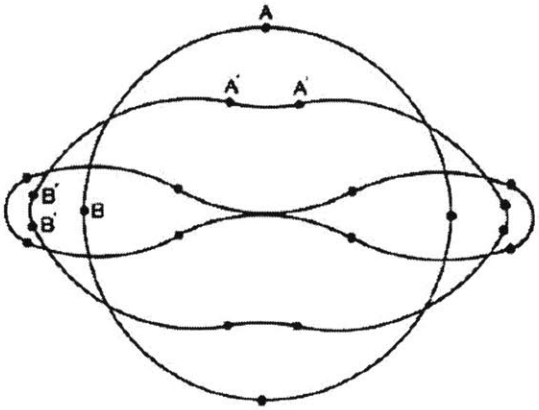

Figure 1-4: Wierzicki and Bhat's traveling hinge ring model.

resulting expression for propagation pressure was:

$$p_{prop} = \left\{ 3 + 12 \left(\frac{E_p h}{3\sigma_0 D} \right)^{0.7} \right\} \sigma_0 \left(\frac{h}{D} \right)^2 \tag{1.2}$$

where E_p is the strain hardening modulus. Kyriakides, et al., [11] also studied the problem of propagating buckles extensively, and conducted numerous experiments to validate the analytic results.

Suh and Wierzbicki [4] investigated plastic deformation of metallic cylinders subjected to combined loading (lateral indentation, bending moment, and axial force). They developed a string-on-foundation model that accurately describes the deformation of a cylinder and is mathematically simplified enough to be used in analytic

solutions. Section 2.2 describes the string-on-foundation model, which will be used as the basis for analytic solutions in this research. Suh and Wierzbicki assumed a rigid perfectly plastic material model, and used the principal of virtual velocities as the basis for their solutions. They investigated a number of different boundary conditions on the cylinder ends, and concluded that the resistance of the tube to deformation is strongly dependent on the boundary conditions.

Hoo Fatt and Wierzbicki [12] and Hoo Fatt [13] studied the plastic response of cylinders under various dynamic loading conditions. Using similar methodology as Suh, they developed solutions for both unstiffened and ring-stiffened cylinders subjected to impact and impulsive loading. Hoo Fatt also introduced the concept of equivalent parameters (constants) using an averaging procedure in the circumferential direction to eliminate one spatial variable.

Current State of the Art

Most of the recent research directly related to underwater implosion has been driven by U.S. Navy interest. Cor and Miller [14, 15] studied spherical and cylindrical implodable volumes and the effect that energy absorption by internal structure has on the implosion pressure pulse. They concluded that internal structure can significantly reduce the implosion pressure pulse, and they identified future work very similar to the research reported in this thesis. However, Cor and Miller have not pursued their implosion work any further, leaving the problem of structural energy absorption during implosion unsolved.

Very few experimental studies of underwater implosion exist in the literature, largely because of a limited number of test facilities capable of conducting implosion tests. Turner [16] conducted implosion experiments on thin-walled glass spheres and demonstrated that the structural failure mode and time history have a significant effect on an implosion pressure pulse. Diwan, et al., [2] measured the shock wave

(implosion pulse) resulting from the hydrostatically-induced implosion of a PMT, and compared the results to numerical simulations. The implosion experiments reported in both these papers were conducted in the test facility at the Naval Undersea Warfare Center (NUWC) in Newport, RI, shown in Fig. 1-5 below.

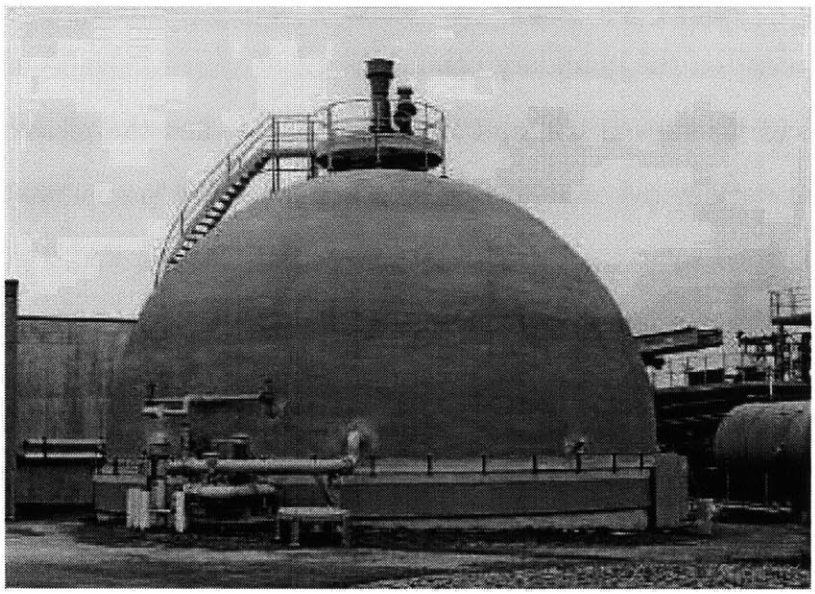

Figure 1-5: Propulsion Noise Test System (PNTS) at the Naval Undersea Warfare Center (NUWC) in Newport, RI [2].

Numerous authors (e.g., Brett and Yiannakopolous [17] and Hung, et al., [18]) have studied and reported UNDEX effects on cylindrical structures. However, the impetus for their work is understanding the direct effects of UNDEX rather than subsequent implosion. In most of the literature, the loading conditions (UNDEX and hydrostatic pressure combined) were such that the cylinder did not fully implode. Very little, if any, literature has been published on UNDEX-initiated implosion and the subsequent implosion pressure pulse.

General Implosion Mechanics

Under purely hydrostatic loading, a metallic cylindrical structure tends to buckle and implode in a symmetric fashion into one of several possible mode shapes, as shown

in Fig. 1-6 below.

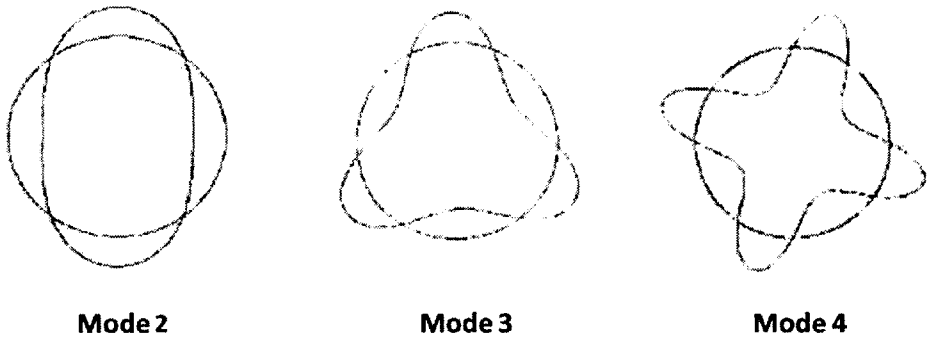

Figure 1-6: Symmetric collapse modes under purely hydrostatic loading.

The buckling mode of a cylinder subjected to hydrostatic pressure is determined by the cylinder's length (2L), diameter (D), and thickness (h), in accordance with classical elastic-plastic buckling theory. Cylinders with large 2L/D ($>\sim 5$) collapse in mode 2, while lower 2L/D collapse into mode 3 or 4[3]. Fracture may or may not occur during the implosion process, depending on material parameters, shell thickness, loading, boundary conditions, etc. Figure 1-7 shows photos of representative test samples illustrating the different collapse modes.

(a) Mode 2.

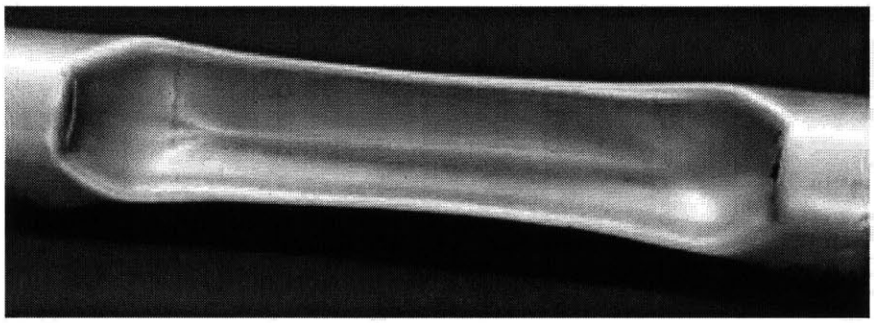

(b) Mode 3.

(c) Mode 4.

Figure 1-7: Representative test samples illustrating different collapse modes [3].

If hydrostatic loading is combined with UNDEX, the implosion process becomes more complex. UNDEX itself is a complicated process, consisting of an initial shock wave followed by multiple bubble pulse pressure loadings. Underwater Explosions, by R.H. Cole [19], is the definitive reference on UNDEX. A representative pressure-time history from an UNDEX event is shown in Fig. 1-2(A). The response of an implodable volume subjected to UNDEX depends on many parameters, including explosive charge size, standoff distance, hydrostatic pressure, and orientation of the structure relative to the charge. The structure may implode due to the initial shock loading, or due to one of the bubble pulses. Implosions triggered by UNDEX tend to exhibit asymmetric collapse modes, often accompanied by significant fracture. Because of the complexities involved in UNDEX-initiated implosion, this work focuses solely on hydrostatically-induced implosion.

1.2 General Description of Fluid-Structure Interaction Problems

Underwater implosion is a fluid-structure interaction problem. Fluid-structure interaction (FSI) problems are a broad class of problems involving both solid and fluid mechanics. A general FSI problem consists of an elastic or elastic-plastic solid body either surrounded by a fluid or surrounding a fluid. The solid body may be rigid or deformable. The problem is solved by imposing continuity conditions at the fluid-solid interface. Specifically, kinematic continuity of displacement and velocity and kinetic continuity of normal stress must be imposed at the interface [20].

An FSI problem is further complicated if the solid body undergoes large transient deformations, as in the case of underwater implosion. In hydrostatically-induced implosion, the hydrostatic pressure loading on the solid body causes rapid movement of the solid surface (i.e., deformation or crushing of the body). This rapid movement

of the solid surface causes corresponding motion of the adjacent fluid (because of kinematic continuity requirements), which in turn causes a local hydrodynamic pressure change (decrease) in the fluid. The hydrodynamic pressure during the cylinder collapse is illustrated in Fig. 1-1. The changing fluid pressure acting on the solid surface changes the acceleration of the solid surface, which further changes the fluid velocity and pressure. In a typical underwater implosion, the entire collapse occurs in a few milliseconds. Thus, the implosion problem is a fully-coupled, highly dynamic and nonlinear problem.

In general, FSI problems are too complex to be solved analytically, so they are analyzed numerically. The general solution approach is to solve the equations governing fluid flow and solid displacement at each time step, while simultaneously imposing the continuity requirements. Extensive research has been done on optimizing numerical methods for solving FSI problems (e.g., [21, 22, 23]). Fully coupled numerical simulation of FSI problems is beyond the scope of the current research; rather, this work focuses on a pseudo-coupled analytic solution method.

1.3 U.S. Navy Involvement

Underwater implosion is of great interest to the U.S. Navy, primarily because of the danger that an implosion could pose to an adjacent submarine. Submarines carry a variety of devices and systems that could potentially implode. Examples include drydeck shelters (DDS) mounted externally to the submarine topside deck, unmanned underwater vehicles (UUVs) carried either external or internal to the submarine, and countermeasure devices (either external or internal). Figure 1-8 below shows photographs of implodables associated with Navy submarines. The implodables of interest to the Navy range in size from ≈ 0.001 m^3 to ≈ 10 m^3 outer envelope volume (5 orders of magnitude).

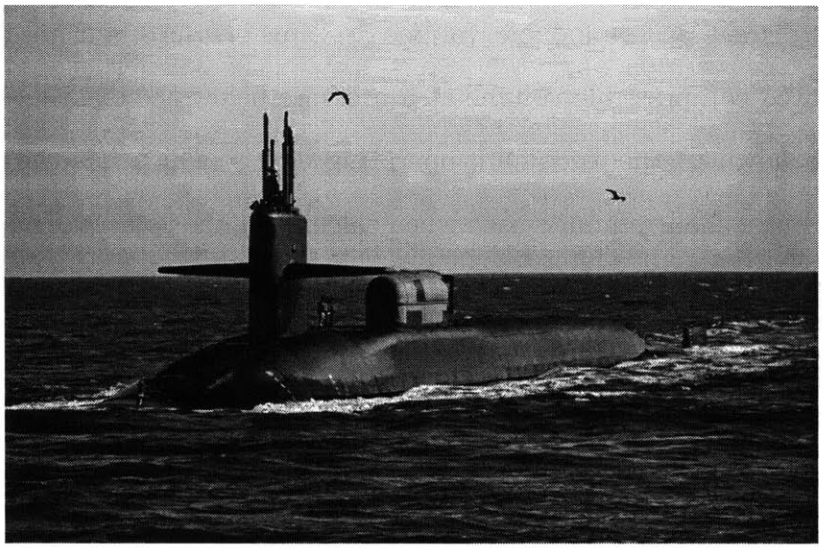

(a) Submarine with drydeck shelter (DDS). Approximate DDS volume is 10 m^3.

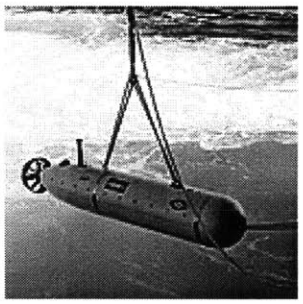

(b) Unmanned underwater vehicle (UUV). Approximate UUV volume is 0.5 m^3.

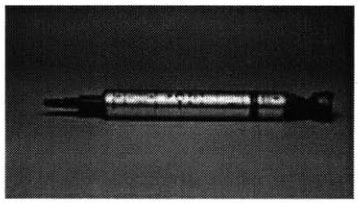

(c) Submarine-launched countermeasure device. Approximate countermeasure volume is 0.001 m^3.

Figure 1-8: Examples of implodables associated with U.S. Navy submarines.

The Navy defines an implodable volume as "any pressure housing containing a non-compensated compressible volume at a pressure below the external sea pressure (at any depth down to the maximum operating depth) which has the potential to collapse. The outer shell volume is used when calculating the volume of an implodable. Subtracting the volume of items internal to the implodable is not allowed. Externally mounted lights, gauges, bottles/flasks, spheres/tanks and beacons are examples of implodable items." [24].

The Navy uses a formal approval process for all implodable volumes to be carried aboard submarines. The current approval methodology calculates the maximum potential energy available from the complete structural collapse of the implodable volume, and assumes that all this energy will be transmitted into the water in the form of a pressure pulse. No allowance or adjustment is made for structure or material inside the implodable volume, or for energy absorbed by the structure during collapse. In reality, a significant fraction of the available energy will be absorbed by the structure during collapse. As such, the current methodology is very conservative and results in overestimating the energy (and corresponding damage effect) of the implosion pressure pulse. Subsequently, the implodable volumes must be structurally overdesigned to meet the current required safety standards.

The Navy sought to address this problem by organizing and funding a research program through the Office of Naval Research (ONR). The first step was creation of a Multi-University Research Initiative (MURI) to investigate certain aspects of the implosion problem such as small-scale laboratory testing, algorithm development, and fracture modeling. The MURI consisted of researchers from Stanford University, University of Texas at Austin, MIT, and Northwestern University. As part of the MURI, an implosion test facility was constructed at University of Texas at Austin, shown in Fig. 1-9 below.

In conjunction with the MURI, a Future Naval Capability (FNC) Implosion pro-

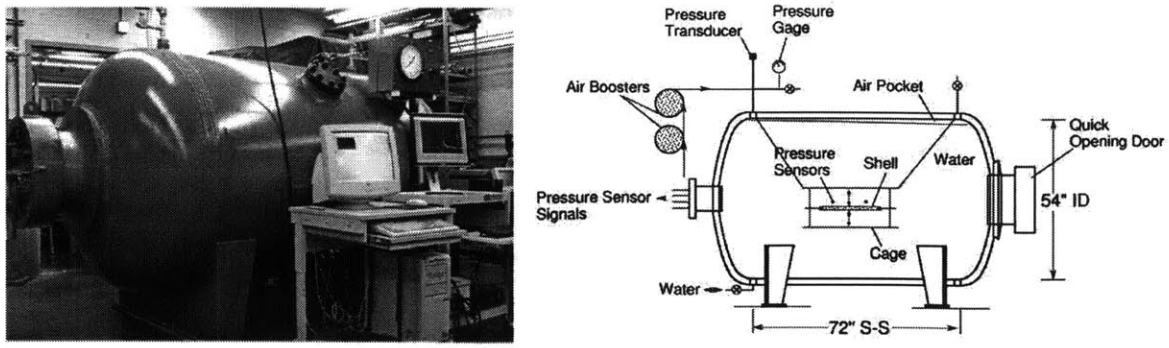

Figure 1-9: Implosion test facility at University of Texas at Austin [3].

gram was started. The FNC was a five-year (fiscal year 2008-2012), $18M program, and included development of a physics-based modeling tool, development of an implosion design and assessment tool, and full-scale at-sea implosion testing. The computational framework for the physics-based modeling tool, developed at Stanford, was published in the PhD thesis by Rallu [25]. Portions of the laboratory implosion experiments and numerical simulations were reported by Turner and Ambrico [26]. Figure 1-10 shows the configuration for one of the actual at-sea tests conducted as part of the FNC, an implodable cylinder attached to a larger host cylinder.

The present research is an extension of MIT's original involvement in the MURI. The current work seeks to address analytic questions not directly addressed by the MURI or FNC. The goal of this research is to obtain analytic solutions, validated with numerical simulations and experimental data, for the plastic strain energy absorbed by an unstiffened cylindrical structure during implosion. This solution will then be used to estimate the energy that may be transmitted in the form of a pressure pulse. The results will support more realistic, less conservative approval criteria for Navy implodable volumes.

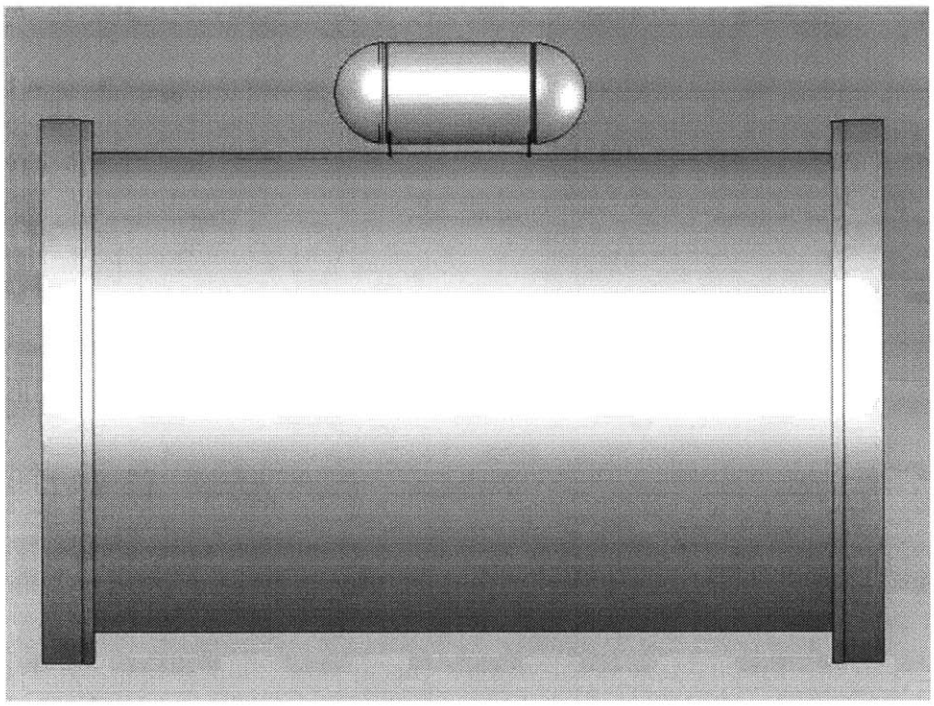

Figure 1-10: Implodable volume and host configuration for at-sea test.

1.4 Outline of Thesis

This thesis consists of 7 chapters. With the exception of Chapters 1 and 7, each chapter is self-contained and addresses one specific topic. Several chapters have been (or will be) submitted separately for publication. Chapter 1 provides background on underwater implosion and motivation for the current research. Chapter 2 describes the problem formulation and underlying assumptions in the solution methodologies. Chapter 3 describes the numerical simulations used to validate the analytic results. Chapter 4 contains derivations of the analytic solutions for plastic energy dissipation of an unstiffened cylinder during implosion. Chapter 5 presents a pseudo-coupled fluid-structure interaction solution method using an explicit time-stepping approach. Chapter 6 applies the knowledge from Chapters 4 and 5 to provide design recommendations for minimizing the implosion pulse of underwater structures. Finally, Chapter 7 summarizes the conclusions of this work and identifies future work related to underwater implosion.

Chapter 2

Problem Formulation and Simplifying Assumptions

This thesis deals primarily with hydrostatically-induced implosion of unstiffened metallic cylindrical shells. The cylinders have rigid flat endcaps. The hydrostatic pressure is assumed to be uniform over the entire surface of the cylinder (i.e., the difference in depth of one part of the cylinder compared to another is insignificant). The solutions apply to symmetric mode 2 collapse[1]. In all cases, the diameter-to-wall thickness ratio (D/h) is greater than 20. The standard thin-walled pressure vessel assumptions and equations of membrane theory apply:

$$\sigma_\theta = \frac{pR}{h} \tag{2.1}$$

$$\sigma_x = \frac{pR}{2h} \tag{2.2}$$

where σ_θ is hoop stress and σ_x is longitudinal stress in the undeformed cylinder. Figure 2-1 below shows the basic geometry, coordinate system, and notation used throughout this thesis.

[1]Experiments indicate that cylinders with length-to-diameter ratios ($2L/D = L/R$) greater than about 5 will collapse in mode 2[3]. Most real-world implodables fall into this category.

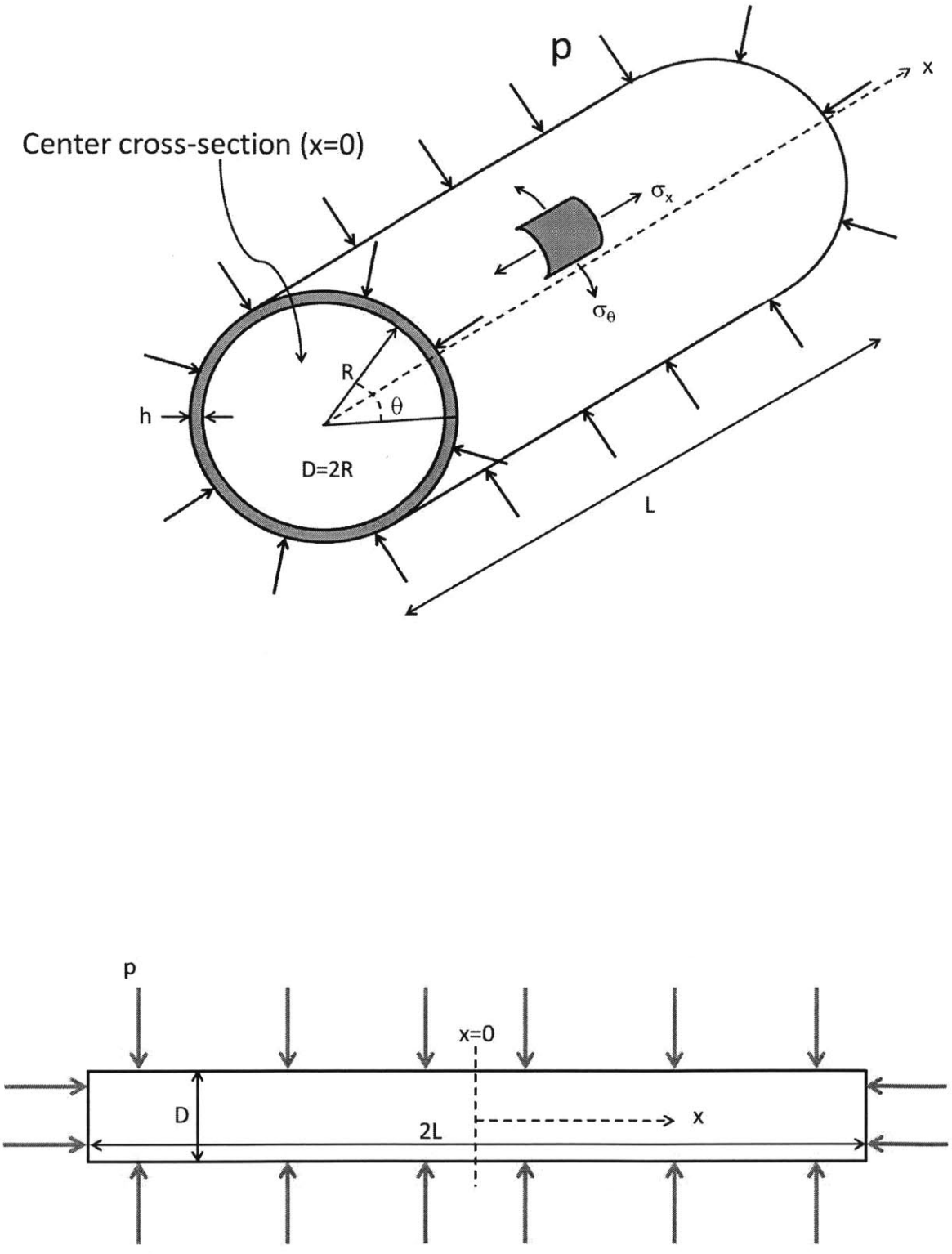

Figure 2-1: Geometry and loading of a cylindrical shell.

2.1 Equilibrium (Principle of Virtual Velocities)

The quasi-static global equilibrium for the problem of an imploding cylinder is expressed via the principle of virtual velocities:

$$\dot{E}_{ext} = \dot{E}_{int} \tag{2.3}$$

where $\dot{E}_{ext}$ is the rate of external work and $\dot{E}_{int}$ is the rate of internal plastic energy dissipation. For the case of purely hydrostatic loading, p, the left hand side of Eq. (2.3) is given by:

$$\dot{E}_{ext} = \int_S p\dot{w} dS \tag{2.4}$$

where S represents the entire cylinder surface and w is the normal displacement of the surface. In general, p may be a function of time and space. The expression for internal plastic energy dissipation is:

$$\dot{E}_{int} = h \int_S \sigma_{ij}\dot{\varepsilon}_{ij} dS \quad \text{(i,j=1,2,3)} \tag{2.5}$$

Because the cylinders are thin-walled, a plane stress state exists, and Eq. (2.5) can be rewritten as:

$$\dot{E}_{int} = \int_S \left(N_{\alpha\beta}\dot{\varepsilon}_{\alpha\beta} + M_{\alpha\beta}\dot{\kappa}_{\alpha\beta}\right) dS \quad (\alpha, \beta=1,2) \tag{2.6}$$

where $\dot{\varepsilon}_{\alpha\beta}$ and $\dot{\kappa}_{\alpha\beta}$ are the generalized strain and curvature rate tensors, and $N_{\alpha\beta}$ and $M_{\alpha\beta}$ are the corresponding membrane force and bending moment tensors. The first term on the right hand side of Eq. (2.6) represents membrane energy; the second term represents bending energy. Substituting the x-θ coordinate system from Fig.

2-1 for $\alpha\beta$ and expanding Eq. (2.6) gives:

$$\dot{E}_{int} = 2\int_0^L R\int_0^{2\pi} (N_{xx}\dot{\varepsilon}_{xx} + N_{\theta\theta}\dot{\varepsilon}_{\theta\theta} + 2N_{x\theta}\dot{\varepsilon}_{x\theta} + M_{xx}\dot{\kappa}_{xx} + M_{\theta\theta}\dot{\kappa}_{\theta\theta} + 2M_{x\theta}\dot{\kappa}_{x\theta})\, d\theta dx \tag{2.7}$$

2.2 Ring-Generator Model of Cylinder

The basic computational model of a cylindrical shell used in this work was first developed by Suh and Wierzbicki [4]. The cylinder is modeled as a series of unconnected rings or cross-sectional slices and a bundle of unconnected longitudinal generators. The rings and generators are loosely connected, as shown in Fig. 2-2.

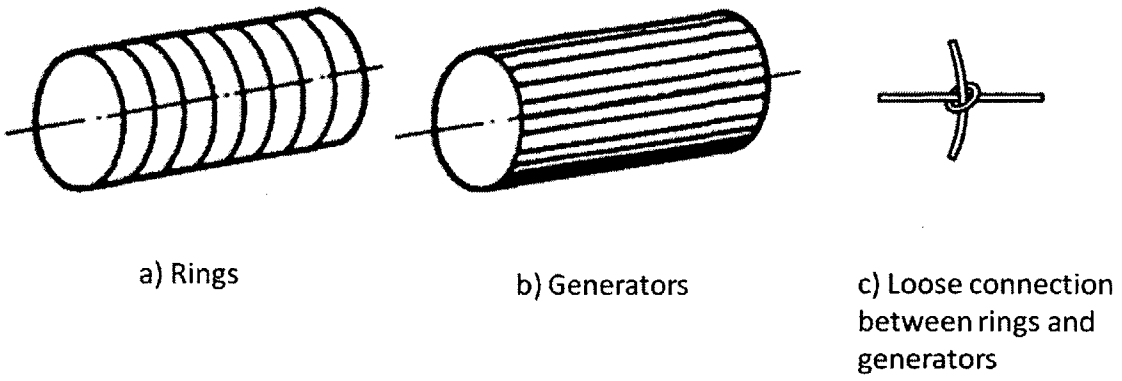

Figure 2-2: Ring-generator model of a cylindrical shell [4].

The rings are assumed to be inextensible in the circumferential direction ($\dot{\varepsilon}_{\theta\theta} = 0$), so energy is dissipated only by bending in the circumferential direction. The generators are treated as beams which can dissipate energy in bending or membrane action. However, the change in longitudinal curvature of the generators is negligible compared to the change in circumferential curvature of the rings ($\dot{\kappa}_{xx} \ll \dot{\kappa}_{\theta\theta}$). Thus, bending of the generators is neglected in this work. The generators dissipate energy only by membrane action (i.e., stretching or compressing axially).

The loose connections between rings and generators require that lateral displacement of the two elements be the same at the connection point. However, the two elements are free to rotate relative to each other. Thus, the connection does not provide any resistance to shear (i.e., $M_{x\theta} = 0$ and $N_{x\theta} = 0$). These simplifying assumptions reduce Eq. (2.7) to:

$$\dot{E}_{int} = 2 \int_0^L R \int_0^{2\pi} \left(N_{xx}\dot{\varepsilon}_{xx} + M_{\theta\theta}\dot{\kappa}_{\theta\theta} \right) d\theta dx \tag{2.8}$$

Because shear energy is neglected, it is reasonable to expect that any analytic solutions will underestimate the total plastic energy dissipation. Suh [4] estimated the effects of shear and made the following conclusions:

1. Shear is less significant in symmetric collapse than in non-symmetric collapse (hydrostatically-induced implosion causes symmetric collapse).

2. The shear effect (as a percentage of total energy dissipation) is greatest for small tube deformation. For deformation on the order of tube radius, the shear increases plastic energy dissipation by no more than 10%.

2.3 Material Model

The cylinder material is idealized as rigid, perfectly plastic with flow stress σ_0. The deflections that occur during implosion are on the order of the cylinder radius (i.e., large deflections). Therefore, the elastic deformations that occur prior to collapse are negligible compared to the plastic deformations that occur during collapse. Thus, the rigid perfectly plastic material idealization is reasonable.

The flow stress, σ_0, lies between the yield stress and ultimate strength, and incorporates strain-hardening effects in an approximate way. The flow stress is calculated by requiring equal areas under the actual material stress-strain curve and the rigid plastic stress-strain curve, up to a given value of plastic strain, ε_1. This is known as the energy equivalent flow stress. All analytic solutions and numerical simulations in this work use aluminum 6061-T6. The specific material characterization was conducted and reported by Beese [27]. The material follows the Swift hardening rule, given by:

$$\sigma = A(\varepsilon_p + \varepsilon_0)^n \tag{2.9}$$

where ε_p is plastic strain, ε_0 is yield strain, and A and n are strain-hardening parameters of the material. The flow stress is calculated as follows:

$$\frac{1}{\varepsilon_1}\int_0^{\varepsilon_1} A(\varepsilon_p + \varepsilon_0)^n d\varepsilon_p = \sigma_0 \tag{2.10}$$

For this specific material (Al6061-T6), A=438 MPa, n=0.07, and ε_0=0.00434 [27]. The resulting flow stress is 351 MPa, assuming the range of expected plastic strain to be $\varepsilon_1 = 0.2$. Figure 2-3 shows the actual Al6061-T6 stress-strain curve, as measured by Beese, along with the 20% energy equivalent flow stress σ_0.

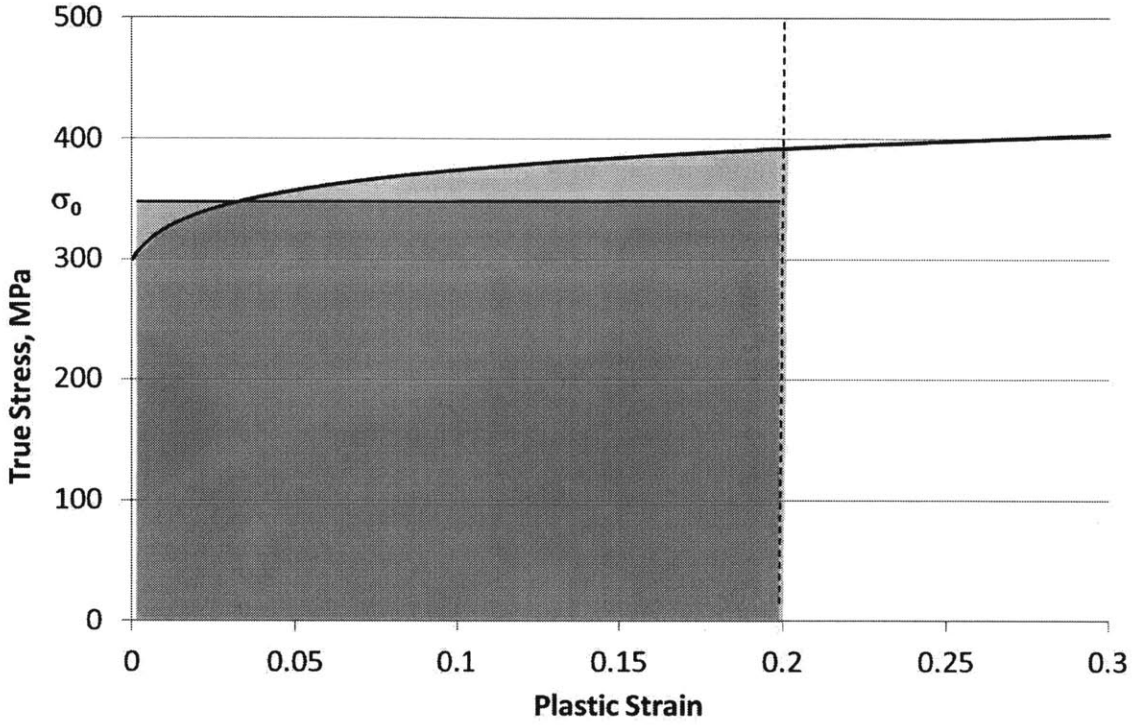

Figure 2-3: 20% Energy equivalent flow stress for Al6061-T6. Areas under actual and rigid plastic stress-strain curves must be equal.

2.4 Yield Condition

The dimensionless membrane force and bending moment tensors are denoted by:

$$n_{\alpha\beta} = \frac{N_{\alpha\beta}}{N_0}\,,\; m_{\alpha\beta} = \frac{M_{\alpha\beta}}{M_0} \tag{2.11}$$

where $N_0 = \sigma_0 h$ is the fully plastic membrane force per unit length and $M_0 = \sigma_0 h^2/4$ is the fully plastic bending moment per unit length. The dimensionless components are related through the yield condition:

$$f\left(m_{\alpha\beta}, n_{\alpha\beta}\right) = 0 \tag{2.12}$$

From the previous simplifications, the general membrane force $N_{\alpha\beta}$ reduces to just N_{xx}, and the general bending moment $M_{\alpha\beta}$ reduces to just $M_{\theta\theta}$. The Huber-Mises yield condition then reduces to:

$$\frac{3}{4} n_{xx}^2 + m_{\theta\theta}^2 = 1 \tag{2.13}$$

Equation (2.13) forms the ellipse shown in Fig. 2-4. Wierzbicki and Hoo Fatt [28] approximated the actual elliptical yield condition with a rectangular limited interaction curve defined by:

$$|N_{xx}| = N_0\,,\; |M_{\theta\theta}| = M_0 \tag{2.14}$$

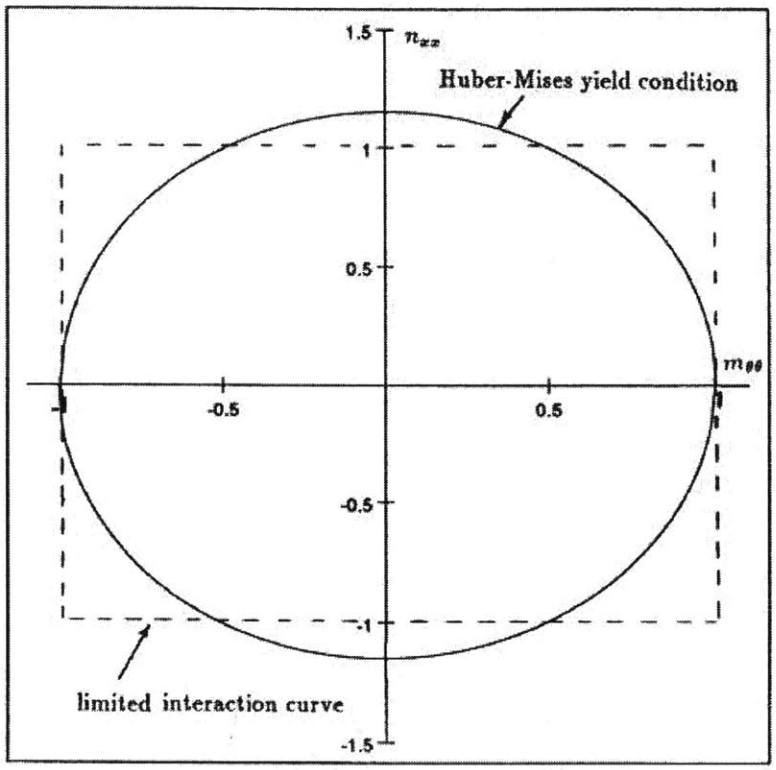

Figure 2-4: Huber-Mises yield condition for a cylindrical shell and a rectangular approximation.

The rate of internal energy dissipation using the limited interaction yield condition is given by:

$$\dot{E}_{int} = 2\int_0^L R\int_0^{2\pi} \left(|N_0\dot{\varepsilon}_{xx}| + |M_0\dot{\kappa}_{\theta\theta}|\right) d\theta dx \tag{2.15}$$

The absolute value signs in Eq. (2.15) are necessary to ensure that the energy dissipation is always non-negative, as required by the associated flow law of plasticity and Drucker's stability postulate.

From Fig. 2-4, it is clear that the approximate yield condition overestimates the stress state for all cases where $|m_{\theta\theta}| > 0.5$. Thus, using the approximate yield condition will overestimate the plastic energy dissipation. However, the exact degree of overestimation cannot be calculated without a full three-dimensional analysis of the problem, which is analytically intractable. The overestimation due to the approximate yield condition is partially offset by the underestimation due to neglect of shear effects. The exact result of these two combined errors is impossible to determine, but is believed to be small.

2.5 Kinematic Assumptions and Models for Cylinder Collapse

Evaluation of Eq. (2.15) requires a kinematic model of sufficient simplicity to make analytic solutions possible. Following the framework established by the ring-generator cylinder model, the kinematic model must address 1) the collapse of individual cross-sectional rings, and 2) the variation of collapse along the longitudinal length of the cylinder.

2.5.1 Phases of Collapse

The symmetric mode 2 collapse of a cylinder under hydrostatic load is divided into three phases. Phase 1 is from initiation of collapse until the moment of first contact between opposite cylinder walls. First contact occurs at a single point on the center cross-section. After first contact, the cylinder begins to flatten in both the radial direction on the center cross-section, and the longitudinal direction. Phase 2 is from the moment of first contact until the moment of maximum flattening of the center cross-section. The degree of flattening of the center cross-section is dependent on the hydrostatic pressure and the diameter-to-thickness ratio (D/h). Following Phase 2, the flattening progresses longitudinally along the cylinder until it reaches a final state. Phase 3 is from the end of Phase 2 until the final state. As in Phase 2, the extent of final flattening is dependent on the hydrostatic pressure and the diameter-to-thickness ratio (D/h). Figure 2-5 depicts the three collapse phases for a representative numerical simulation.

(a) End of Phase 1

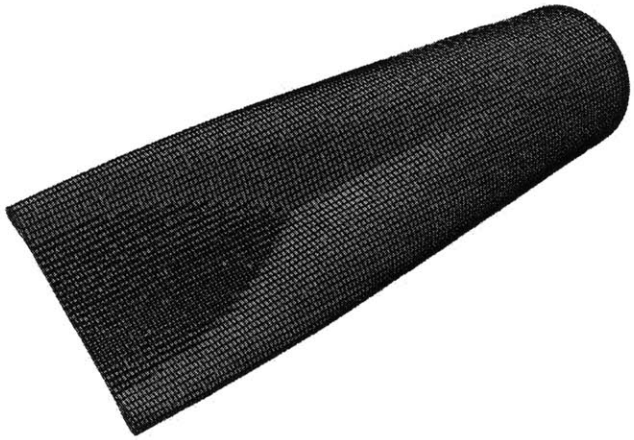

(b) End of Phase 2

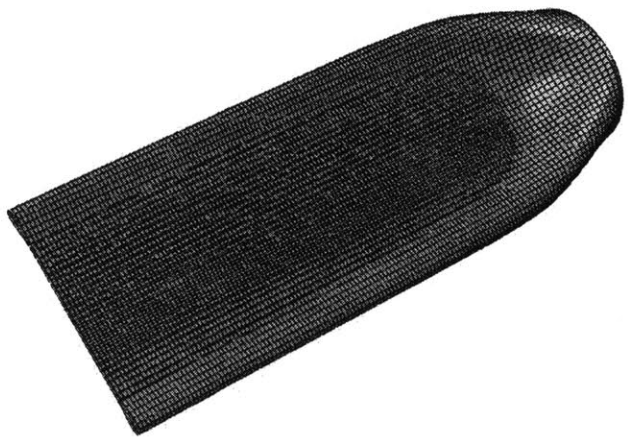

(c) End of Phase 3

Figure 2-5: Phases of mode 2 collapse.

2.5.2 Models for Ring Collapse

Stationary Hinge Model

A number of kinematic models for plastic ring deformation under the action of external pressure have been proposed and used. The simplest model, first used by Palmer and Martin [5], consists of four stationary plastic hinges connecting four rigid segments (Fig. 2-6).

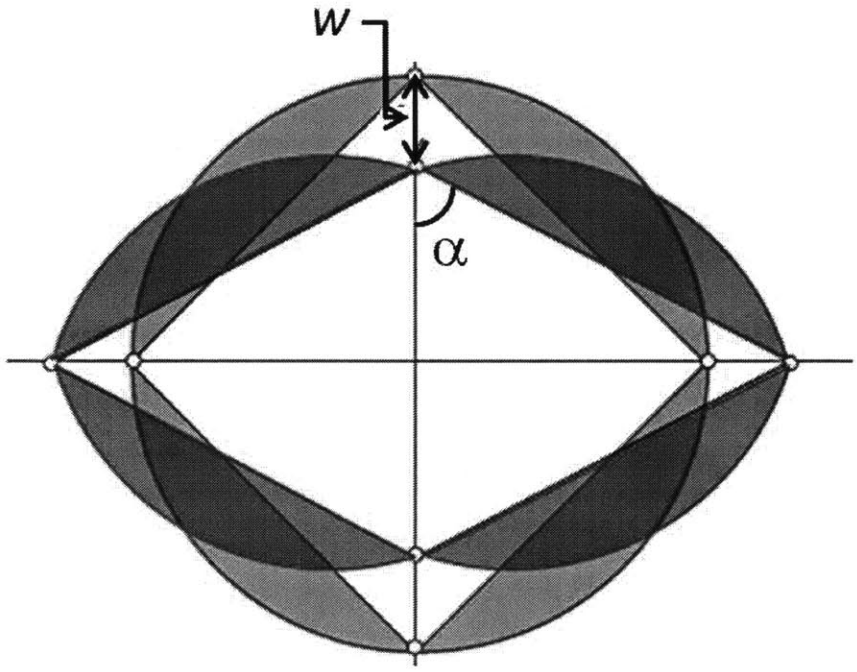

Figure 2-6: Stationary hinge model [5].

This model is called the stationary hinge model throughout this work. The shape of the ring at any time is fully described by a single degree of freedom (DOF): either displacement of the center point, w, or the angle α. During Phase 1 collapse, w varies from 0 to R, and α varies from $\pi/4$ to $\pi/2$. From the geometry of the model, the relationship between w and α is:

$$\frac{w}{R} = 1 - \sqrt{2}\cos\alpha \tag{2.16}$$

This relationship is nearly linear, as seen in Fig. 2-7, and can be approximated as:

$$\frac{w}{R} = 1.287\alpha - 1.0431 \tag{2.17}$$

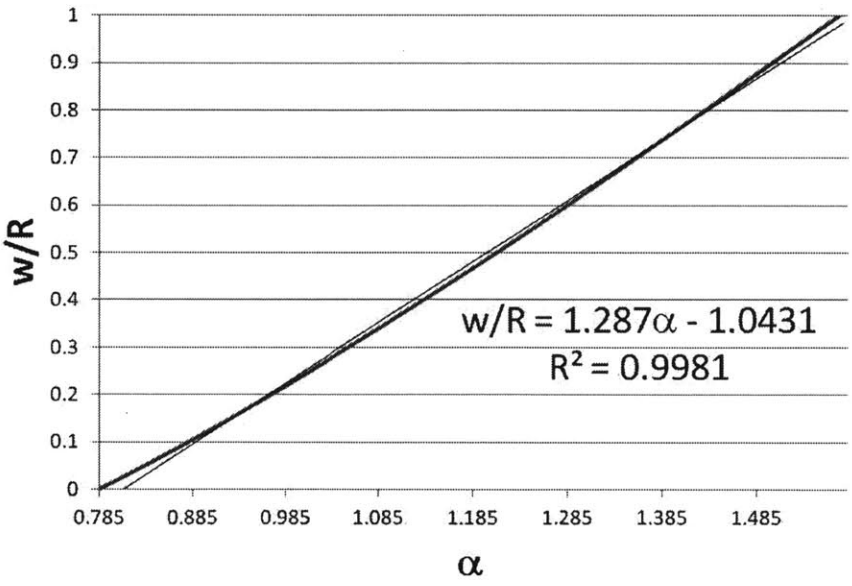

Figure 2-7: Stationary hinge model relationship between w and α, with linear approximation.

The stationary hinge model is only applicable during Phase 1; it does not allow for flattening of the ring during Phases 2 and 3. Therefore, another kinematic model is required to analyze Phases 2 and 3.

Moving Hinge Model

In this thesis, a new 1 DOF traveling hinge kinematic model is proposed which is valid during all phases of collapse. This model is hereafter referred to as the moving hinge model (MHM). In Phase 1, the ring progresses through deformed shapes characterized by the parameter w (deflection from the original position), as shown in Fig. 2-8. Each quarter of the ring is divided into two arcs: one with constant radius R and angle α, and the other with variable radius r and angle $(\frac{\pi}{2}+\alpha)$. As the deformation progresses, α increases and r decreases.

The relationship between α and r follows from the condition of ring inextensibility:

$$R\alpha + \left(\frac{\pi}{2} + \alpha\right) r = \frac{\pi}{2} R$$

or

$$\frac{r}{R} = \frac{\frac{\pi}{2} - \alpha}{\frac{\pi}{2} + \alpha} \tag{2.18}$$

The angle α at the end of phase 1 is designated α_f, and is calculated from simple trigonometry:

$$\cos \alpha_f = \frac{R}{R+r} \tag{2.19}$$

With the substitution of Eq. (2.18), the following equation is obtained for α_f:

$$\cos \alpha_f = \frac{1}{2} + \frac{\alpha_f}{\pi} \tag{2.20}$$

whose approximate solution is

$$\alpha_f \approx \frac{\pi}{4} \; [rad] \tag{2.21}$$

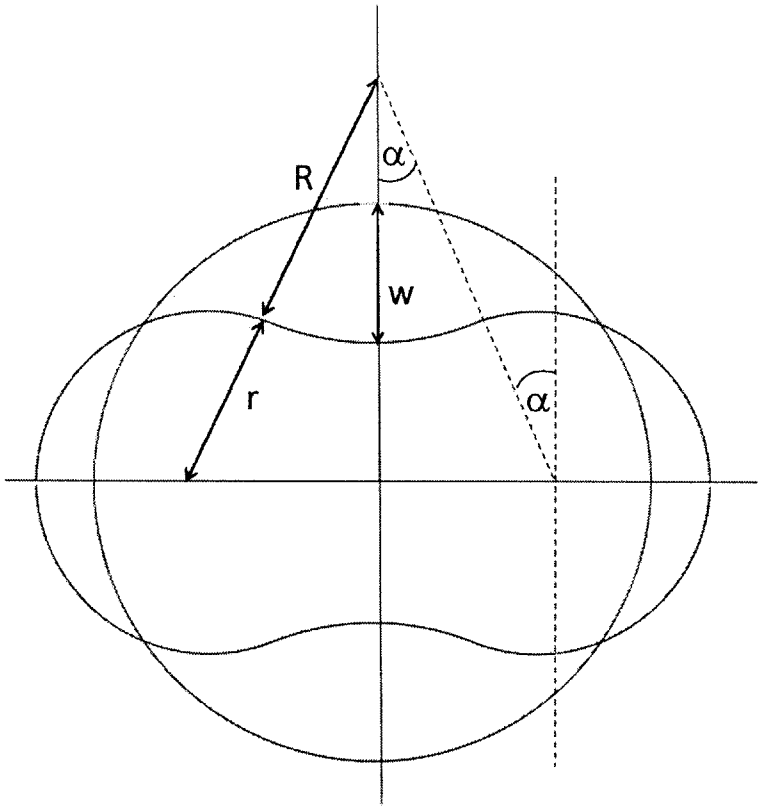

(a) Intermediate state

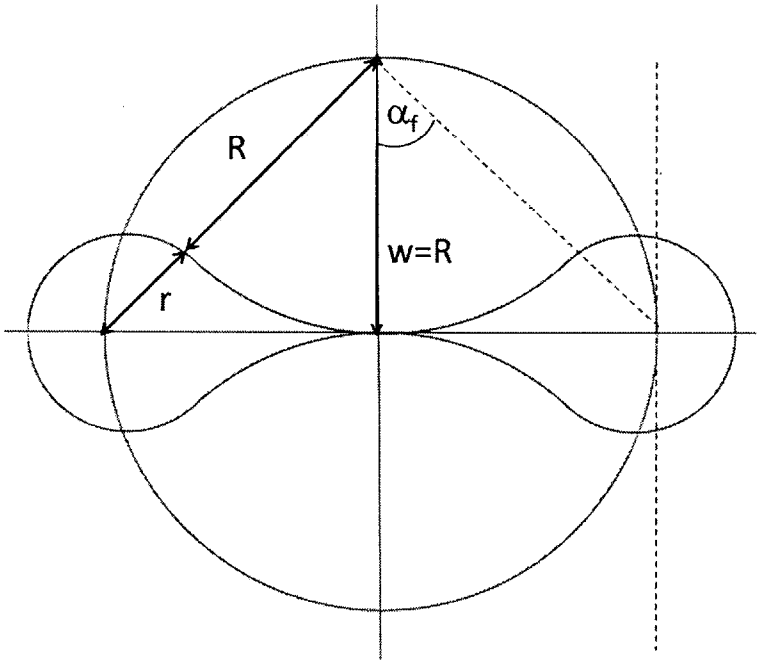

(b) End of Phase 1

Figure 2-8: Moving hinge model deformation during Phase 1

The relation between w and α is derived as follows:

$$\begin{aligned} w &= R - [(r+R)\cos\alpha - R] \\ &= 2R - (r+R)\cos\alpha \end{aligned} \tag{2.22}$$

Rearranging terms and substituting Eq. (2.18) gives:

$$\frac{w}{R} = 2 - \frac{\pi\cos\alpha}{\left(\frac{\pi}{2}+\alpha\right)} \tag{2.23}$$

As with the stationary hinge model, this relationship is nearly linear (Fig. 2-9), and can be approximated as:

$$\frac{w}{R} \approx \frac{\alpha}{\alpha_f} = 1.346\alpha \tag{2.24}$$

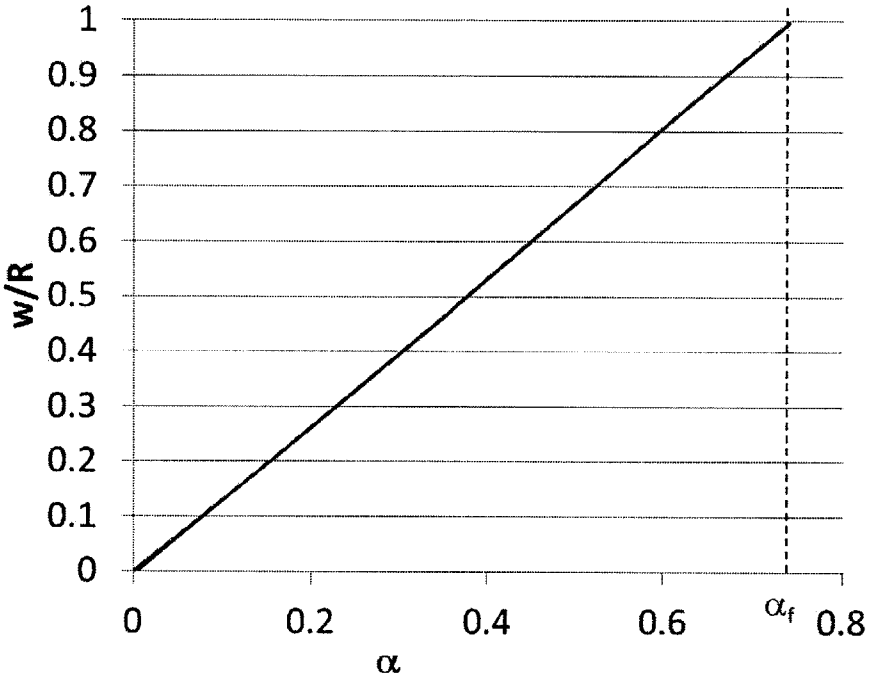

Figure 2-9: Moving hinge model relationship between w and α.

The accuracy of the MHM can be evaluated by comparing the predicted ring shape to a numerical simulation at different stages of collapse. Figure 2-10 shows the comparison for $w = 0.25R$, $w = 0.5R$, $w = 0.75R$, and $w = R$. The comparison indicates that the MHM closely approximates the actual shape of the collapsing ring throughout Phase 1.

In Phase 2, the MHM progresses through deformed shapes characterized by the parameter b (the half-width of the flattened portion of the ring), as shown in Fig. 2-11. Each quarter of the ring is divided into three segments: a straight segment of length b, an arc with variable radius R_1 and constant angle $\alpha_f = \frac{\pi}{4}$, and an arc with variable radius r and constant angle $\frac{\pi}{2} + \alpha_f = \frac{3\pi}{4}$.

In order to restrict the model to 1 DOF, two assumptions are made:

1. The angle α is constant and independent of b, and is equal to α_f, the angle at the end of Phase 1.

2. The ratio r/R_1 remains constant from the end of Phase 1 throughout Phase 2.

At the end of Phase 1, $r = r_f$ and $R_1 = R$. From Eq. (2.18),

$$\frac{r_f}{R} = \frac{\frac{\pi}{2} - \alpha_f}{\frac{\pi}{2} + \alpha_f} = \frac{\frac{\pi}{2} - \frac{\pi}{4}}{\frac{\pi}{2} + \frac{\pi}{4}} = \frac{1}{3} \tag{2.25}$$

The inextensibility condition gives:

$$b + \alpha R_1 + \left(\frac{\pi}{2} + \alpha\right) r = \frac{\pi}{2} R \tag{2.26}$$

Applying the above assumptions to Eq. (2.26) results in the following relation between b and r:

$$r = \frac{R}{3} - \frac{2b}{3\pi} \tag{2.27}$$

Thus, the ring shape at any instant is fully described by a single DOF (b or r).

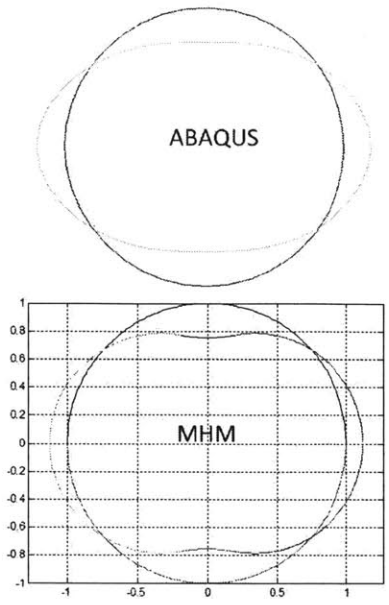

(a) $w = 0.25R$

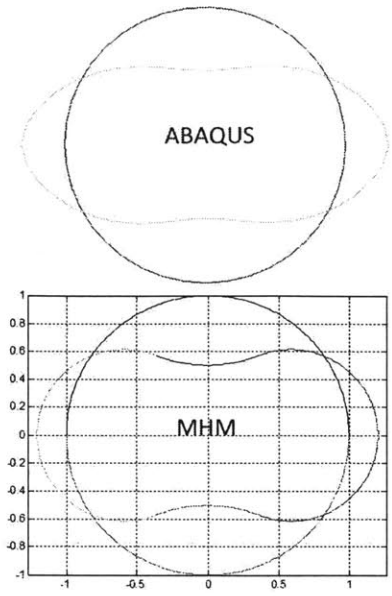

(b) $w = 0.5R$

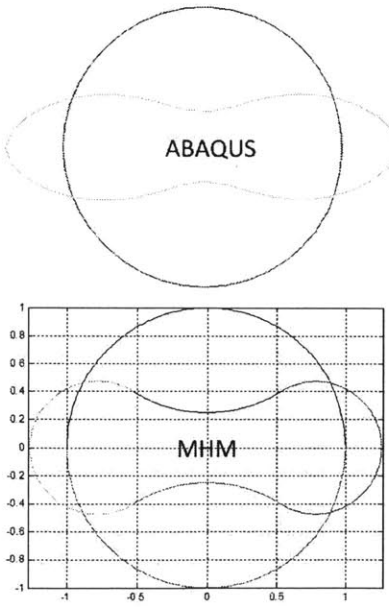

(c) $w = 0.75R$

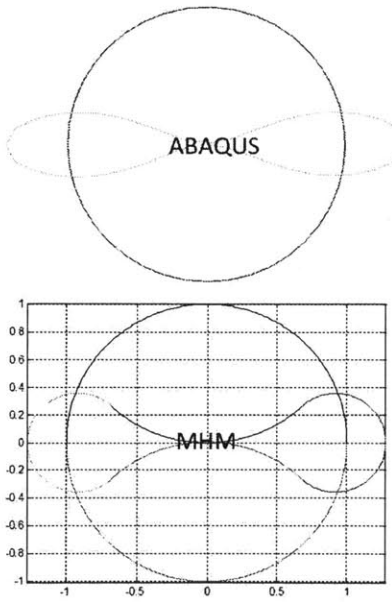

(d) $w = R$

Figure 2-10: Comparison of moving hinge model and numerical simulation during Phase 1

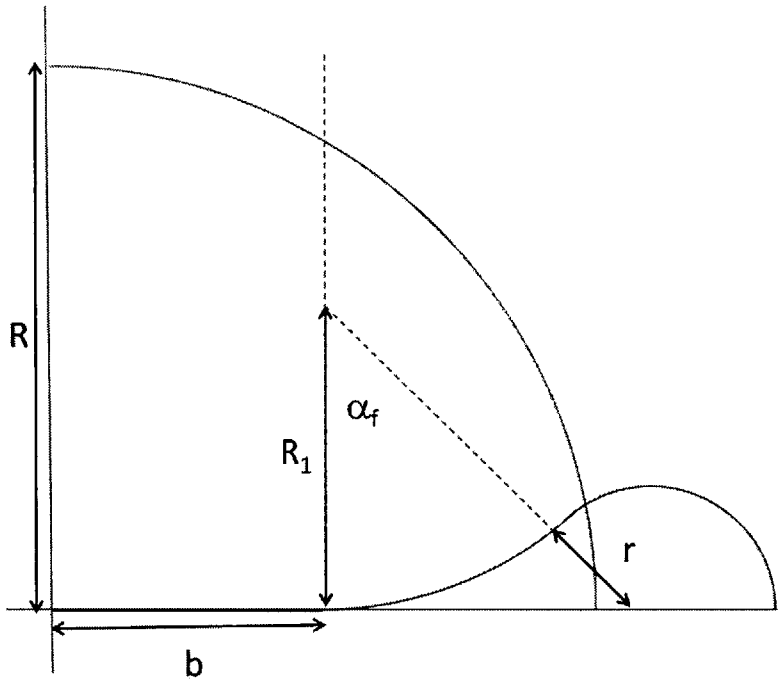

(a) Intermediate position

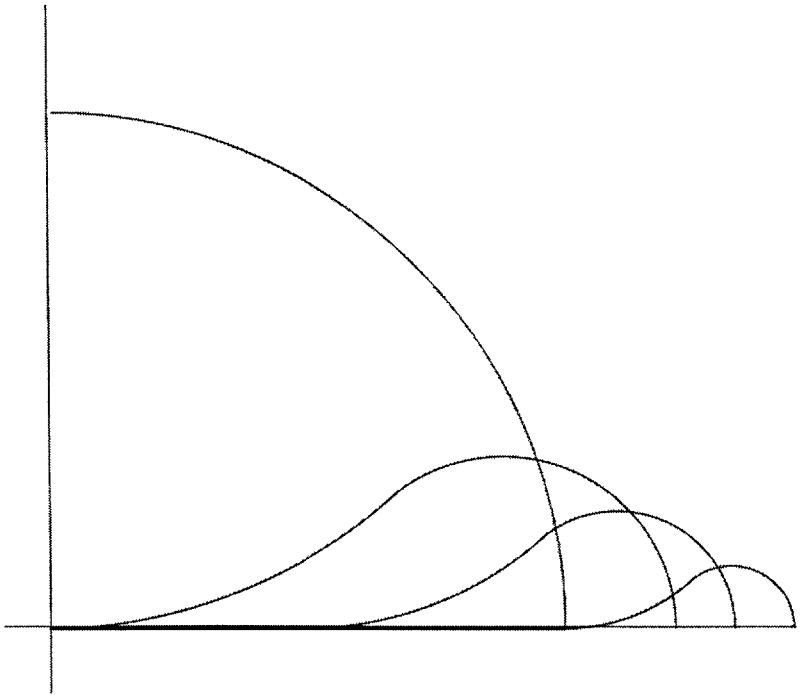

(b) Progressive deformation states

Figure 2-11: Moving hinge model deformation during Phase 2

2.5.3 Longitudinal Assumptions

Bhat and Wierzbicki [29] and Dyau and Kyriakides [30] studied propagating buckles in long pipelines under hydrostatic load. They concluded that in an infinitely long unconstrained pipeline, a localized region of deformation (i.e., buckling) occurs, and the deformation zone then travels in both directions along the length of the pipe. Figure 2-12 illustrates this scenario, where ζ represents the length of the deformed region.

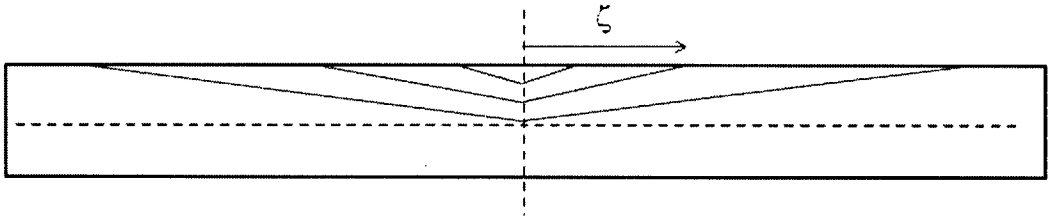

Figure 2-12: Expanding deformation zone in long pipeline under hydrostatic load.

In contrast, the present analysis of finite-length cylinders with rigid endcaps under hydrostatic load indicates that deformation occurs along the entire length of the cylinder, even in the earliest stages. There is no traveling or expanding longitudinal deformation zone. Figure 2-13 shows the longitudinal deformation profile during Phase 1 from a representative numerical simulation, for varying levels of central deflection w_0.

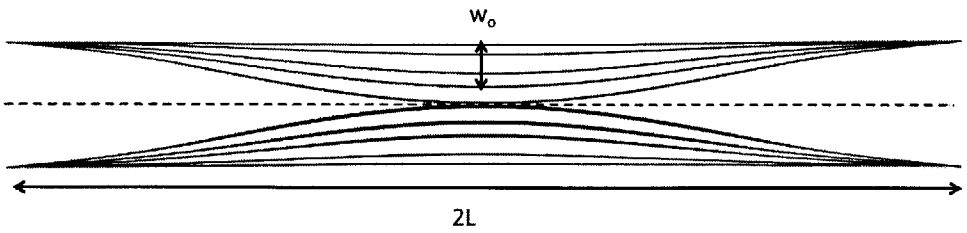

Figure 2-13: Longitudinal deformation profile during Phase 1 (numerical simulation).

In this work, it is assumed that the longitudinal deformation profile is linear or triangular, as shown in Fig. 2-14.

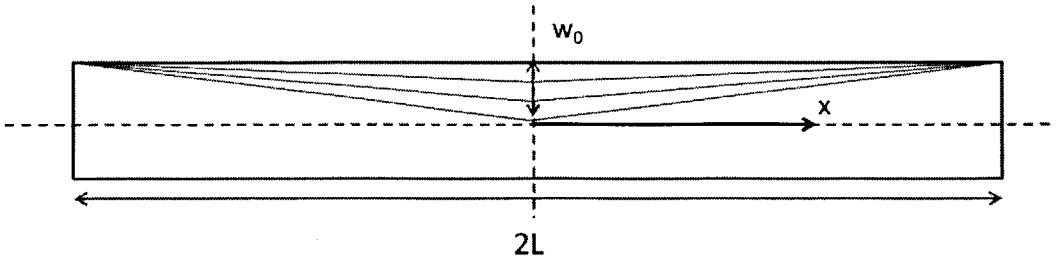

Figure 2-14: Linear longitudinal deformation profile during Phase 1.

This linear profile is expressed mathematically as:

$$w(x) = w_0 \left(1 - \frac{x}{L}\right) \tag{2.28}$$

where w_0 is the deflection of the center. This linear approximation of longitudinal profile is used throughout the remainder of this thesis. The effect of this linear approximation on energy dissipation is evaluated for a specific example cylinder in Appendix A. Compared to a more accurate cubic longitudinal profile, the linear approximation underpredicts the energy calculations by only 3.4%. The benefit of the linear approximation simplicity compared to the cubic profile far outweighs this small error. Thus, it was determined that the linear profile approximation is adequate for this work.

In order to understand the difference in longitudinal behavior between the previous pipeline work and the present work, a study was done using an ABAQUS numerical simulation. First, to investigate the effect of length, a very long (but finite) cylinder with rigid endcaps was considered. The length of the cylinder represented in Fig. 2-13 was increased so that the length-to-diameter ratio ($2L/D$) was 50 (compared to the original $2L/D$=8, typical value for problems considered in this thesis). All other properties of the model were kept the same, including the rigid endcaps. The results showed that, even for the extremely long cylinder, the deformation occurs along the entire length, just as it did for the shorter cylinder. Figure 2-15 shows the

long cylinder in progressive states of deformation. Even in the earliest stages, it is possible to see some deformation along the entire cylinder length.

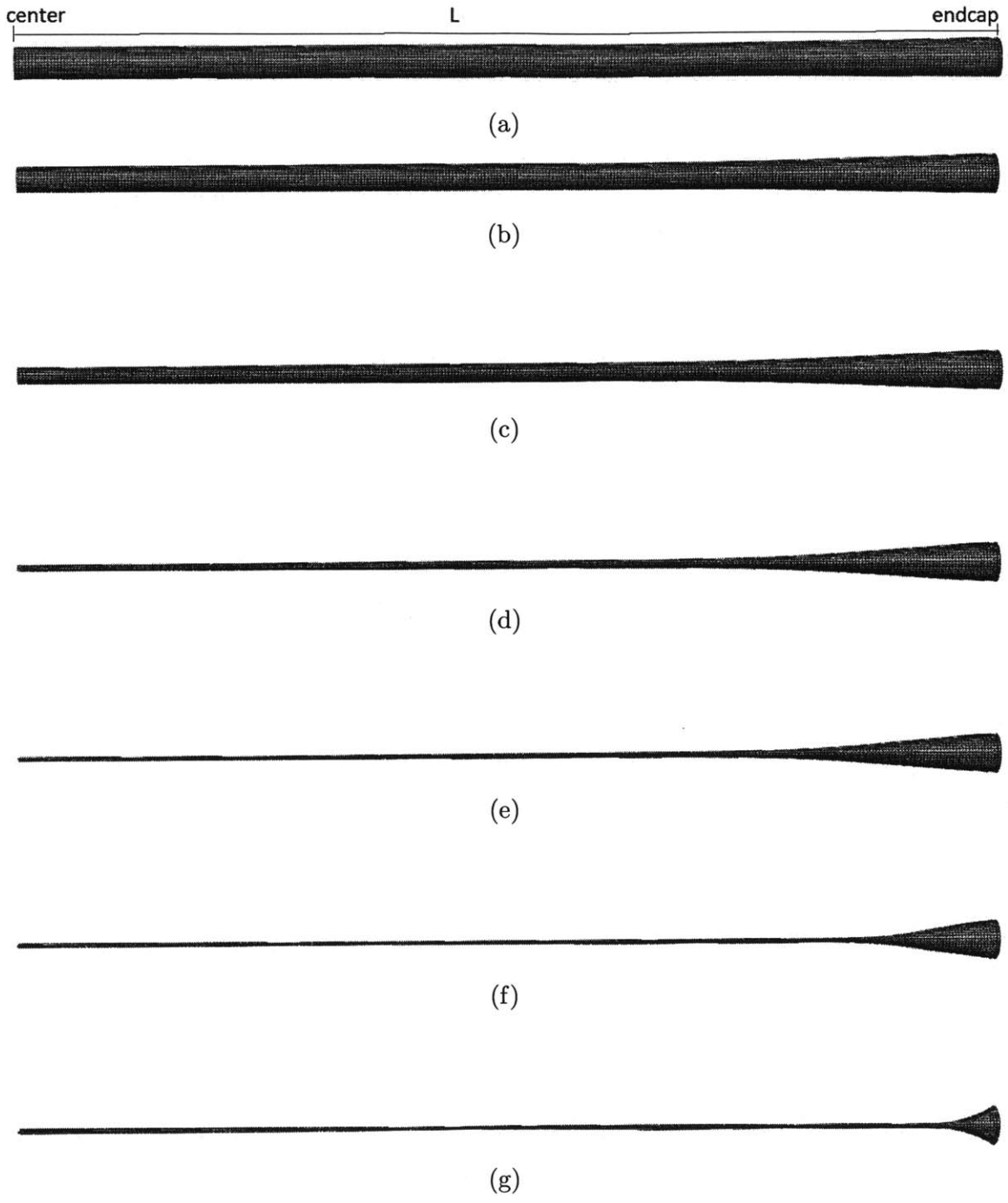

Figure 2-15: Progressive deformation of numerical model with $2L/D = 50$.

Second, to investigate the effect of initial imperfections, a triggering load was introduced into the very long numerical model. The trigger was a large point load initially applied at the longitudinal center, then removed, to simulate an indenter. The results for this simulation are shown in Fig. 2-16. In this case, the deformation starts at the location of the trigger force and spreads longitudinally, just as it does in the infinite pipelines. Figure 2-16 also illustrates the flip-flop mode of buckling behavior in long pipes, described by Kyriakides and Netto [31].

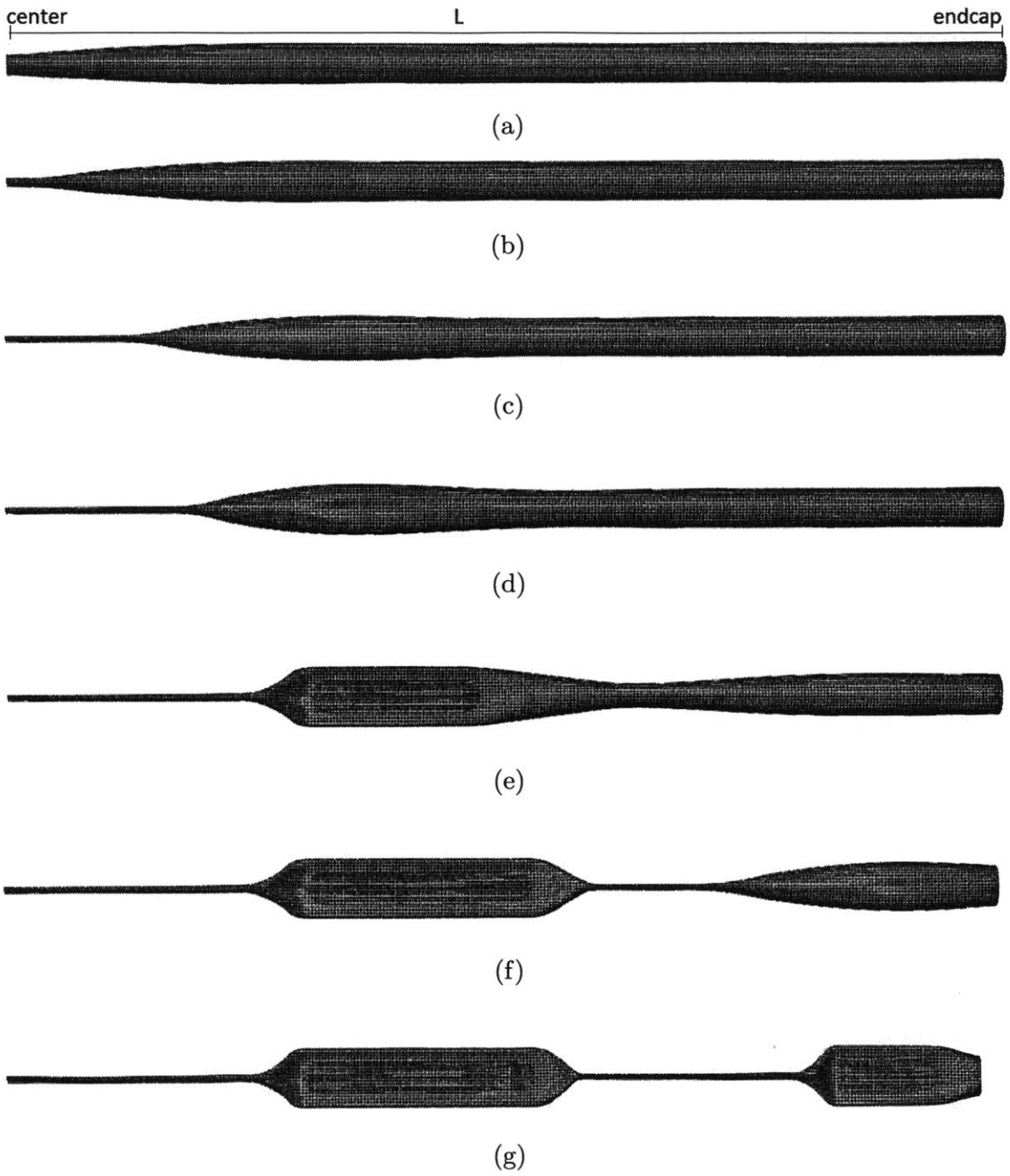

Figure 2-16: Progressive deformation of numerical model with $2L/D = 50$ and indenter load at center.

These results indicate that the difference in longitudinal behavior reported for pipelines and that observed in the present work may be explained primarily by the presence of trigger loads or imperfections. If a trigger load or imperfection is present, the deformation will begin at that location and travel longitudinally, as observed in long pipelines. If no imperfections or trigger loads are present, the deformation will occur along the entire length and will be greatest at the center of the cylinder.

The previous discussion applies to the longitudinal deformation profile during Phase 1. As the collapse continues through Phases 2 and 3, when $w_0 = R$, the flattened center section of the cylinder expands towards the ends. For example, Fig. 2-15d represents the end of Phase 1, and Figs. 2-15e, 2-15f, and 2-15g show the flattened section expanding toward the end during Phases 2 and 3. The longitudinal profile during Phases 2 and 3 is also approximated as linear, as shown in Fig. 2-17.

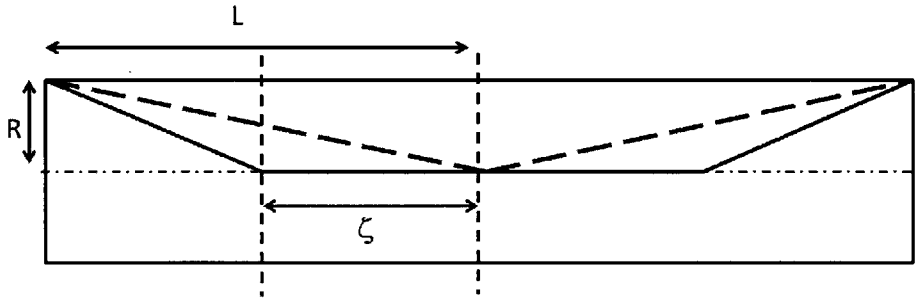

Figure 2-17: Linear longitudinal deformation profile during Phases 2 and 3.

This longitudinal profile is expressed mathematically as:

$$w(x) = \begin{cases} R, & \text{if } x \leq \zeta \\ R\left(1 - \dfrac{x-\zeta}{L-\zeta}\right), & \text{if } \zeta < x \leq L \end{cases} \tag{2.29}$$

where ζ is the length of the center flattened section.

2.6 Effect of Internal Air

The implodable volumes considered in this work contain trapped air. As the cylinder collapses, the air compresses. Compressing the internal air requires energy, and this amount of energy must be added to the right hand side of Eq. (2.3).

In general, the energy required to compress a gas is given by:

$$E = -\int p_i dV \tag{2.30}$$

where p_i is the gas pressure and V is the volume. It is assumed the air in the cylinder is an ideal gas. For polytropic compression of an ideal gas,

$$p_i = p_{i_0}\left(\frac{V_0}{V}\right)^n \tag{2.31}$$

where p_{i_0} and V_0 are initial conditions, and n is the polytropic exponent. If adiabatic compression is assumed, then $n = \gamma$, the ratio of specific heats for the gas ($C_P/C_V = 1.4$ for air). Combining Eqs. (2.30) and (2.31), with $n = \gamma$, gives the following expression for energy required for adiabatic compression:

$$E_{air,adiabatic} = \frac{p_{i_0}V_0}{\gamma - 1}\left[\left(\frac{V_0}{V}\right)^{\gamma-1} - 1\right] \tag{2.32}$$

An alternative assumption is that the compression is isothermal rather than adiabatic. For isothermal compression, $n = 1$. The energy required for isothermal compression is then:

$$E_{air,isothermal} = p_{i_0}V_0 \ln\left(\frac{V_0}{V}\right) \tag{2.33}$$

The actual air compression during implosion is likely somewhere between isothermal and adiabatic (i.e., $1 \leq n \leq 1.4$). Because the implosion event happens so rapidly (on the order of a few milliseconds), it is reasonable to assume that very little heat

will transfer across the cylinder boundary and the process is closer to adiabatic than isothermal. Therefore, adiabatic compression is assumed throughout the remainder of this work.

For the implosion problems considered in this thesis, the volume at the end of collapse varies from about 10% to 30% of the original volume. For $V = 0.1V_0$ and $p_{i_0} =$ 0.1 MPa (atmospheric pressure) undergoing adiabatic compression, the maximum air pressure in the cylinder is given by:

$$p_{i_{max}} = 0.1\text{MPa}\left(\frac{1}{0.1}\right)^{1.4} = 2.5\text{MPa} \tag{2.34}$$

The maximum internal air pressure, $p_{i_{max}}$, can be compared to the external hydrostatic pressure, p, to determine what will happen in the event of fracture of the solid cylinder material. If $p > p_{i_{max}}$, water will flow into the cylinder through any fractures. If $p_{i_{max}} > p$, air will flow out of the cylinder. In all the cases considered in this work, $p > p_{i_{max}}$.

In order to determine the significance of E_{air} in the overall energy balance of an implosion problem, a specific problem was analyzed both with and without internal air. Failure to include internal air in the analysis will result in overestimating the implosion pulse energy by about 8%. Details are provided in Appendix B.

2.7 Dynamic Effects

The quasi-static global equilibrium for an imploding cylinder was given by Eq. (2.3):

$$\dot{E}_{ext} = \dot{E}_{int}$$

However, the actual implosion problem is dynamic in nature. Part of the external work done on the cylinder goes into accelerating the structure. Therefore, the equilibrium equation must include a dynamic term on the right-hand side (equivalent

to the rate of change of kinetic energy). This dynamic term can also be called the D'Alembert inertia term, and can be written as:

$$\dot{E}_{dyn} = \int_S (m\ddot{w})\, \dot{w} dS \tag{2.35}$$

where m is the mass per unit area[2]. The dynamic term is very important, because it represents the maximum amount of energy available to be converted into an implosion pulse. Combining the equation of quasi-static equilibrium, the expression for energy required for air compression, and the expression for D'Alembert inertia gives the following total energy balance equation for the underwater implosion problem:

$$\dot{E}_{ext} = \dot{E}_{int} + \dot{E}_{air} + \dot{E}_{dyn} \tag{2.36}$$

In this work, the D'Alembert inertia term cannot be directly calculated, because in general the velocity and acceleration functions are not known. Rather, the dynamic term is found by calculating all the other terms in Eq. (2.36) and subtracting.

[2]If the structure is surrounded by fluid, as in underwater implosion, then m also includes the added mass of surrounding fluid.

Chapter 3

ABAQUS Numerical Simulation

Numerical simulations of a cylinder subjected to hydrostatic pressure were made using ABAQUS/Explicit, v. 6.10. The purposes of the simulations were twofold:

1. To inform the kinematic assumptions made in the development of the analytic solutions.

2. To validate the accuracy of the analytic solutions for plastic energy dissipation.

3.1 Model Description

The cylinder was modeled using S4R shell elements (4-node, reduced integration, finite membrane strain elements) and consisted of an extruded tube with flat end plates. The thickness was uniform throughout the tube and end plates. Figure 3-1 shows a representative cylinder model.

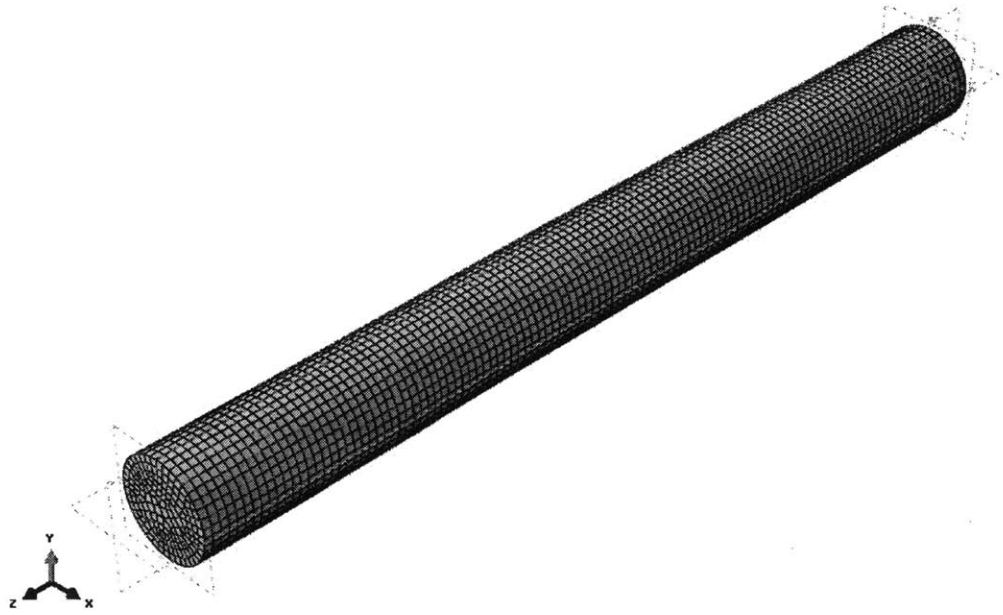

Figure 3-1: ABAQUS model consisting of extruded tube and flat end plates of uniform thickness (shell elements).

A number of different cylinder geometries were modeled, spanning the following ranges:

- 12.7 mm $\leq R \leq$ 19.07 mm
- 274.6 mm $\leq 2L^1 \leq$ 1907 mm
- 0.714 mm $\leq h \leq$ 0.889 mm

This range of dimensions corresponds roughly to the sizes of cylinders tested by the University of Texas at Austin, for which data was available for comparison.

Two different mesh sizes were used: a coarse mesh with elements approximately 3x3 mm, and a fine mesh with elements approximately 1x1 mm. These element sizes resulted in 40-80 elements around the circumference of the cylinder. Most of the simulations were done with the coarse mesh. The fine mesh was used to provide a higher-resolution look at the kinematics of the collapsing cylinder for specific models. The mesh size had no noticeable effect on the energy dissipation calculations.

The material used in all numerical simulations was Al6061-T6. The material model incorporated isotropic strain hardening, using the stress-strain relationship reported by Beese [27]:

$$\sigma = 438\,(\varepsilon_p + 0.00434)^{0.07} \text{ MPa} \tag{3.1}$$

The Young's Modulus of the material was 69.2 GPa, and the yield stress was 263.4 MPa. No fracture modeling was included in the simulations.

Boundary conditions were applied at the circumference of the end plates to prevent translation in the x and y directions and rotation around all three axes. This effectively makes the end plates rigid, with translation in the z direction being the only allowed motion. In a few simulations, translation in the z direction was also prevented, to investigate the effect on energy dissipation.

[1] As defined in Chapter 2, the total cylinder length is 2L.

For each different cylinder model, a static buckling analysis was run first to determine the minimum buckling pressure of the cylinder. Then a dynamic analysis was run with the minimum buckling pressure applied as a uniform hydrostatic load. In some cases, simulations were also run with pressure greater than the minimum buckling pressure, to investigate what effect the magnitude of the pressure had on collapse kinematics and energy dissipation.

The ABAQUS model does not in any way account for the fluid (water) surrounding the cylinder. In effect, it simulates implosion in air. This has the following implications:

1. The simulation does not include the damping effect of the surrounding water. Therefore, the simulated velocities will be greater than the real problem.

2. The simulation does not account for the dynamic fluid pressure acting on the cylinder surface. The simulation applies a constant uniform hydrostatic pressure to the cylinder surface throughout the collapse. In the real problem, the fluid pressure acting on the surface drops in response to the surface motion.

Despite these significant limitations on the simulation, it was adequate for the intended purpose. The intent was not to model the fully-coupled fluid-structure interaction. The purpose of the simulation was simply to analyze the kinematics of an imploding cylinder and the associated plastic energy dissipation. These parameters are largely independent of the surrounding fluid effects.

3.2 Modeling Internal Air

The air trapped inside the cylinder was modeled in ABAQUS using the idealized **surface-based fluid cavity** keyword. The ABAQUS user's manual [32] states that a surface-based fluid cavity can be used to model a liquid-filled or gas-filled structure,

and is defined by a surface that fully encloses the cavity (in this case, the inner surface of the cylinder)[2]. It allows inclusion of fluid effects (specifically pressure on the inside cylinder surface), without the added complexity of actually using fluid elements. A surface-based fluid cavity idealizes the fluid volume by assuming that fluid pressure and temperature are uniform throughout the cavity at any point in time. The fluid cavity was defined in accordance with the following assumptions:

- The fluid (air) is an ideal gas.
- Compression is adiabatic.
- No leakage occurs out of or into the cavity.

The output variables of interest related to the fluid cavity are air pressure and cavity volume, as functions of time. Figure 3-2 shows the air pressure and volume for a typical simulation.

[2]The end plates are included in the model so that a closed surface can be defined around the air cavity. Otherwise, the end plates are unnecessary.

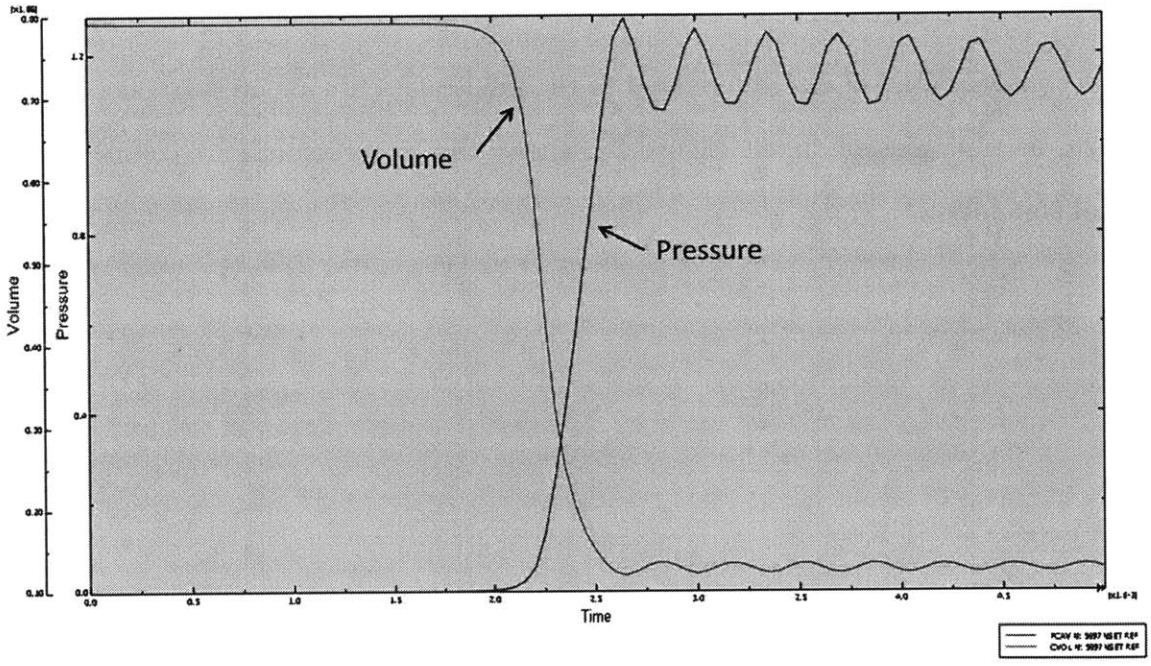

Figure 3-2: Internal air cavity volume and pressure vs. time for a typical implosion.

3.3 Exploration of Explosive-Induced Implosion

The ABAQUS cylinder model was used to conduct a brief study into explosive-induced implosion. As before, the surrounding water was not included in the model, so the simulation was effectively in air. The shockwave created by an airblast explosion is nearly identical to the shockwave generated by an underwater explosion (UNDEX). However, the bubble pulse phenomenon that occurs in UNDEX [19] does not occur in air. Therefore, this analysis only simulates the effect of the initial explosive shock wave.

Explosive airblast loading was applied using the built-in ABAQUS CONWEP model. The CONWEP model calculates a scaled distance based on user-input explosive size (entered as equivalent mass of TNT) and stand-off distance (the distance between the explosive charge and the loading surface). The model then uses the scaled distance and stored empirical airblast data to provide peak pressure, arrival time, positive phase duration, and decay coefficient for the incident and reflected pressure waves [33]. A major advantage of the CONWEP model is that the explosive loading effect is automatically converted into a pressure-time history loading on the cylinder surface; thus, there is no need to model the fluid domain.

Simulations were run with various combinations of hydrostatic pressure and explosive charge size. The goal was to investigate what combinations of hydrostatic and explosive loading would cause complete implosion of the cylinder, and to qualitatively investigate how the implosion mode (or collapse shape) changes for different combinations of hydrostatic and explosive loading. The specific model tested had the following dimensions:

- D=38.14 mm
- $2L$=231.88 mm
- h=0.71 mm

The minimum buckling pressure for this cylinder under purely hydrostatic loading was 1.5 MPa.

The hydrostatic pressure was varied from 0.2 MPa to 1.25 MPa. The explosive charge size varied from 25 g equivalent TNT (yielding a peak pressure of 0.05 MPa) to 700 g equivalent TNT (yielding a peak pressure of 0.7 MPa). In all cases, the standoff distance was 1 m. This standoff was large enough such that the spherical shock wave front created by the explosion was essentially planar across the length of the cylinder. Figure 3-3 shows all loading combinations that were tested, and whether or not implosion occurred for each combination. Furthermore, if implosion occurred, it was classified as symmetric or asymmetric (a subjective classification based on visual observation of the collapsed shape).

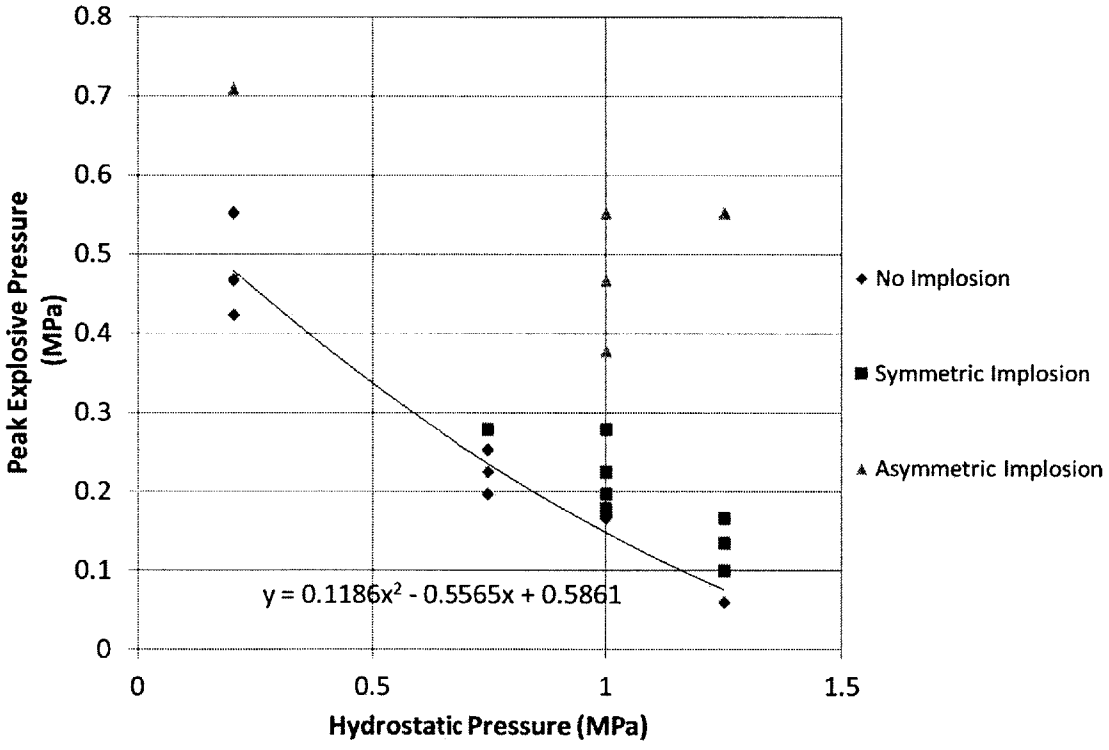

Figure 3-3: Implosion results for varying combinations of explosive and hydrostatic loading.

A best-fit curve through the "No Implosion" points of Fig. 3-3 serves as an implosion threshold. Combinations of explosive and hydrostatic loading below the threshold would not be expected to cause complete implosion. In this particular case, the threshold is approximated by the curve shown on the figure, with the following 2nd-order polynomial equation:

$$p_{exp} = 0.1186 p_{hyd}^2 - 0.5565 p_{hyd} + 0.5861 \tag{3.2}$$

As expected, for a given hydrostatic pressure, the larger the explosive load the more asymmetric the collapse becomes. Figure 3-4 shows the collapse shapes (cut away at the center cross-section) of two different explosive charge sizes, both with hydrostatic pressure of 1.25 MPa. The explosive charge in both cases is located 1 m to the right of the cylinder. Note that even in Fig. 3-4a, there is a slight asymmetry visible on the center cross-section.

(a) Symmetric collapse (charge size=100 g TNT).

(b) Asymmetric collapse (charge size=500 g TNT).

Figure 3-4: Effect of explosive charge size on collapse symmetry (p_{hyd}=1.25 MPa).

Finally, the total plastic energy dissipation and total external work done on the cylinder (E_p and W, as calculated by ABAQUS) were compared for the symmetric and asymmetric collapse cases (Table 3.1).

Table 3.1: Plastic energy dissipation and external work for symmetric vs. asymmetric collapse.

	Symmetric	Asymmetric
E_p	239 J	287 J
W	261 J	310 J
E_p/W	0.916	0.926

The asymmetric case (corresponding to the higher explosive load) collapses more fully, so both E_p and W are higher. However, the ratio E_p/W differs by only 1% for the two cases. This suggests that the plastic energy dissipation, as a percentage of external work, is largely independent of collapse symmetry. The overall energy balance equation for underwater implosion was given by Eq. (2.36), repeated here:

$$\dot{E}_{ext} = \dot{E}_{int} + \dot{E}_{air} + \dot{E}_{dyn}$$

where E_{int}=E_p and E_{ext}=W. This equation and the previous observation suggest that the implosion pulse, which is directly related to $\dot{E}_{dyn}$, is also largely independent of collapse symmetry.

This brief study of explosively-induced implosion is far from conclusive and is not a major emphasis of this thesis. However, it does provide some insight into explosive effects and how explosively-induced implosion differs from hydrostatically-induced implosion.

Chapter 4

Energy Dissipation Calculations

4.1 Kinematic Assumptions and General Energy Dissipation Expressions

The kinematic assumptions used in the energy dissipation calculations are described in detail in Chapter 2 and are summarized here. Two kinematic models of a collapsing ring are considered: the stationary hinge model (SHM) and the moving hinge model (MHM). The SHM is only valid during Phase 1, because it does not allow for flattening of the ring cross-section. The MHM is valid throughout all phases of implosion. A linear deformation profile in the longitudinal direction is assumed, given mathematically by Eqs. (2.28) and (2.29).

$$w(x) = w_0 \left(1 - \frac{x}{L}\right) \text{ (Phase 1)}$$

$$w(x) = \begin{cases} R, & \text{if } x \leq \zeta \\ R\left(1 - \dfrac{x-\zeta}{L-\zeta}\right), & \text{if } \zeta < x \leq L \end{cases} \text{ (Phases 2 \& 3)}$$

The total plastic energy (bending plus membrane) dissipated by the collapsing cylinder is calculated for Phases 1, 2, and 3. In Phase 1, both the SHM and the MHM are used, and the results are compared. In Phases 2 and 3, only the MHM is used. The general equation for rate of plastic energy dissipation is given by Eq. (2.15), repeated here:

$$\dot{E}_{int} = 2\int_0^L R\int_0^{2\pi} (\mid N_0\dot{\varepsilon}_{xx} \mid + \mid M_0\dot{\kappa}_{\theta\theta} \mid) d\theta dx \tag{4.1}$$

The first term on the right-hand side of Eq. (4.1) represents membrane energy, and the second term represents bending energy.

Equation (4.1) gives the instantaneous rate of plastic energy dissipation. In order to calculate total energy dissipated, it is necessary to integrate this rate with respect to time:

$$E = \int_0^t \dot{E} dt \tag{4.2}$$

For each phase of collapse, the time parameter is replaced by a time-like kinematic parameter that describes the state of collapse during that phase (see Table 4.1).

Table 4.1: Time-like parameters for each collapse phase.

Phase	Parameter
1	w_0
2	b_0
3	ζ_3

4.1.1 Bending Energy

The general approach for calculating bending energy for a cylinder is to calculate the energy dissipated per individual ring cross-section, then integrate over the cylinder length to find the total energy dissipated. The instantaneous rate of bending energy

dissipation is:

$$\dot{E}_b = 2\int_0^L R\int_0^{2\pi} \mid M_0\dot{\kappa}_{\theta\theta} \mid d\theta dx + \sum_i \mid M_0\dot{\theta}_i \mid \tag{4.3}$$

where the first term on the right-hand side is due to regions of continuous deformation, and the second term is due to curvature changes at plastic hinges. For moving plastic hinges, $\dot{\theta} = v|\kappa_1 - \kappa_2|$, where v is the speed of the moving hinge and $|\kappa_1 - \kappa_2|$ is the difference in curvature across the hinge [34]. M_0 is the fully plastic bending moment ($M_0 = \sigma_0 h^2/4$), and is assumed to be constant and uniform throughout the material.

4.1.2 Membrane Energy

The general approach for calculating membrane energy is to calculate the energy dissipated per individual longitudinal generator, then integrate over the cylinder circumference to find the total energy dissipated. The instantaneous rate of membrane energy dissipation is:

$$\dot{E}_m = 2\int_0^L R\int_0^{2\pi} \mid N_0\dot{\varepsilon}_{xx} \mid d\theta dx \tag{4.4}$$

where $N_0 = \sigma_0 h$. The longitudinal strain, ε_{xx}, is given by:

$$\varepsilon_{xx} = \frac{du}{dx} + \frac{1}{2}\left(\frac{dw}{dx}\right)^2 \tag{4.5}$$

where u represents displacement in the axial direction and w represents displacement in the transverse direction. The fully plastic axial force, N_0, is assumed to be constant and uniform throughout the material.

With the assumption of a linear deflection profile in the longitudinal direction:

$$\frac{dw}{dx} = \frac{\delta(\theta)}{L} \tag{4.6}$$

where $\delta(\theta)$ is the transverse displacement of a point on the center cross-section. This quantity varies with the circumferential coordinate θ, as shown in Fig. 4-1.

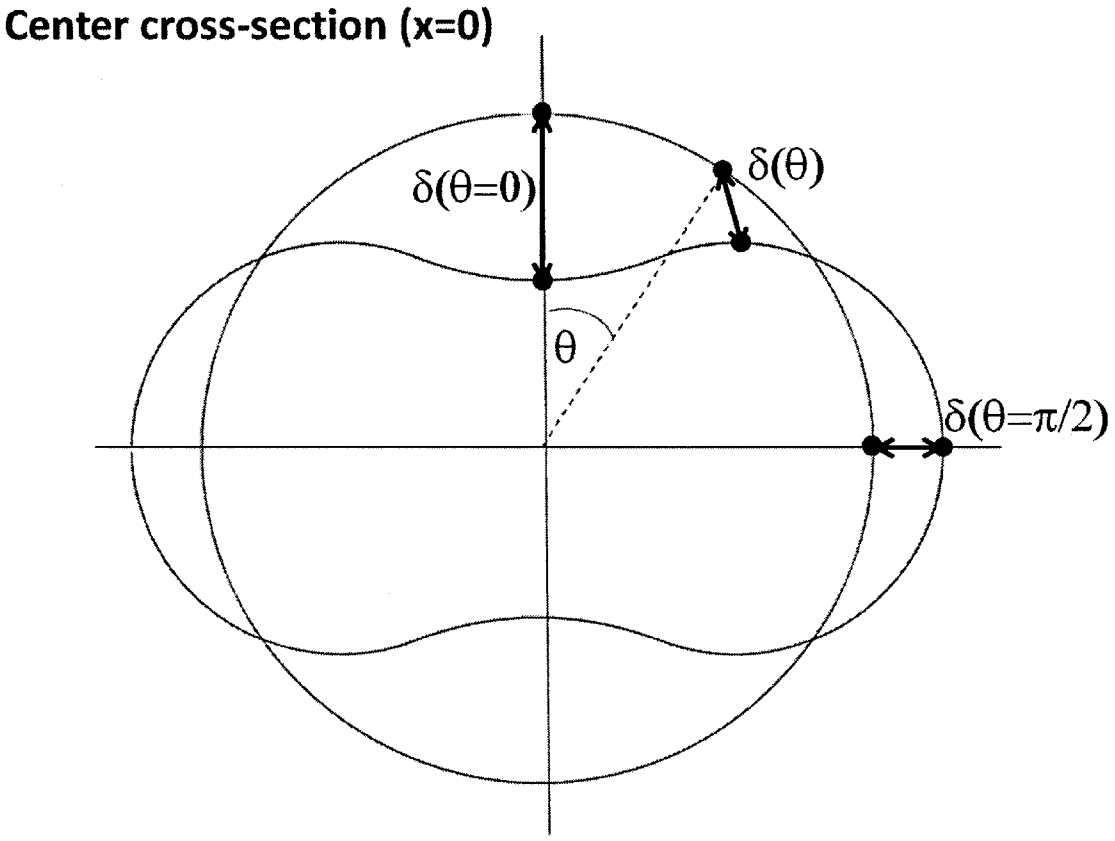

Figure 4-1: Transverse displacement of center cross-section as a function of angle θ.

Substituting Eq. (4.6) into Eq. (4.5) gives:

$$\varepsilon_{xx} = \frac{du}{dx} + \frac{1}{2}\left(\frac{\delta}{L}\right)^2 \tag{4.7}$$

and

$$\dot{\varepsilon}_{xx} = \frac{d\dot{u}}{dx} + \frac{\delta\dot{\delta}}{L^2} \tag{4.8}$$

The instantaneous rate of membrane energy dissipation can then be written as:

$$\dot{E_m} = 2N_0R\int_0^L\int_0^{2\pi} \mid \frac{d\dot{u}}{dx} + \frac{\delta\dot{\delta}}{L^2} \mid d\theta dx \tag{4.9}$$

It is sometimes more intuitive and convenient to work with the ratio $\frac{\delta}{R}$ instead of $\frac{\delta}{L}$. Substituting and integrating over x gives:

$$\dot{E_m} = 2N_0R\int_0^{2\pi} \dot{u}|_{(x=0)}^{(x=L)} d\theta + 2N_0\frac{R^3}{L}\int_0^{2\pi}\left(\frac{\delta\dot{\delta}}{R^2}\right)d\theta \tag{4.10}$$

The first term on the right side of Eq. (4.10) is due to axial movement along the cylinder, and may be positive or negative. The second term is due to the rotation of the generator, and will always be positive.

Free vs. Fixed Boundary Conditions

The boundary conditions on the ends of the imploding cylinder affect the energy dissipation. In most real-world situations, an implodable volume will be unattached to any other structure and supported only by buoyancy, or will be attached to a host structure in such a way that the ends are free to move axially. In this case, the free ends will move towards the center during collapse, and the first term on the right side of Eq. (4.10) will be negative. Thus, the membrane energy dissipated will be less than if the ends were constrained from moving axially. If the ends are physically

constrained, then the axial movement term vanishes[1]. The effect of the end boundary conditions on membrane energy dissipation during Phase 1 is illustrated in Fig. 4-2. The two conditions are identical until about $\frac{w_0}{R} = 0.27$, because there is minimal movement of the free ends to that point. Beyond that point, the free ends begin to move towards the center and reduce the overall membrane energy. For the specific cylinder considered, the free ends reduce the membrane energy dissipation by about 50% at the end of Phase 1.

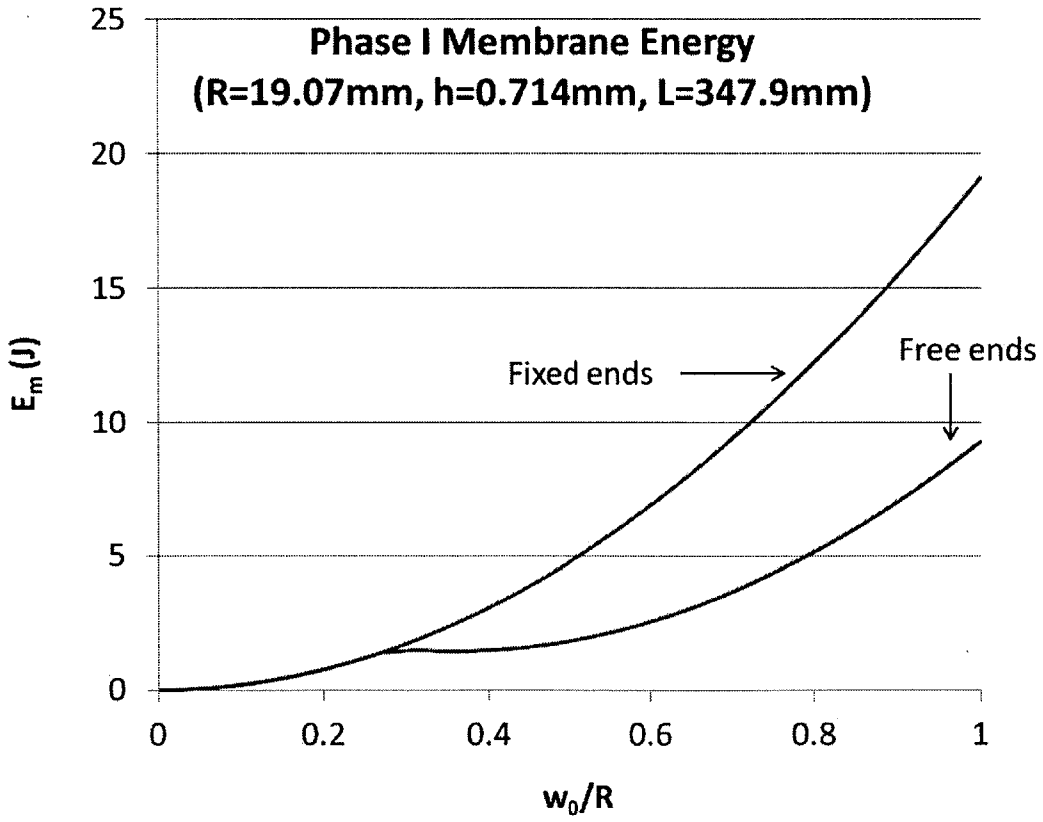

Figure 4-2: Effect of end boundary conditions on Phase 1 E_m.

[1]If the mass (i.e., inertia) of the endcaps is large enough that they do not significantly move during implosion, then the effect is essentially the same as if the ends were physically constrained.

The majority of numerical simulations in this work were done with free end boundary conditions, since this more closely models the real-world situation. In order to investigate the effect that the end conditions have on the magnitude of energy dissipation, a few simulations were run with fixed end conditions (i.e., translation and rotation of the endcaps in all three directions were constrained to zero) and compared to the same cylinder (and same loading) with free end conditions. Figure 4-3 shows the collapsed shape of a cylinder with both types of boundary conditions. It is clear from the figure that there is a qualitative difference in the two collapse shapes. The model with free ends (Fig. 4-3a) shows a broader area of flattening closer to the end, indicating that the bending energy for that case is likely higher. Conversely, the model with fixed ends (Fig. 4-3b) shows more extreme membrane stretching near the end, indicating that the membrane energy for that case is likely higher (as expected).

It is impossible to qualitatively predict which of these two competing effects will dominate. Unfortunately, ABAQUS does not differentiate between bending and membrane energy; it computes total plastic energy dissipated. The total plastic energy dissipated, as a function of time, is plotted in Fig. 4-4 for the free and fixed end simulations. During Phases 1 and 2, the two cases are nearly identical. During Phase 3, the free case is initially higher. Then near the end of collapse, the fixed case increases past the free and finishes at a higher magnitude. This indicates that the extreme membrane stretching of the fixed case at the end of collapse is a larger effect than the increased bending of the free case. The difference in final magnitude for this example is about 30 J, or 4.5% of the total plastic energy dissipated.

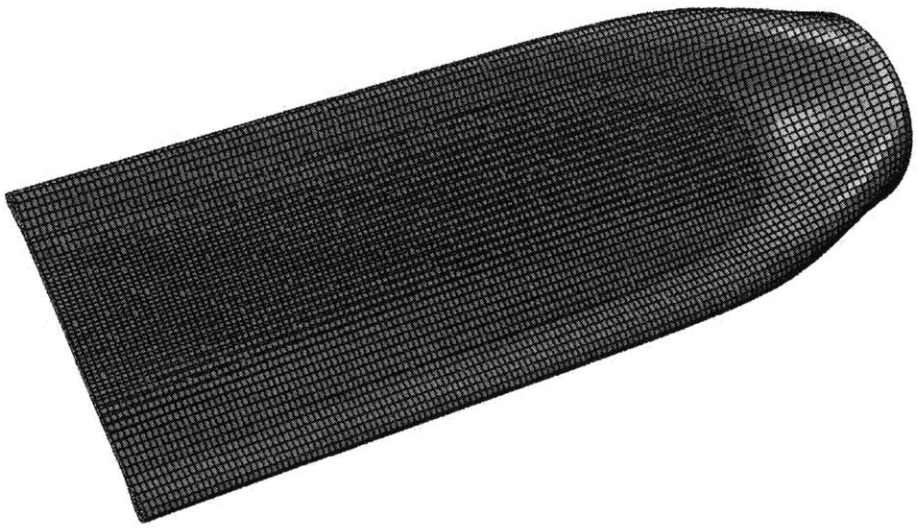

(a) Ends free to translate axially.

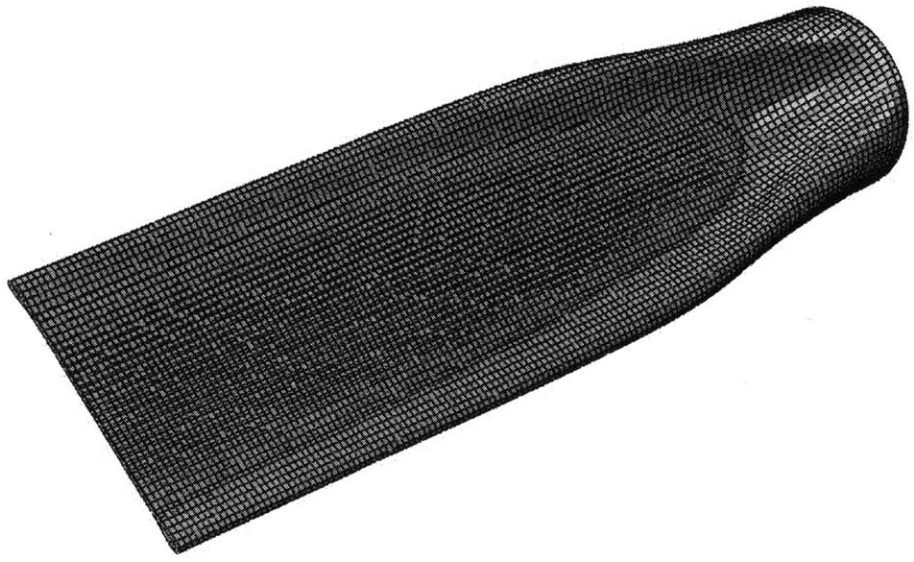

(b) Ends constrained in all 3 directions.

Figure 4-3: Effect of end boundary conditions on collapsed shape.

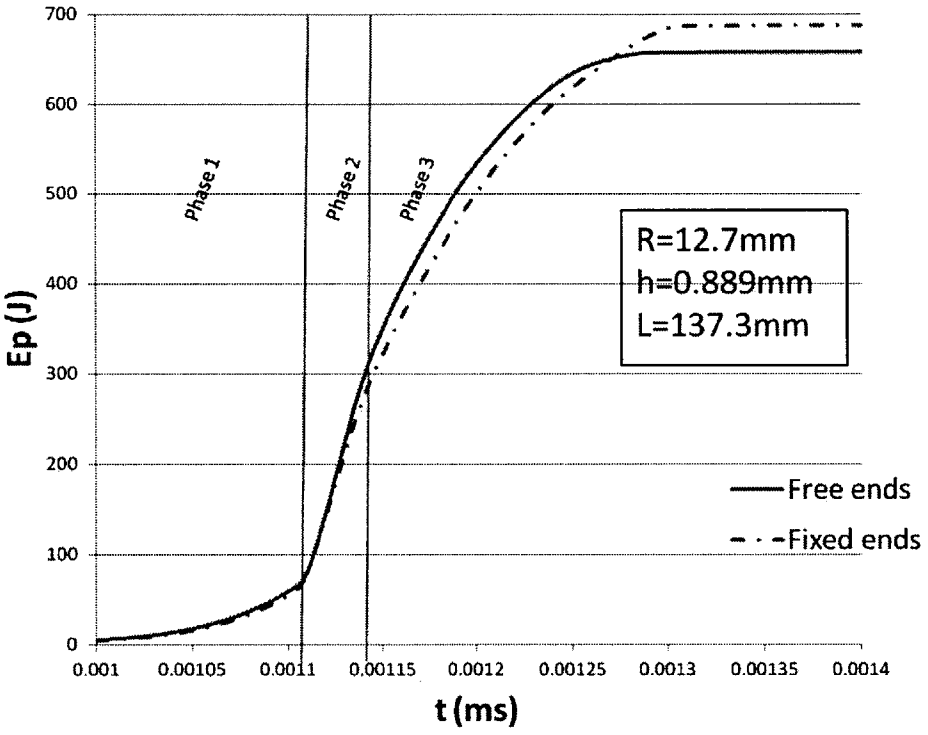

Figure 4-4: Effect of end boundary conditions on total energy dissipation.

In all analytic solutions in this work, the cylinder is assumed to have fixed ends and the first term on the right side of Eq. (4.10) vanishes. This is because the kinematic assumptions upon which the energy dissipation equations are based (described in detail in Section 2.5.3) do not allow for axial displacement.

4.1.3 Path Dependency of Plastic Energy Dissipation

Plastic energy dissipation is in general a path-dependent process (i.e., it depends on the deformation history between states and not just the end states). Plastic energy dissipation is always non-negative, meaning that total energy dissipated can never decrease during a deformation process. Generally speaking, it is easier and more straight-forward to calculate the energy dissipation by considering only the initial and final states of deformation, rather than integrating along the entire deformation path. This is called the *path-independent* approximation. The path-independent approximation will always be a lower bound to the actual value of energy dissipated. It represents the "straight line" deformation from initial to final state, where each element of material is only bent and stretched in one direction. If the actual deformation path involves any repetitive or reverse bending and/or stretching of material elements, then the energy dissipated will necessarily be greater than the path-independent solution. This concept is illustrated in Fig. 4-5. The energy required to bend the bar from state A to state C via the intermediate state B is greater than the energy required to go directly from state A to C.

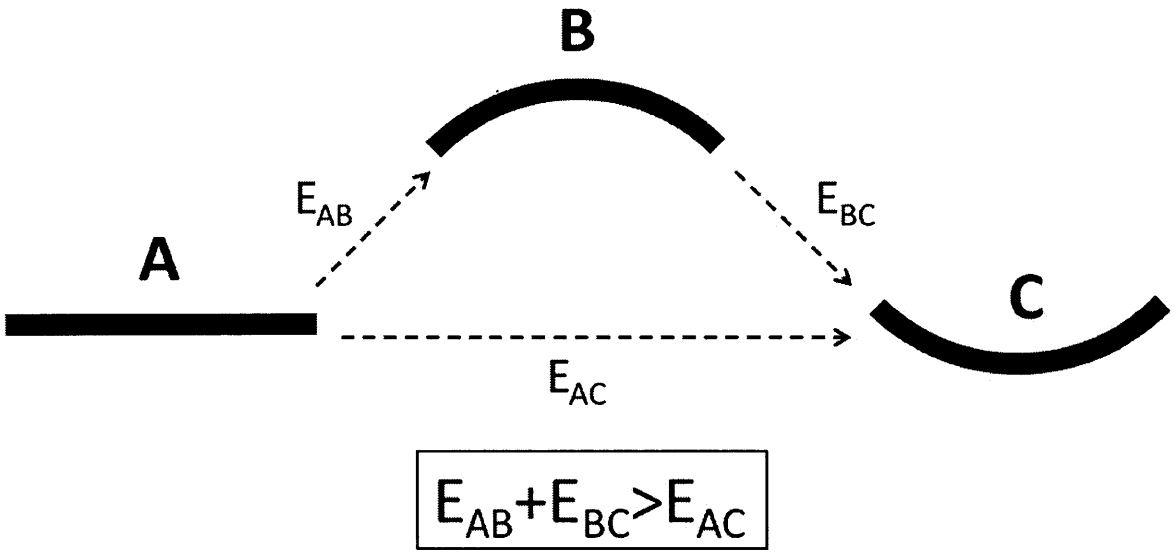

Figure 4-5: Simple illustration of the path-dependence of plastic energy dissipation.

The path-independent bending and membrane energy are calculated as:

$$E_b = \int_S |M_0 \Delta \kappa_{\theta\theta}| dS + \sum_i |M_0 \Delta \theta_i| \tag{4.11}$$

and

$$E_m = \int_S |N_0 \Delta \varepsilon_{xx}| dS \tag{4.12}$$

where $\Delta()$ represents the change from initial state to final state.

For the stationary hinge model, the path-dependent and path-independent solutions are identical. This is because the collapse of the stationary hinge model from the initial undeformed state to the final state (end of Phase 1) follows the "straight line" path. Energy is dissipated only at the plastic hinges (because the ring segments are rigid between the hinges), and the hinges bend in only one direction during collapse.

This chapter includes both path-dependent and path-independent energy calculations. Whenever possible, path-dependent calculations are used, because the real energy dissipation is path-dependent. However, in the case of Phase 2 and 3 membrane energy calculations, the path-independent approximation must be used. Otherwise the solution is computationally impossible. In Phase 1, the calculations are done both ways to demonstrate that the path-independent approximation gives a lower answer.

4.2 Phase 1

Phase 1 energy dissipation is calculated using both the stationary hinge model (SHM) and the moving hinge model (MHM).

4.2.1 Bending Energy

Stationary Hinge Model

The stationary hinge kinematic ring model consists of four plastic hinges connecting four rigid segments, as shown in Fig. 4-6.

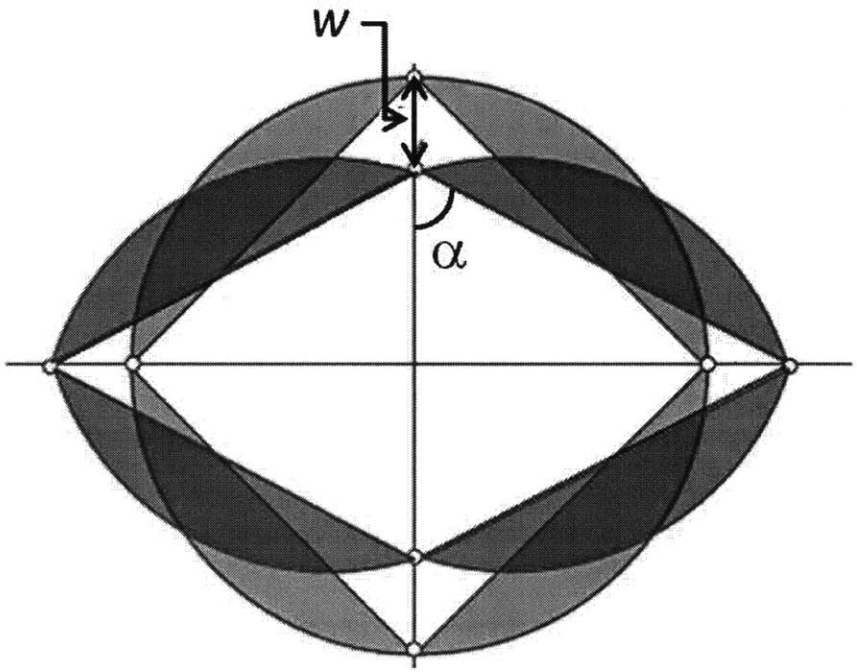

Figure 4-6: Stationary hinge model [5].

For each plastic hinge, $\dot{\theta} = 2\dot{\alpha}$. Since plastic dissipation occurs only at the plastic hinges, equation (4.3) gives the instantaneous rate of bending energy dissipation for a single cross-sectional ring as:

$$\dot{E}_b = 8M_0\dot{\alpha} \tag{4.13}$$

Then the total bending energy for a single ring is calculated as:

$$E_b = \int_0^t \dot{E}_b dt = \int_0^t 8M_0 \frac{d\alpha}{dt} dt = 8M_0 \int_{\frac{\pi}{4}}^{\alpha} d\alpha = 8M_0 \left(\alpha - \frac{\pi}{4}\right) \tag{4.14}$$

The angle α varies along the axial length of the cylinder during Phase 1 deformation, so α (and consequently E_b) are functions of x. The relationship between w and α for the stationary hinge model, first given by Eq. (2.17), is:

$$\frac{w}{R} = 1.287\alpha - 1.0431 \tag{4.15}$$

Combining Eq. (4.15) and the assumed linear longitudinal deformation profile (Eq. (2.28)) gives:

$$\alpha(x) = \frac{w_0}{R} \frac{\left(1 - \frac{x}{L}\right)}{1.287} + \frac{1.0431}{1.287} \tag{4.16}$$

The total bending energy for the entire cylinder is found by integrating $E_b(x)$ over the cylinder length:

$$E_{b,tot} = 2\int_0^L 8M_0 \left(\alpha(x) - \frac{\pi}{4}\right) dx \tag{4.17}$$

Substituting the expression for $\alpha(x)$ gives the following result:

$$E_{b,tot} = 6.22M_0 L \frac{w_0}{R} \tag{4.18}$$

At the end of Phase 1, $w_0 = R$ and $E_{b,tot} = 6.22M_0L$. As explained earlier, the path-dependent and path-independent solutions are identical for the stationary hinge

model.

Moving Hinge Model

For the moving hinge model during Phase 1, the ring is divided into 4 symmetric quarters. Each quarter consists of two segments separated by a moving plastic hinge: one with radius R, and one with radius r (see Fig.4-7).

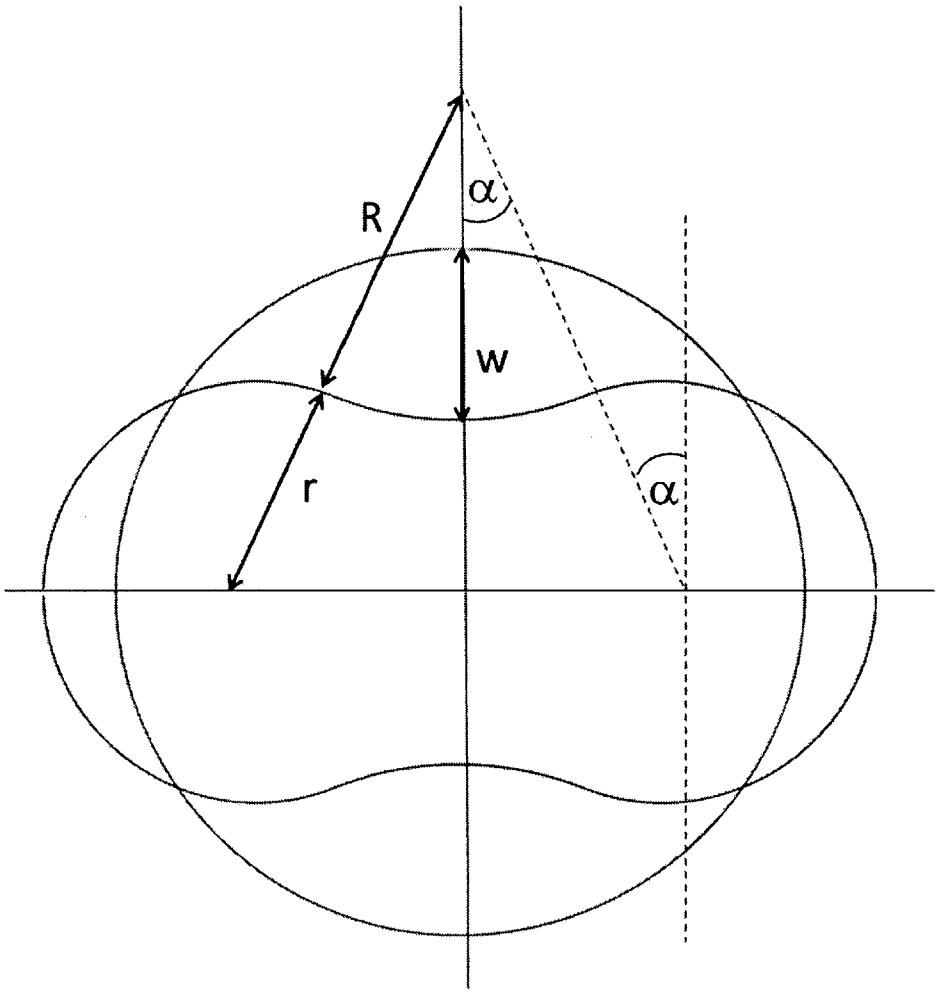

Figure 4-7: Moving hinge model during Phase 1.

The curvature and rate of change of curvature for each segment are:

$$\kappa = \begin{cases} -\frac{1}{R} \ (0 \leq \phi \leq \alpha) \\ \frac{1}{r} \ (\alpha \leq \phi \leq \frac{\pi}{2}) \end{cases} \tag{4.19}$$

and

$$\dot{\kappa} = \begin{cases} 0 \ (0 \leq \phi \leq \alpha) \\ -\frac{\dot{r}}{r^2} \ (\alpha \leq \phi \leq \frac{\pi}{2}) \end{cases} \tag{4.20}$$

Using the geometric relation between R and r (Eq. (2.18)) and substituting into Eq. (4.3) gives the rate of bending energy dissipation for a single cross-section as:

$$\dot{E}_b = M_0 \int_{\alpha}^{\frac{\pi}{2}} -\frac{\dot{r}}{r^2} R d\phi + M_0 \dot{\alpha} \left(\frac{\frac{\pi}{2} + \alpha}{\frac{\pi}{2} - \alpha} + 1 \right)$$

which simplifies to:

$$\dot{E}_b = \frac{2\pi M_0 \dot{\alpha}}{\frac{\pi}{2} - \alpha} \tag{4.21}$$

Integrating with respect to time gives:

$$E_b(x) = 8\pi M_0 \ln \left(\frac{\frac{\pi}{2}}{\frac{\pi}{2} - \alpha(x)} \right) \tag{4.22}$$

The relationship between w and α for the MHM, first given by Eq. (2.24), is:

$$\frac{w}{R} = 1.346\alpha \tag{4.23}$$

Combining Eq. (4.23) and the assumed linear longitudinal deformation profile (Eq. (2.28)) gives:

$$\alpha(x) = \frac{w_0}{1.346R} \left(1 - \frac{x}{L} \right) \tag{4.24}$$

Substituting Eq. (4.24) into Eq. (4.22) and integrating over the cylinder length gives

the following result for the Phase 1 path-dependent bending energy using the MHM:

$$E_{b,tot} = 16\pi M_0 L \left\{ \ln\frac{\pi}{2} - \frac{4R}{w_0}\left[\frac{1}{2}\ln\frac{\pi}{2} - \left(\frac{1}{2} - \frac{w_0}{4R}\right)\ln\left(\frac{\pi}{2} - \frac{\pi w_0}{4R}\right) - \frac{w_0}{4R}\right]\right\} \quad (4.25)$$

The path-independent solution using the MHM is much simpler. From Eq. 4.11, the bending energy for each cross-section is:

$$E_b(x) = 16 M_0 \alpha(x) \quad (4.26)$$

Substituting the expression for $\alpha(x)$ (Eq. (4.24)) and integrating over the cylinder length gives the following result for the Phase 1 path-independent bending energy using the MHM:

$$E_{b,tot} = 4\pi M_0 L \frac{w_0}{R} \quad (4.27)$$

Evaluation of equations (4.25) and (4.27) at the end of Phase 1 (i.e., when $w_0 = R$) gives $E_{b,tot}$(path-dependent) $= 4.91\pi M_0 L$ and $E_{b,tot}$ (path-independent) $= 4\pi M_0 L$. The path-dependent value is $\approx 25\%$ larger, as expected.

In summary: the Phase 1 bending energy was calculated three ways, and the results are given in Table 4.2.

Table 4.2: End of Phase 1 bending energy.

Model	$\mathbf{E}_b$
SHM	$6.22 M_0 L$
MHM (path-independent)	$12.57 M_0 L$
MHM (path-dependent)	$15.43 M_0 L$

4.2.2 Membrane Energy

Stationary Hinge Model

Calculating the membrane energy dissipated (Eq. (4.9) or (4.10)) requires an expression for δ, the transverse displacement of a point on the center cross-section. For the SHM, Fig. 4-8 shows the geometry of the collapsing ring.

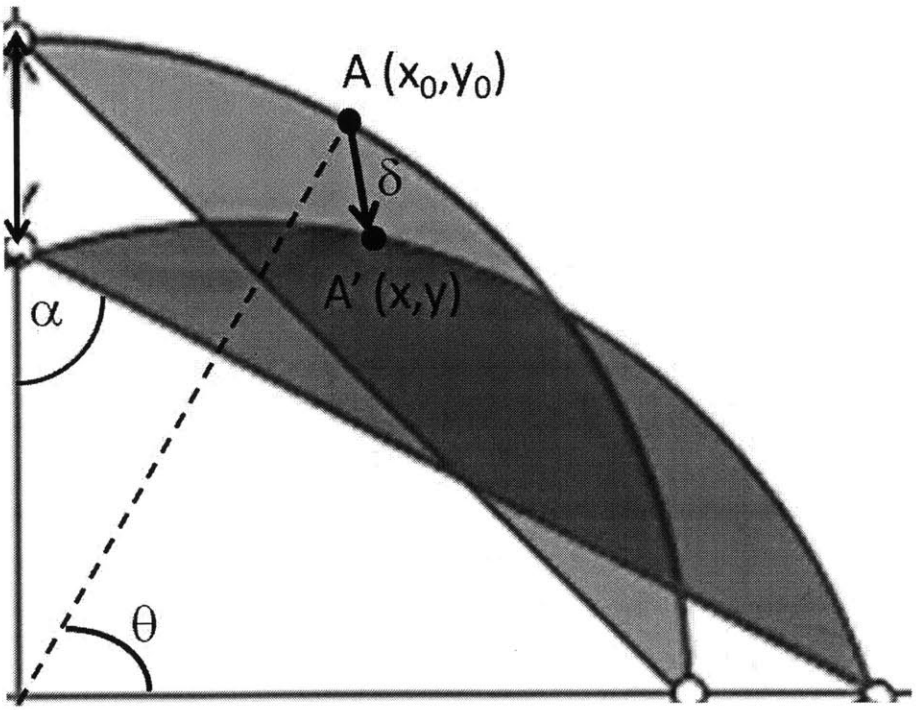

Figure 4-8: SHM geometry for calculating δ.

Point $A(x_0,y_0)$ moves to point $A'(x,y)$. The angle α is the time-like parameter that determines the extent of collapse, and the angle θ determines the position of the point on the ring. The displacement δ is given by:

$$\delta = \sqrt{(x - x_0)^2 + (y - y_0)^2} \tag{4.28}$$

After some trigonometric manipulations, the following relationship is obtained:

$$\begin{aligned}\left(\frac{\delta}{R}\right)^2 =& 3 - 2\sin\theta - \sqrt{2}\,(\sin\alpha + \cos\alpha) - 2\sin\alpha\cos\alpha - 2\sqrt{2}\cos\alpha\sin\theta + \ldots \\ &\ldots + 2\sqrt{2}\cos\alpha\sin\left(\alpha - \frac{\pi}{4} + \theta\right) - 2\sin\left(\alpha - \frac{\pi}{4} - \theta\right)\end{aligned} \tag{4.29}$$

Evaluation of this expression for δ and its time derivative $\dot{\delta}$, as a function of α, is extremely cumbersome. Alternatively, it is assumed that δ will vary linearly with w_0, for any value of θ. At the end of Phase 1 (when $\alpha = \frac{\pi}{2}$):

$$\left(\frac{\delta}{R}\right)^2 = 3 - 2\sin\theta + \sqrt{2}\,(\sin\theta - \cos\theta - 1) \tag{4.30}$$

Assuming that δ changes linearly as w_0 progresses from $0 \rightarrow R$, then:

$$\frac{\delta}{R} = \sqrt{3 - 2\sin\theta + \sqrt{2}\,(\sin\theta - \cos\theta - 1)}\frac{w_0}{R} \tag{4.31}$$

The accuracy of this assumption is plotted in Fig. 4-9 for three different values of θ. It is clear that the linear assumption is more accurate for larger values of θ. Over the range $0 \leq \theta \leq \frac{\pi}{4}$, the linear approximation under-predicts the exact value of $\frac{\delta}{R}$. Over the range $\frac{\pi}{4} > \theta \leq \frac{\pi}{2}$, the linear approximation over-predicts the exact value of $\frac{\delta}{R}$. Therefore, it is reasonable to assume that, when integrated over the whole range of $0 \leq \theta \leq \frac{\pi}{2}$, the linear approximation will be reasonably close to the exact value.

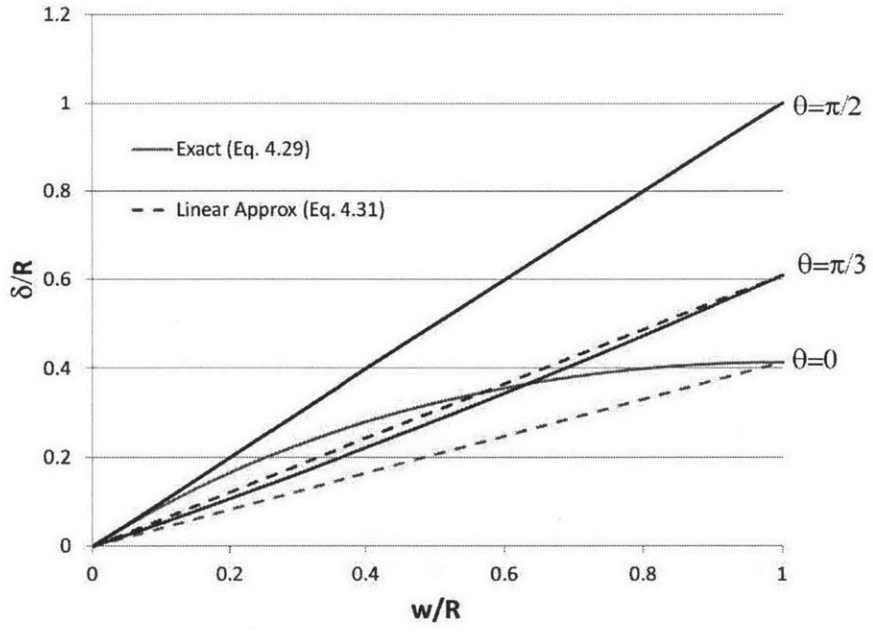

Figure 4-9: Comparison of exact δ/R with linear approximation, for different values of θ.

Given Eq. (4.31), the following expressions are true:

$$\delta = \sqrt{3 - 2\sin\theta + \sqrt{2}\,(\sin\theta - \cos\theta - 1)}w_0 \tag{4.32}$$

and

$$\dot{\delta} = \sqrt{3 - 2\sin\theta + \sqrt{2}\,(\sin\theta - \cos\theta - 1)}\dot{w}_0 \tag{4.33}$$

Substituting Eqs. (4.32) and (4.33) into Eq. (4.9) and integrating over the length gives:

$$\begin{aligned}\dot{E_m} &= 4\pi N_0 R\dot{u}\mid_{x=L} + 8N_0 R\int_0^{\frac{\pi}{2}} \frac{\delta\dot{\delta}}{L}d\theta \\ &= 4\pi N_0 R\dot{u}\mid_{x=L} + 8\frac{N_0 R}{L}\int_0^{\frac{\pi}{2}} \left(3 - 2\sin\theta + \sqrt{2}\,(\sin\theta - \cos\theta - 1)\right) w_0\dot{w}_0 d\theta\end{aligned} \tag{4.34}$$

Fixed end conditions are assumed, so the first term on the right-hand side vanishes. Evaluation of the integral gives the following result:

$$\begin{aligned}\dot{E_m} &= 8\frac{N_0 R}{L}w_0\dot{w}_0\left[\frac{\pi}{2}\left(3 - \sqrt{2}\right) - 2\right] \\ &= 3.928\frac{N_0 R}{L}w_0\dot{w}_0\end{aligned} \tag{4.35}$$

Integrating with respect to time gives the following result for total membrane energy dissipated:

$$E_{m,tot} = 1.964\frac{N_0 R}{L}w_0^2 = 1.964\frac{N_0 R^3}{L}\left(\frac{w_0}{R}\right)^2 \tag{4.36}$$

Moving Hinge Model

The deformed shape of the MHM at the end of Phase 1 is shown in Fig. 4-10, along with two representative points, A and B. Point A moves to A' and B moves to B'. The ring is divided into four symmetric quarters, and each quarter is divided into two

segments: $0 \leq \theta \leq \alpha_f$ and $\alpha_f \leq \theta \leq \frac{\pi}{2}$.

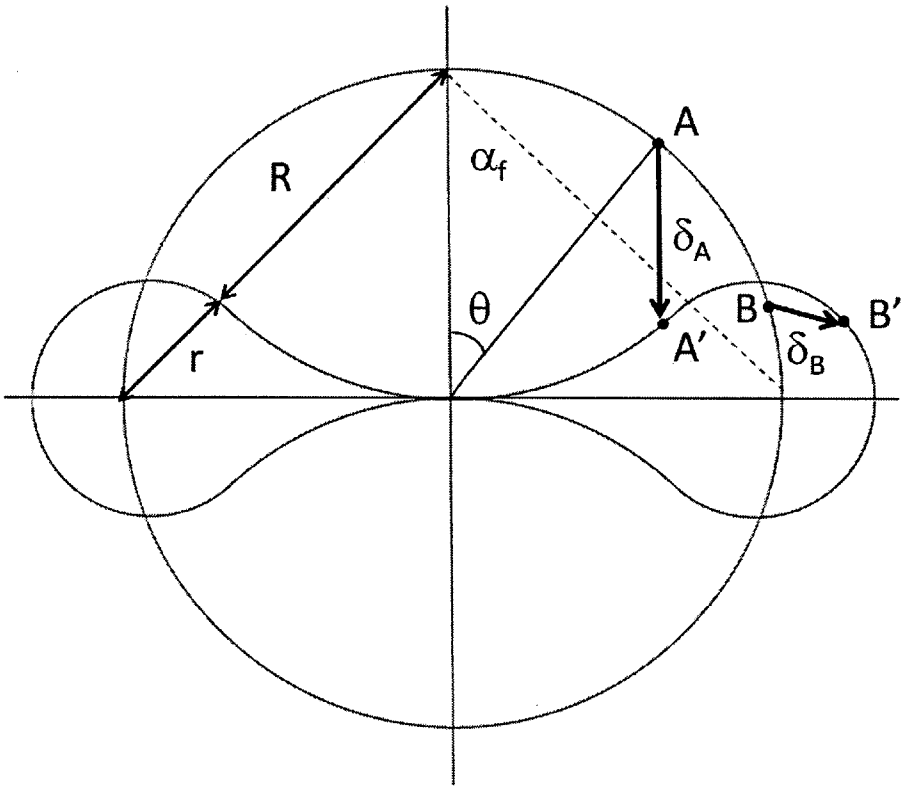

Figure 4-10: MHM geometry for calculating δ.

The general expression for displacement of any point point on the ring is given by Eq. (4.28). After some trigonometric manipulations, the following relationships are obtained (valid at the end of Phase 1):

$$\left(\frac{\delta}{R}\right)^2 = \begin{cases} (2\cos\theta - 1)^2, & 0 \le \theta \le \alpha_f \\ \frac{19}{9} - \frac{2}{3}\sin(3\theta) - 2\sin\theta + \frac{2}{3}\sin\theta\sin(3\theta) + \frac{2}{3}\cos\theta\cos(3\theta), & \alpha_f < \theta \le \frac{\pi}{2} \end{cases} \tag{4.37}$$

The path-independent approximation for the membrane energy dissipation is given by:

$$E_m = \frac{4N_0R^3}{L}\int_0^{\frac{\pi}{2}} \left(\frac{\delta}{R}\right)^2 d\theta \tag{4.38}$$

Substituting Eq. (4.37) and evaluating the integral gives the following result for membrane energy at the end of Phase 1:

$$E_m = 2.38\frac{N_0R^3}{L} \tag{4.39}$$

The path-dependent rate of membrane energy dissipation is given by Eq. (4.10). To make the calculations tractable, the expression for $\left(\frac{\delta}{R}\right)^2$ (Eq. (4.37)) is replaced by a polynomial approximation. Using a Taylor series expansion for $\cos\theta$,

$$\cos\theta \approx 1 - \frac{\theta^2}{2} \tag{4.40}$$

the right-hand side of Eq. (4.37) for $0 \le \theta \le \alpha_f$ can be replaced by:

$$\left[2\left(1 - \frac{\theta^2}{2}\right) - 1\right]^2 = \left(1 - \theta^2\right)^2 \tag{4.41}$$

Figure 4-11 shows the exact function for $\left(\frac{\delta}{R}\right)^2$ (from Eq. (4.37)) , along with the polynomial approximation over the range $0 \le \theta \le 1$. The quantity of interest in calculating E_m is the integral of $\left(\frac{\delta}{R}\right)^2$, or the area under the curve in Fig. 4-11. As

shown in the figure, the portion of the curve beyond $\theta = 1$ contributes little to the total integral. To evaluate the accuracy of the polynomial approximation, the integral of the exact expression was evaluated (equal to 0.595) and compared to the integral of the polynomial approximation (equal to 0.533). Thus, the polynomial approximation underestimates the integral by approximately 10%, a reasonable approximation.

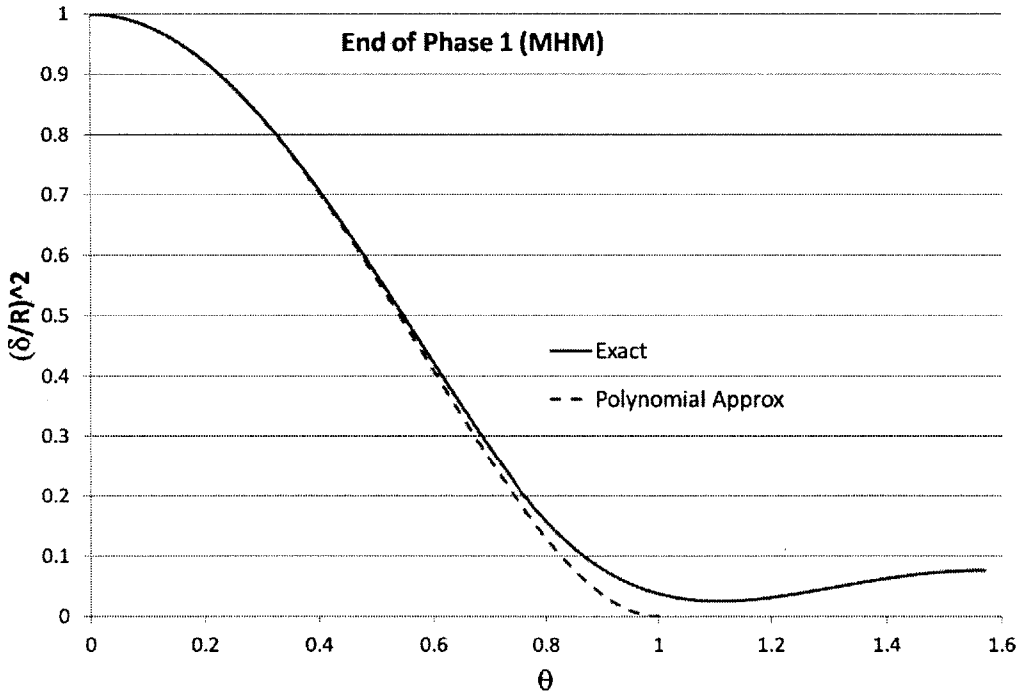

Figure 4-11: MHM displacement at end of Phase 1, with polynomial approximation.

As before, the displacement is assumed to vary linearly with $\frac{w_0}{R}$ (or equivalently, $\frac{\alpha}{\alpha_f}$ from Eq. (2.24)), so:

$$\delta = R\left(1-\theta^2\right)\frac{\alpha}{\alpha_f} = \frac{4R}{\pi}\left(1-\theta^2\right)\alpha \tag{4.42}$$

and

$$\dot{\delta} = \frac{4R}{\pi}\left(1-\theta^2\right)\dot{\alpha} \tag{4.43}$$

Substituting these expressions into Eq. (4.10), again dropping the first term due to fixed end conditions, gives:

$$\begin{aligned}\dot{E_m} &= \frac{128N_0R^3\alpha\dot{\alpha}}{\pi^2 L}\int_0^1\left(1-\theta^2\right)^2 d\theta \\ &= \frac{128N_0R^3\alpha\dot{\alpha}}{\pi^2 L}\left(\frac{8}{15}\right)\end{aligned} \tag{4.44}$$

Integrating with respect to the time-like parameter α gives:

$$E_m = \frac{128N_0R^3}{\pi^2 L}\left(\frac{8}{15}\right)\left(\frac{\alpha^2}{2}\right) \tag{4.45}$$

Finally, substituting $\alpha = \frac{\pi w_0}{4R}$ gives the membrane energy dissipated, as a function of $\frac{w_0}{R}$:

$$E_m = 2.13\frac{N_0R^3}{L}\left(\frac{w_0}{R}\right)^2 \tag{4.46}$$

Note that this result is actually less than the path-independent approximation given by Eq. (4.39). This is because of the polynomial approximation used for $\left(\frac{\delta}{R}\right)^2$ in the path-dependent calculations. Figure 4-11 clearly shows that the polynomial approximation underestimates the exact value for $\left(\frac{\delta}{R}\right)^2$. If the same expressions for $\left(\frac{\delta}{R}\right)^2$ were used in the path-independent and path-dependent calculations, the path-independent result would be lower (as expected). In summary: the Phase 1 membrane energy was calculated three ways, and the results are given in Table 4.3.

Table 4.3: End of Phase 1 membrane energy.

Model	$\mathbf{E}_b$
SHM	$1.964\frac{N_0R^3}{L}$
MHM (path-independent)	$2.38\frac{N_0R^3}{L}$
MHM (path-dependent)	$2.13\frac{N_0R^3}{L}$

4.2.3 Comparison with Numerical Simulation

In order to determine which kinematic model gives a more accurate value for energy dissipation during Phase 1, the results were compared to a numerical simulation for a representative cylinder geometry. Figure 4-12 shows the comparison.

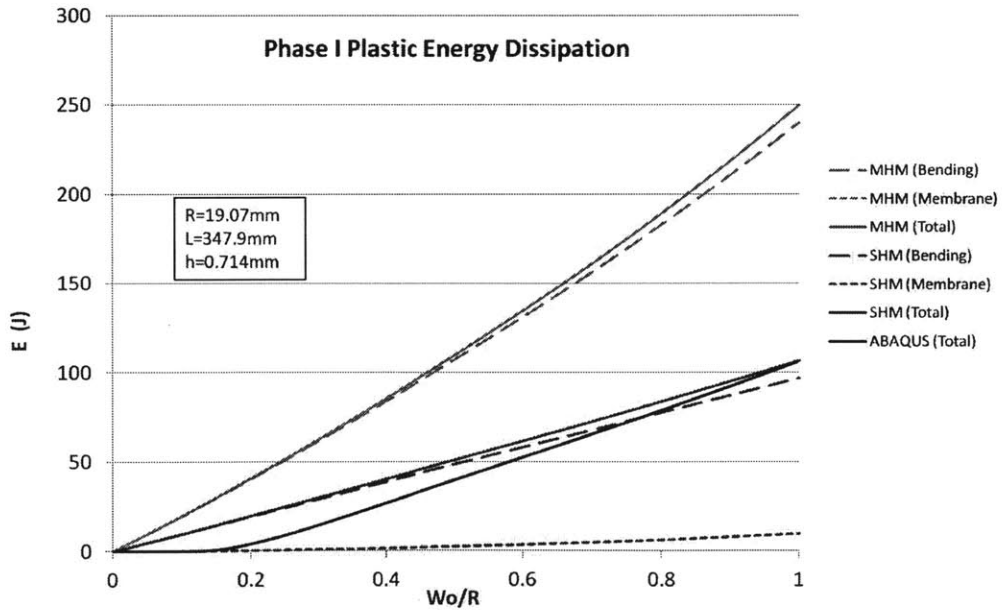

Figure 4-12: Comparison of Phase 1 analytic energy dissipation solutions to numerical simulation.

The following observations are made from Fig. 4-12:

1. Membrane energy dissipation is nearly identical for the two models.
2. For both models, membrane energy is much smaller than bending energy.
3. The MHM bending energy is much larger than SHM bending energy.
4. The MHM grossly overestimates energy dissipation during Phase 1 ($> 100\%$ error compared to ABAQUS).
5. The SHM total energy dissipation is very close to the ABAQUS value at the end of Phase 1.

Observations 3 and 4 are due to the fact that the MHM kinematics cause reverse curvature of some segments of the ring during collapse (i.e., the segment first bends in one direction then bends the other direction later in the collapse). This requires greater bending energy than if the structure moved directly from the initial to final state. Figure 2-10 illustrates the differences between the actual ring kinematics as seen in ABAQUS, and the kinematics predicted by the MHM. The overall goal of the analytic energy calculations is to accurately predict the energy dissipation for a given cylinder geometry, without the need for numerical simulation. Therefore, since the SHM energy calculations more closely match the numerical simulation (which in turn is assumed to accurately model the real cylinder and the real energy dissipation), the SHM will be used for Phase 1 throughout the remainder of this thesis.

4.3 Phase 2

Phase 2 energy dissipation is calculated using the MHM only, because the SHM is not applicable during Phase 2 (or 3). The MHM kinematics during Phase 2 are shown in Fig. 2-11. The important geometric relationships and assumptions for the model

(first presented in Chapter 2) are:

$$\alpha_f = \frac{\pi}{4} \tag{4.47}$$

$$R_1 = 3r \tag{4.48}$$

and

$$r = \frac{R}{3} - \frac{2b}{3\pi} \tag{4.49}$$

Each quarter of the ring is composed of three segments:

- A straight segment with length b.
- A curved arc with radius R_1 and angle $\alpha_f = \frac{\pi}{4}$.
- A curved arc with radius r and angle $\frac{3\pi}{4}$.

4.3.1 Bending Energy

The instantaneous rate of bending energy dissipation is given by Eq. (4.3). The curvature for each of the ring segments is:

$$\kappa = \begin{cases} 0, & \theta R \leq b \\ -\dfrac{1}{R_1}, & b < \theta R \leq b + \dfrac{\pi}{4} R_1 \\ \dfrac{1}{r}, & b + \dfrac{\pi}{4} R_1 < \theta R \leq \dfrac{\pi}{2} R \end{cases} \tag{4.50}$$

and the rate of curvature is:

$$\dot{\kappa} = \begin{cases} 0, & \theta R \leq b \\ \dfrac{\dot{R}_1}{R_1^2} = -\dfrac{\frac{2}{\pi}\dot{b}}{\left(R - \frac{2b}{\pi}\right)^2}, & b < \theta R \leq b + \dfrac{\pi}{4} R_1 \\ -\dfrac{\dot{r}}{r^2} = \dfrac{\frac{2}{3\pi}\dot{b}}{\left(\frac{R}{3} - \frac{2b}{3\pi}\right)^2}, & b + \dfrac{\pi}{4} R_1 < \theta R \leq \dfrac{\pi}{2} R \end{cases} \tag{4.51}$$

Each quarter-ring has two moving plastic hinges. For each hinge, $\dot{\theta}$ is calculated as follows:

$$\begin{aligned}\dot{\theta}_1 &= v_1 \mid \kappa_2 - \kappa_1 \mid \\ &= \dot{b}\left(\frac{1}{R_1}\right) \\ &= \frac{\pi\dot{b}}{\pi R - 2b}\end{aligned} \tag{4.52}$$

and

$$\begin{aligned}\dot{\theta}_2 &= v_2 \mid \kappa_3 - \kappa_2 \mid \\ &= \dot{b}\sqrt{\left(1 - \frac{\sqrt{2}}{\pi}\right)^2 + \left(\frac{2}{\pi} - \frac{\sqrt{2}}{\pi}\right)^2}\left(\frac{1}{r} + \frac{1}{R_1}\right) \\ &= 0.58\dot{b}\left(\frac{1}{\frac{R}{3} - \frac{2b}{3\pi}} + \frac{1}{R - \frac{2b}{\pi}}\right) \\ &= \frac{2.32\pi\dot{b}}{\pi R - 2b}\end{aligned} \tag{4.53}$$

Substituting these expressions into Eq. (4.3) gives the following result for the instantaneous rate of bending energy dissipation for a single cross-sectional ring:

$$\dot{E}_b = 4M_0\left[\int_{\frac{b}{R}}^{\left(\frac{b}{R}+\frac{\pi R_1}{4R}\right)} \frac{-2\dot{b}R}{\pi\left(R - \frac{2b}{\pi}\right)^2}d\theta + \int_{\left(\frac{b}{R}+\frac{\pi R_1}{4R}\right)}^{\frac{\pi}{2}} \frac{2\dot{b}R}{3\pi\left(\frac{R}{3} - \frac{2b}{3\pi}\right)^2}d\theta + \frac{\pi\dot{b}}{\pi R - 2b} + \frac{2.32\pi\dot{b}}{\pi R - 2b}\right] \tag{4.54}$$

which simplifies to:

$$\dot{E}_b = \frac{21.28\pi M_0\dot{b}}{\pi R - 2b} \tag{4.55}$$

Integrating with respect to time gives (for a single cross-sectional ring):

$$E_b = \int_0^t \dot{E}_b dt = 10.64\pi M_0 \ln\left(\frac{\pi R}{\pi R - 2b}\right) \tag{4.56}$$

Equation (4.56) is a function of x, because $b = b(x)$. This necessitates an analytic expression for $b(x)$. During Phase 2, the center cross-sectional ring is flattening (described by the parameter b_0), while at the same time the tube is flattening longitudinally (described by the parameter ζ_2). The function $b(x)$ defines the boundary of the flattened portion of the tube (see Fig. 4-13).

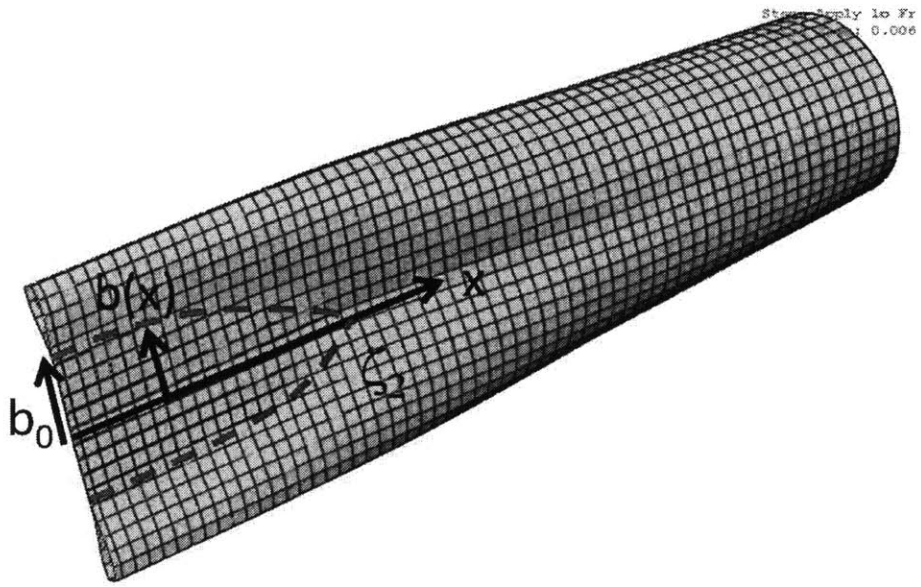

Figure 4-13: Cylinder geometry during Phase 2.

A number of different ABAQUS numerical simulations were evaluated to determine the best form of the function $b(x)$. Linear, parabolic, cubic, and square shape functions were considered. It was determined that the parabolic shape best matched the numerical simulations. Two new non-dimensional parameters were introduced:

$$\bar{b_0} = \frac{b_0}{R} \tag{4.57}$$

and

$$\bar{\zeta_2} = \frac{\zeta_2}{L} \tag{4.58}$$

The final values of these dimensionless parameters (i.e., at the end of Phase 2) are:

$$\bar{b_{0_f}} = \frac{b_{0_f}}{R} \tag{4.59}$$

and

$$\bar{\zeta_{2_f}} = \frac{\zeta_{2_f}}{L} \tag{4.60}$$

Then the function $b(x)$ may be written as:

$$b(x) = \begin{cases} \sqrt{b_0^2 - \frac{R\bar{b_{0_f}} b_0 x}{\zeta_{2_f} L}}, & x \leq \frac{\bar{\zeta_{2_f}} L b_0}{b_{0_f} R} \\ 0, & x > \frac{\bar{\zeta_{2_f}} L b_0}{b_{0_f} R} \end{cases} \tag{4.61}$$

Note that b_0 is the time-like parameter for Phase 2, so that $b(x)$ also varies with time.

In order to calculate the total bending energy for the cylinder, Eq. (4.56) must be integrated over the cylinder length. The integral is divided into 2 sections: (1) $0 \leq x \leq \zeta_2$ (the partially flattened portion), and (2) $\zeta_2 < x \leq L$ (which looks just like the end of Phase 1). The bending energy for section (1) is found by substituting

Eq. (4.61) into Eq. (4.56) as follows:

$$E_{b(1)} = 2(10.64)\pi M_0 \int_0^{\frac{\bar{\zeta_{2_f}} L b_0}{\bar{b_{0_f}} R}} \ln \left[\frac{\pi R}{\pi R - 2\left(b_0^2 - \frac{R\bar{b_{0_f}} b_0 x}{\bar{\zeta_{2_f}} L}\right)^{\frac{1}{2}}} \right] dx \tag{4.62}$$

The bending energy for section (2) is given by Eq. (4.18), with $\frac{w_0}{R} = 1$ and L replaced by $(L - \frac{\bar{\zeta_{2_f}} L b_0}{\bar{b_{0_f}} R})$:

$$E_{b(2)} = 6.22 M_0 L \left(1 - \frac{\bar{\zeta_{2_f}} b_0}{\bar{b_{0_f}} R}\right) \tag{4.63}$$

Simplifying the integral and combining the two sections gives the following expression for total Phase 2 bending energy:

$$E_{b,tot} = 21.28\pi M_0 \left\{ \frac{\bar{\zeta_{2_f}} L b_0}{\bar{b_{0_f}} R} \ln(\pi R) + \frac{\bar{\zeta_{2_f}} L}{2R\bar{b_{0_f}} b_0} \left[b_0^2 (1 - 2\ln(\pi R - 2b_0)) + \ldots \right.\right.$$
$$\left.\left. \ldots + \frac{\pi^2 R^2}{2} (-\ln(\pi R) + \ln(\pi R - 2b_0)) + \pi R b_0 \right] \right\} + 6.22 M_0 L \left(1 - \frac{\bar{\zeta_{2_f}} b_0}{\bar{b_{0_f}} R}\right) \tag{4.64}$$

4.3.2 Membrane Energy

The exact path-dependent Phase 2 membrane energy cannot be directly calculated as the bending energy was, because of the complexity and uncertainty in mapping the displacement of individual points during Phase 2. Therefore, a path-independent approximation is used in conjunction with an assumption that the longitudinal strain varies linearly with the angular coordinate, θ. The strains of the leading generator ($\theta = 0$) and the edge generator ($\theta = \frac{\pi}{2}$) are calculated from the definition of logarithmic strain:

$$\varepsilon = \frac{L'^2 - L^2}{2L^2} \tag{4.65}$$

where L' is the deformed length of the generator. Figure 4-14 shows the relative locations of the leading and edge generators, along with the geometry for calculating the strain.

From Fig. 4-14b, the deformed length of the leading generator is:

$$L' = \zeta_2 + \sqrt{(L - \zeta_2)^2 + R^2} \tag{4.66}$$

and the strain ε becomes:

$$\varepsilon_{(\theta=0)} = \frac{2\zeta_2^2 + 2\zeta_2\sqrt{(L - \zeta_2)^2 + R^2} - 2L\zeta_2 + R^2}{2L^2} \tag{4.67}$$

From Fig. 4-14c, the deformed length of the edge generator is:

$$L' = \sqrt{L^2 + (a - R)^2} \tag{4.68}$$

and from the MHM kinematics,

$$\begin{aligned} a &= b_0 + R_1 + r \\ &= b_0 + 4r \\ &= \frac{4}{3}R + b_0\left(1 - \frac{8}{3\pi}\right) \end{aligned} \tag{4.69}$$

Then

$$L' = \sqrt{L^2 + \left[\frac{R}{3} + b_0\left(1 - \frac{8}{3\pi}\right)\right]^2} \tag{4.70}$$

and the strain ε becomes:

$$\varepsilon_{(\theta=\frac{\pi}{2})} = \frac{\frac{R^2}{9} + \frac{2Rb_0}{3}\left(1 - \frac{8}{3\pi}\right) + b_0^2\left(1 - \frac{8}{3\pi}\right)^2}{2L^2} \tag{4.71}$$

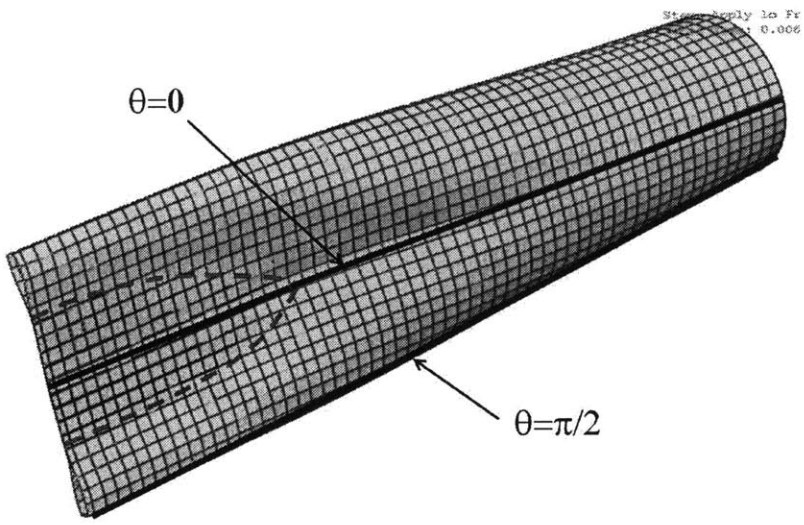

(a) Positions of leading and edge generators.

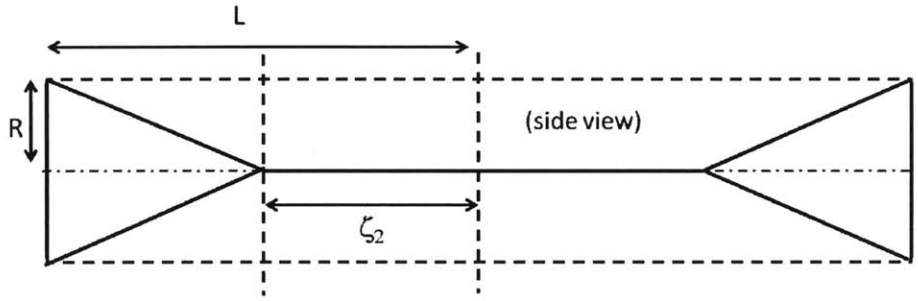

(b) Leading generator ($\theta = 0$).

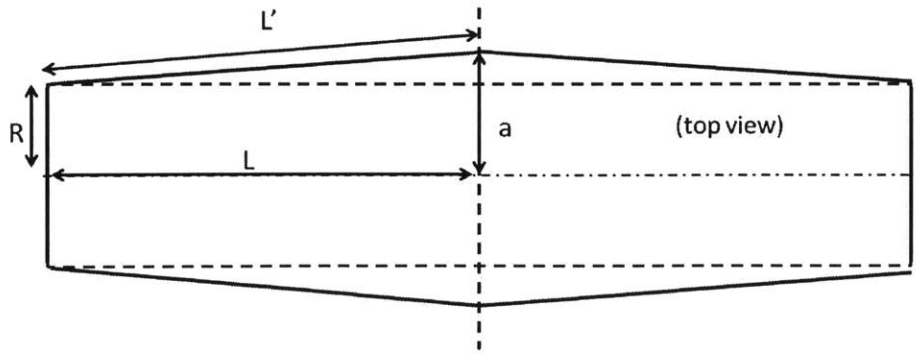

(c) Edge generator ($\theta = \frac{\pi}{2}$).

Figure 4-14: Leading and edge generators for strain calculations.

Assuming that the strain varies linearly between $\theta = 0$ and $\theta = \frac{\pi}{2}$, then:

$$\varepsilon(\theta) = \varepsilon_{(\theta=0)} + \frac{\theta}{\frac{\pi}{2}} \left(\varepsilon_{(\theta=\frac{\pi}{2})} - \varepsilon_{(\theta=0)} \right) \tag{4.72}$$

From Eq. (4.12), the total membrane energy for the cylinder is given by:

$$E_m = 8N_0 L \int_0^{\frac{\pi}{2}} \varepsilon(\theta) R d\theta \tag{4.73}$$

Substituting Eq. (4.72) and simplifying the integral gives the following expression for total membrane energy dissipated during Phase 2:

$$E_{m,tot} = \frac{\pi N_0 R}{L} \left[\frac{2\bar{\zeta_{2_f}}^2 L^2 b_0^2}{\bar{b_{0_f}}^2 R^2} + \frac{2\bar{\zeta_{2_f}} L b_0}{\bar{b_{0_f}} R} \sqrt{\left(L - \frac{\bar{\zeta_{2_f}} L b_0}{\bar{b_{0_f}} R} \right)^2 + R^2} - \ldots \right.$$
$$\left. \ldots - \frac{2\bar{\zeta_{2_f}} L^2 b_0}{\bar{b_{0_f}} R} + R^2 + \frac{R^2}{9} + \frac{2Rb_0}{3} \left(1 - \frac{8}{3\pi} \right) + b_0^2 \left(1 - \frac{8}{3\pi} \right)^2 \right] \tag{4.74}$$

4.4 Phase 3

The deformation during Phase 3 is described by the time-like parameter ζ_3. The shape of the flattened portion at the end of Phase 2, described by the function $b(x)$, is frozen and translates along the longitudinal length. The shape of the Phase 3 deformation is shown in Fig. 4-15. The cylinder can be divided into three segments as shown in the figure. Segment (1) is a flattened section with uniform width $\bar{b_{0_f}} R$ and length ζ_3. Segment (2) is a flattened section bounded by $b(x)$, given by Eq. (4.61). Segment (3) is identical to the end of Phase 1, but over the shortened length $(L - \zeta_2 - \zeta_3)$. The end of Phase 3 (i.e., the final collapse shape) is defined by the dimensionless term:

$$\bar{\zeta_{3_f}} = \frac{\zeta_{3_f}}{L} \tag{4.75}$$

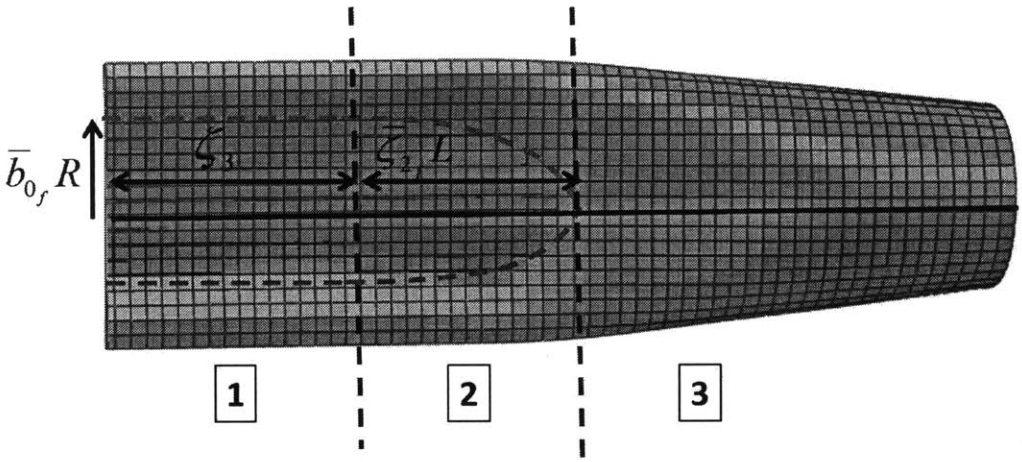

Figure 4-15: Cylinder geometry during Phase 3.

4.4.1 Bending Energy

The Phase 3 bending energy is the sum of the energy dissipated in each of the three length segments. For segment (1), the bending energy is found by integrating Eq. (4.56) over the length ζ_3, with $b(x) = \bar{b_{0_f}} R$ (constant):

$$E_{b,1} = 21.28\pi M_0 \ln\left(\frac{\pi R}{\pi R - 2\bar{b_{0_f}} R}\right)\zeta_3 \tag{4.76}$$

For segment (2), the bending energy is given by Eq. (4.62), with $b_0 = \bar{b_{0_f}} R$. The bending energy for segment (3) is given by Eq. (4.18), with $\frac{w_0}{R} = 1$ and L replaced by $(L - \bar{\zeta_{2_f}} L - \zeta_3)$. Combining the three segments gives the following expression for total bending energy during Phase 3:

$$E_{b,tot} = 21.28\pi M_0 \left\{ \ln\left(\frac{\pi R}{\pi R - 2\bar{b_{0_f}} R}\right)\zeta_3 + \bar{\zeta_{2_f}} L \left[\frac{1}{2} + \frac{\pi}{2\bar{b_{0_f}}} + \ln\left(\frac{\pi R}{\pi R - 2\bar{b_{0_f}} R}\right)\left(1 - \frac{\pi^2}{4\bar{b_{0_f}}^2}\right)\right]\right\} + \\ ... + 6.22 M_0 L \left(1 - \bar{\zeta_{2_f}} - \frac{\zeta_3}{L}\right) \tag{4.77}$$

4.4.2 Membrane Energy

The Phase 3 membrane energy is calculated in the same manner and with the same assumptions as Phase 2. The strain of the leading generator, as a function of ζ_3, is:

$$\varepsilon_{(\theta=0)} = \frac{2\left(\zeta_3 + \bar{\zeta_{2_f}} L\right)^2 + 2\left(\zeta_3 + \bar{\zeta_{2_f}} L\right)\sqrt{(L - \zeta_3 - \bar{\zeta_{2_f}} L)^2 + R^2} - 2L\left(\zeta_3 + \bar{\zeta_{2_f}} L\right) + R^2}{2L^2} \tag{4.78}$$

For the edge generator ($\theta = \frac{\pi}{2}$), the deformed length is:

$$L' = \zeta_3 + \sqrt{(L - \zeta_3)^2 + \left[\frac{R}{3} + \bar{b_{0_f}} R\left(1 - \frac{8}{3\pi}\right)\right]^2} \tag{4.79}$$

and the strain is:

$$\varepsilon_{(\theta=\frac{\pi}{2})} = \left(\frac{1}{2L^2}\right)\left[2\zeta_3^2 + 2\zeta_3\sqrt{(L-\zeta_3)^2 + \left[\frac{R}{3} + \bar{b_{0_f}}R\left(1-\frac{8}{3\pi}\right)\right]^2} - 2\zeta_3 L + \frac{R^2}{9} + \ldots\right.$$
$$\left. \ldots + \frac{2R^2\bar{b_{0_f}}}{3}\left(1-\frac{8}{3\pi}\right) + R^2\bar{b_{0_f}}^2\left(1-\frac{8}{3\pi}\right)^2\right] \quad (4.80)$$

Substituting these expressions into Eqs. (4.72) and (4.73) and simplifying gives the following result for total membrane energy dissipated during Phase 3:

$$E_{m,tot} = \frac{\pi N_0 R}{L}\left[4\zeta_3^2 + 4\zeta_3\bar{\zeta_{2_f}}L + 2\bar{\zeta_{2_f}}^2L^2 + 2\left(\zeta_3 + \bar{\zeta_{2_f}}L\right)\sqrt{\left(L-\bar{\zeta_{2_f}}L-\zeta_3\right)^2 + R^2} - \ldots\right.$$
$$\ldots - 2\bar{\zeta_{2_f}}L^2 - 4\zeta_3 L + \frac{10R^2}{9} + 2\zeta_3\sqrt{(L-\zeta_3)^2 + \left[\frac{R}{3} + \bar{b_{0_f}}R\left(1-\frac{8}{3\pi}\right)\right]^2} + \ldots$$
$$\left. \ldots + \frac{2R^2\bar{b_{0_f}}}{3}\left(1-\frac{8}{3\pi}\right) + R^2\bar{b_{0_f}}^2\left(1-\frac{8}{3\pi}\right)^2\right] \quad (4.81)$$

4.5 Validation of Analytic Results

The resulting equations for energy dissipation for all three phases are summarized below:

Phase 1 (time-like parameter w_0):

$$E_{b,tot} = 6.22 M_0 L\frac{w_0}{R}$$

$$E_{m,tot} = 1.964\frac{N_0 R^3}{L}\left(\frac{w_0}{R}\right)^2$$

Phase 2 (time-like parameter b_0):

$$E_{b,tot} = 21.28\pi M_0 \left\{ \frac{\bar{\zeta_{2_f}} L b_0}{\bar{b_{0_f}} R} \ln(\pi R) + \frac{\bar{\zeta_{2_f}} L}{2R\bar{b_{0_f}} b_0} \left[b_0^2 \left(1 - 2\ln(\pi R - 2b_0)\right) + ... \right.\right.$$
$$\left.\left. ... + \frac{\pi^2 R^2}{2} \left(-\ln(\pi R) + \ln(\pi R - 2b_0)\right) + \pi R b_0 \right] \right\} + 6.22 M_0 L \left(1 - \frac{\bar{\zeta_{2_f}} b_0}{\bar{b_{0_f}} R}\right)$$

$$E_{m,tot} = \frac{\pi N_0 R}{L} \left[\frac{2\bar{\zeta_{2_f}}^2 L^2 b_0^2}{\bar{b_{0_f}}^2 R^2} + \frac{2\bar{\zeta_{2_f}} L b_0}{\bar{b_{0_f}} R} \sqrt{\left(L - \frac{\bar{\zeta_{2_f}} L b_0}{\bar{b_{0_f}} R}\right)^2 + R^2} - ... \right.$$
$$\left. ... - \frac{2\bar{\zeta_{2_f}} L^2 b_0}{\bar{b_{0_f}} R} + R^2 + \frac{R^2}{9} + \frac{2Rb_0}{3} \left(1 - \frac{8}{3\pi}\right) + b_0^2 \left(1 - \frac{8}{3\pi}\right)^2 \right]$$

Phase 3 (time-like parameter ζ_3):

$$E_{b,tot} = 21.28\pi M_0 \left\{ \ln\left(\frac{\pi R}{\pi R - 2\bar{b_{0_f}} R}\right) \zeta_3 + \bar{\zeta_{2_f}} L \left[\frac{1}{2} + \frac{\pi}{2\bar{b_{0_f}}} + \ln\left(\frac{\pi R}{\pi R - 2\bar{b_{0_f}} R}\right) \left(1 - \frac{\pi^2}{4\bar{b_{0_f}}^2}\right) \right] \right\} +$$
$$... + 6.22 M_0 L \left(1 - \bar{\zeta_{2_f}} - \frac{\zeta_3}{L}\right)$$

$$E_{m,tot} = \frac{\pi N_0 R}{L} \left[4\zeta_3^2 + 4\zeta_3 \bar{\zeta_{2_f}} L + 2\bar{\zeta_{2_f}}^2 L^2 + 2\left(\zeta_3 + \bar{\zeta_{2_f}} L\right) \sqrt{\left(L - \bar{\zeta_{2_f}} L - \zeta_3\right)^2 + R^2} - ... \right.$$
$$... - 2\bar{\zeta_{2_f}} L^2 - 4\zeta_3 L + \frac{10R^2}{9} + 2\zeta_3 \sqrt{(L - \zeta_3)^2 + \left[\frac{R}{3} + \bar{b_{0_f}} R \left(1 - \frac{8}{3\pi}\right)\right]^2} + ...$$
$$\left. ... + \frac{2R^2 \bar{b_{0_f}}}{3} \left(1 - \frac{8}{3\pi}\right) + R^2 \bar{b_{0_f}}^2 \left(1 - \frac{8}{3\pi}\right)^2 \right]$$

Each phase's energy equations are a function of a different time-like parameter. In order to plot the energy dissipation over the complete collapse (for comparison with numerical simulations), it is necessary to use a common, continuous, monotonically increasing time-like parameter. The cylinder internal volume (V) is one such parameter, and can be readily calculated using the kinematic model assumptions.

4.5.1 Volume Calculations

The cylinder volume during each phase was calculated as a function of the same time-like parameter as the energy dissipation.

Phase 1

The time-like parameter for Phase 1 is w_0. Referring to Fig. 4-6, the area of any cross-sectional ring may be written as:

$$A(x) = 4\left[\left(\frac{1}{2}\right)\sqrt{2}R\cos\alpha(x)\sqrt{2}R\sin\alpha(x) + R^2\left(\frac{\pi}{4} - \frac{1}{2}\right)\right] \tag{4.82}$$

and $\alpha(x)$ is given by Eq. (4.16). The total cylinder volume is:

$$V = 2\int_0^L A(x)dx \tag{4.83}$$

Substituting and evaluating the integral gives the Phase 1 volume as:

$$V_1 = R^2L\left[2\pi - 4 + \frac{2.574\sin\left(\frac{\pi w_0}{2R}\right)}{\left(\frac{w_0}{R}\right)}\right] \tag{4.84}$$

Phase 2

Just like the Phase 2 bending energy calculations, the Phase 2 integral is divided into 2 sections: (1) $0 \leq x \leq \zeta_2$ (the partially flattened portion), and (2) $\zeta_2 < x \leq L$ (which looks just like the end of Phase 1). Referring the Fig. 2-11, the area of a cross-sectional ring in section (1) may be written as:

$$A = 4\left[\frac{R_1^2}{2} - \frac{\pi R_1^2}{8} + \pi r^2\left(\frac{3}{8}\right)\right] \tag{4.85}$$

Substituting the expressions for R_1 and r and simplifying gives:

$$A(x) = 2.144\left(\frac{R^2}{9} - \frac{4Rb(x)}{9\pi} + \frac{4b(x)^2}{9\pi^2}\right) \tag{4.86}$$

Substituting the expression for $b(x)$ (Eq. (4.61)) and integrating from x=0 to x=ζ_2 gives:

$$V = 0.476\frac{\bar{\zeta_{2_f}} L b_0}{\bar{b_{0_f}}}\left(R + \frac{2b_0^2}{\pi^2 R} - \frac{8b_0}{3\pi}\right) \tag{4.87}$$

The volume of section (2) is identical to Eq. (4.84), with $\frac{w_0}{R} = 1$ and L replaced by $(L - \zeta_2)$:

$$V = 4.857R^2 L\left(1 - \frac{\bar{\zeta_{2_f}} b_0}{\bar{b_{0_f}} R}\right) \tag{4.88}$$

Combining the two sections gives the Phase 2 volume as:

$$V_2 = 0.476\frac{\bar{\zeta_{2_f}} L b_0}{\bar{b_{0_f}}}\left(R + \frac{2b_0^2}{\pi^2 R} - \frac{8b_0}{3\pi}\right) + 4.857R^2 L\left(1 - \frac{\bar{\zeta_{2_f}} b_0}{\bar{b_{0_f}} R}\right) \tag{4.89}$$

Phase 3

As shown in Fig. 4-15, the cylinder during Phase 3 can be divided into three sections. The volume of section (1) is a linear function of ζ_3. Section (1) has constant cross-sectional area, given by Eq. (4.86) with $b(x) = b_{0_f}$, and length ζ_3:

$$V = 0.476R^2\zeta_3\left(1 - \frac{4\bar{b_{0_f}}}{\pi} + \frac{4\bar{b_{0_f}}^2}{\pi^2}\right) \tag{4.90}$$

The volume of section (2) is constant, and is given by Eq. (4.87) with $b_0 = b_{0_f}$:

$$V = 0.476\bar{\zeta_{2_f}} L R^2\left(1 + \frac{2\bar{b_{0_f}}^2}{\pi^2} - \frac{8\bar{b_{0_f}}}{3\pi}\right) \tag{4.91}$$

The volume of section (3) is identical to Eq. (4.88) but with $(L - \zeta_2)$ replaced with $(L - \zeta_{2_f} - \zeta_3)$:

$$V = 4.857R^2L\left(1 - \bar{\zeta_{2_f}} - \frac{\zeta_3}{L}\right) \tag{4.92}$$

Combining the three sections gives the Phase 3 volume as:

$$V_3 = 0.476R^2\zeta_3\left(1 - \frac{4\bar{b_{0_f}}}{\pi} + \frac{4\bar{b_{0_f}}^2}{\pi^2}\right) + 0.476\bar{\zeta_{2_f}}LR^2\left(1 + \frac{2\bar{b_{0_f}}^2}{\pi^2} - \frac{8\bar{b_{0_f}}}{3\pi}\right) + 4.857R^2L\left(1 - \bar{\zeta_{2_f}} - \frac{\zeta_3}{L}\right) \tag{4.93}$$

The volume relationships for all three phases are plotted in Fig. 4-16. The x-axis is the percent change in volume, and the y-axis is the relevant dimensionless parameter for each phase. This figure illustrates the relative amount of volume change per phase.

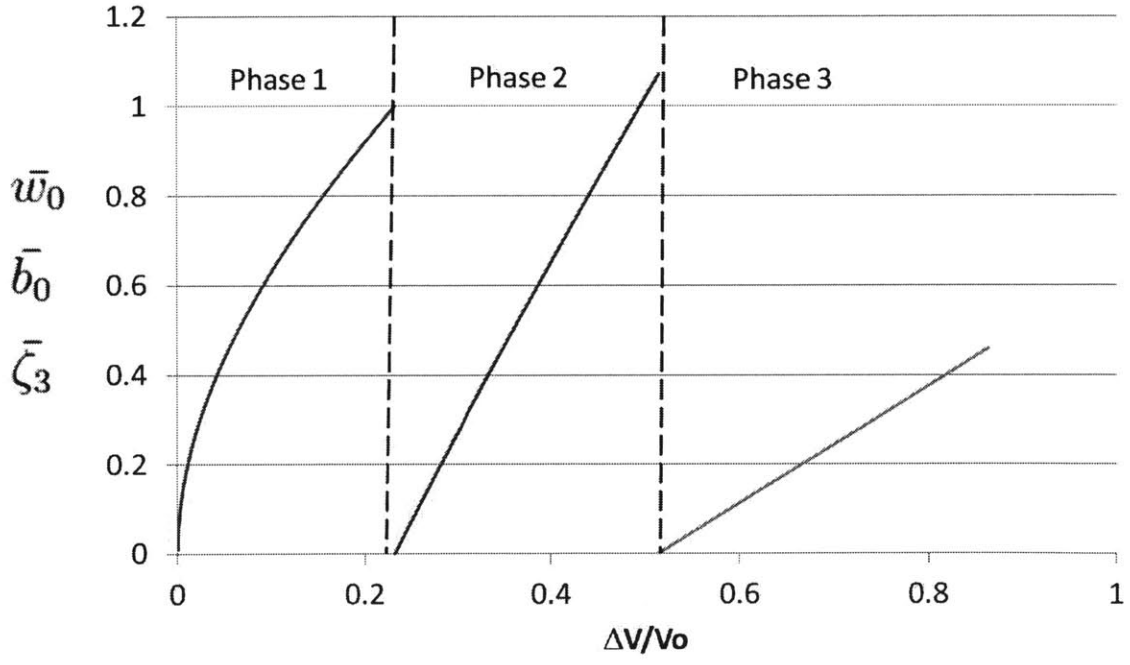

Figure 4-16: Relative change in volume for the three collapse phases.

4.5.2 Comparison with Numerical Simulation

In order to validate the accuracy of the analytic solutions, they are compared to numerical simulations for two specific cylinder geometries. The energy dissipation is plotted vs. percent volume change ($\Delta V/V_0$). The analytic solutions are plotted parametrically, where both energy dissipation and volume are functions of the same time-like parameter. The ABAQUS results are also plotted parametricallly, where the energy and volume are recorded as functions of time. Figure 4-17 shows the comparison.

There is a visible discontinuity in the analytic solutions from the end of Phase 1 to the start of Phase 2. This is not unexpected, since the Phase 1 and Phase 2 solutions use different kinematic models and assumptions. The most significant discontinuity occurs in the membrane energy, and is due primarily to the linear strain assumption used in the Phase 2 and 3 solutions.

Correction for Linear Strain Assumption in Phase 2 and 3

Recall that the Phase 2 and 3 membrane energy calculations used a path-independent approximation and assumed a linear change in strain from $\theta = 0$ to $\theta = \frac{\pi}{2}$. This assumption overestimates the actual strain for intermediate angles, as indicated by the jump increase in membrane energy at the start of Phase 2. The Phase 1 membrane energy calculation did not use the linear assumption, because it was straightforward to find the actual strain for any angle θ (see Eq. (4.32)).

In order to quantify the error introduced by the linear strain assumption, the Phase 1 membrane energy was re-calculated using the linear assumption and compared to the more exact solution previously derived. The resulting expression for Phase 1 membrane energy using the linear strain assumption is:

$$E_{m,tot} = \frac{2\pi N_0 R^2}{L}\left(w_0 + R - \sqrt{R^2 + 2Rw_0 - w_0^2}\right) \tag{4.94}$$

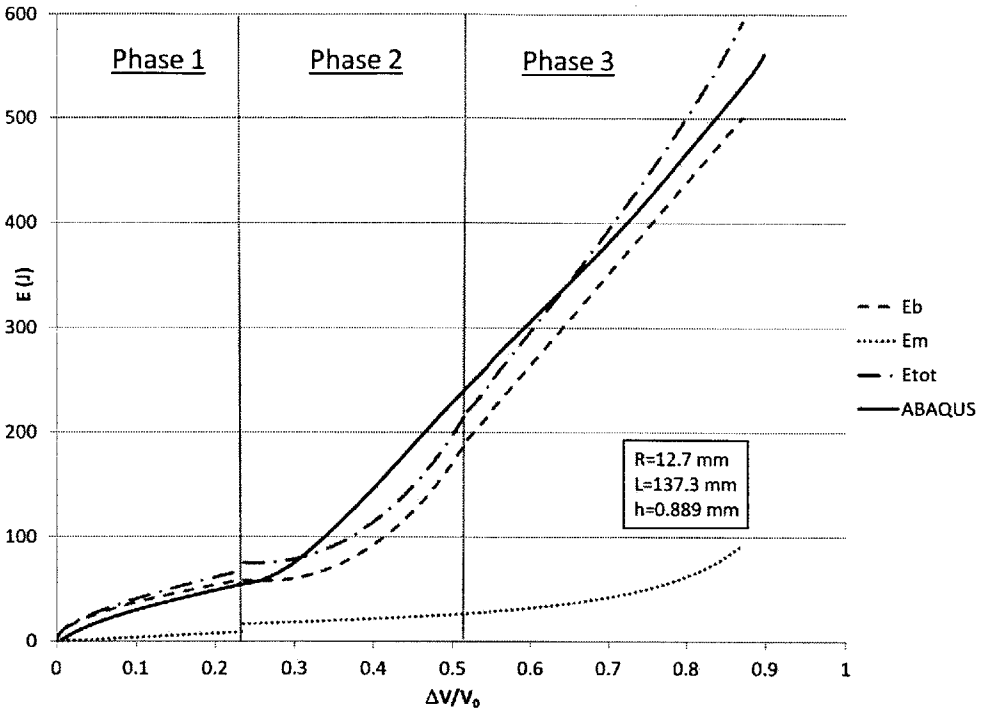

(a) Cylinder with $R/h = 14.3$, $L/R = 10.8$.

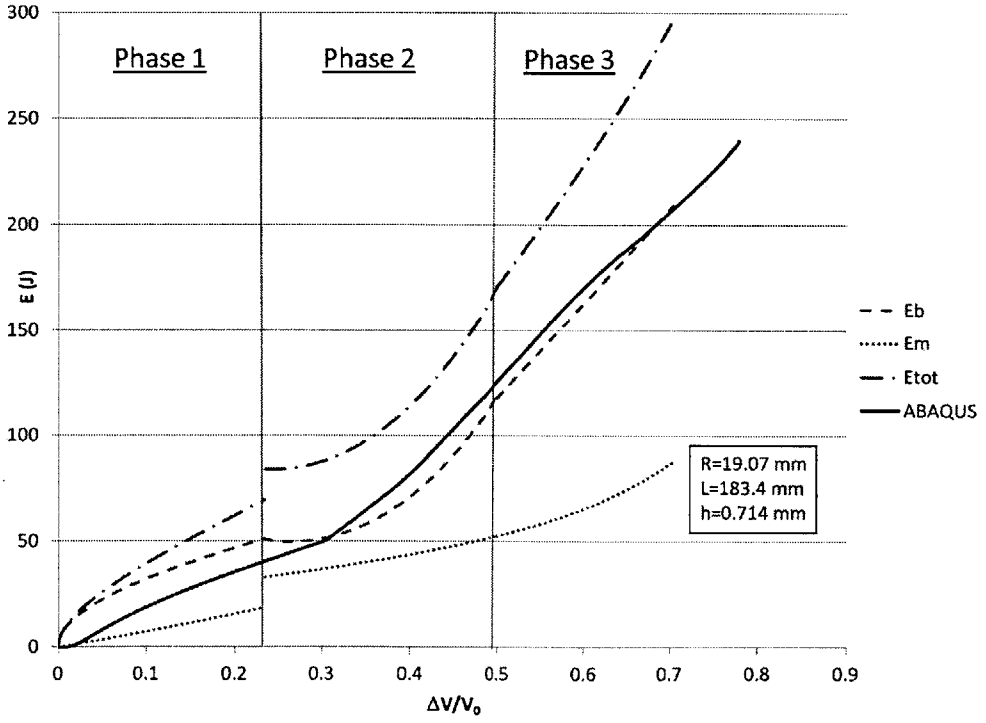

(b) Cylinder with $R/h = 26.7$, $L/R = 9.6$.

Figure 4-17: Comparison of analytic and numerical energy dissipation.

The exact Phase 1 membrane energy solution was:

$$E_{m,tot} = 1.964\frac{N_0 R^3}{L}\left(\frac{w_0}{R}\right)^2$$

Comparing these two expressions at the end of Phase 1 (when $w_0 = R$) gives:

$$E_{m,linear} \approx 1.87 E_{m,exact} \tag{4.95}$$

It is reasonable to assume that this ratio will hold throughout the cylinder collapse; therefore, a correction factor can be applied to the Phase 2 and 3 membrane energy solutions to correct for the overestimation of the linear strain assumption. When the Phase 2 and 3 membrane solutions are divided by the correction factor (1.87), the discontinuity across Phase 1-2 is almost entirely eliminated (see Fig. 4-18).

Both cylinders in Figs. 4-17 and 4-18 are made of aluminum 6061-T6.

4.5.3 Determining $\bar{b_{0_f}}$, $\bar{\zeta_{2_f}}$ and $\bar{\zeta_{3_f}}$

The Phase 2 and 3 analytic solutions are functions of $\bar{b_{0_f}}$, $\bar{\zeta_{2_f}}$ and $\bar{\zeta_{3_f}}$ as well as the applicable time-like parameter for each phase. The parameters $\bar{b_{0_f}}$, $\bar{\zeta_{2_f}}$ and $\bar{\zeta_{3_f}}$ are constant for a given cylinder geometry and loading, and the values were determined from numerical simulation, by visually measuring the deformed shape of the cylinder at the end of Phase 2 and 3. The accuracy of the parameters is limited by the element size (approximately 1 mm x 1 mm in most cases). By examining several different cylinder simulations, it was determined that the values vary, as summarized in Table 4.4.

It was originally assumed that the same average value of $\bar{b_{0_f}}$, $\bar{\zeta_{2_f}}$ and $\bar{\zeta_{3_f}}$ could be used for all cylinder geometries. To test this hypothesis, the energy dissipation was calculated using different values of the dimensionless parameters spanning the ranges in Table 4.4. Two different cylinder geometries were evaluated, and the results

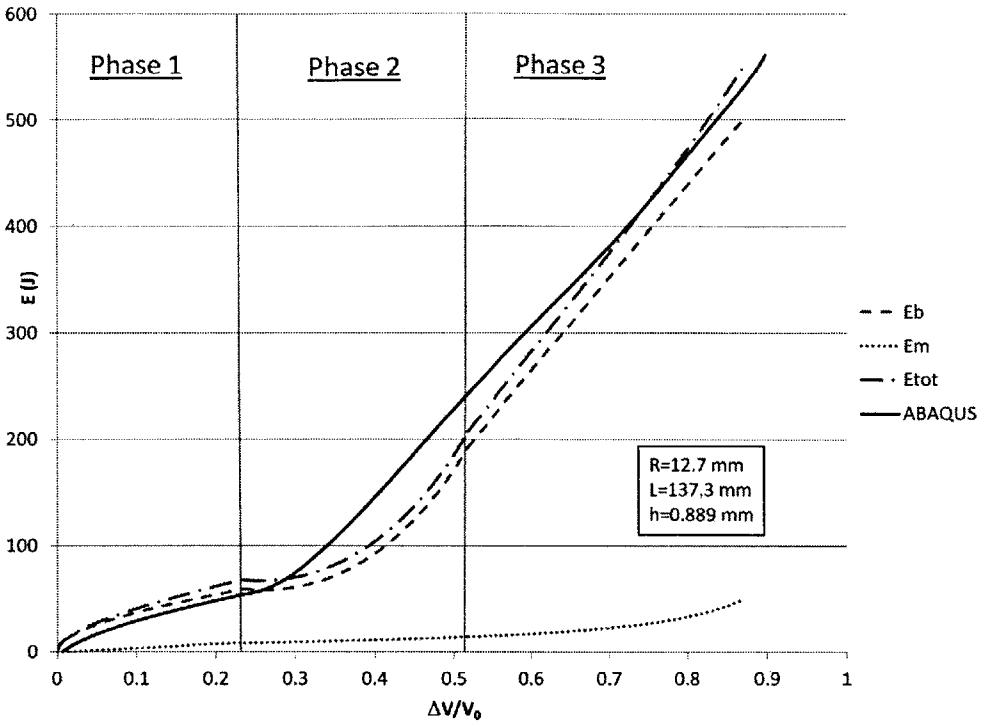

(a) Cylinder with $R/h = 14.3$, $L/R = 10.8$.

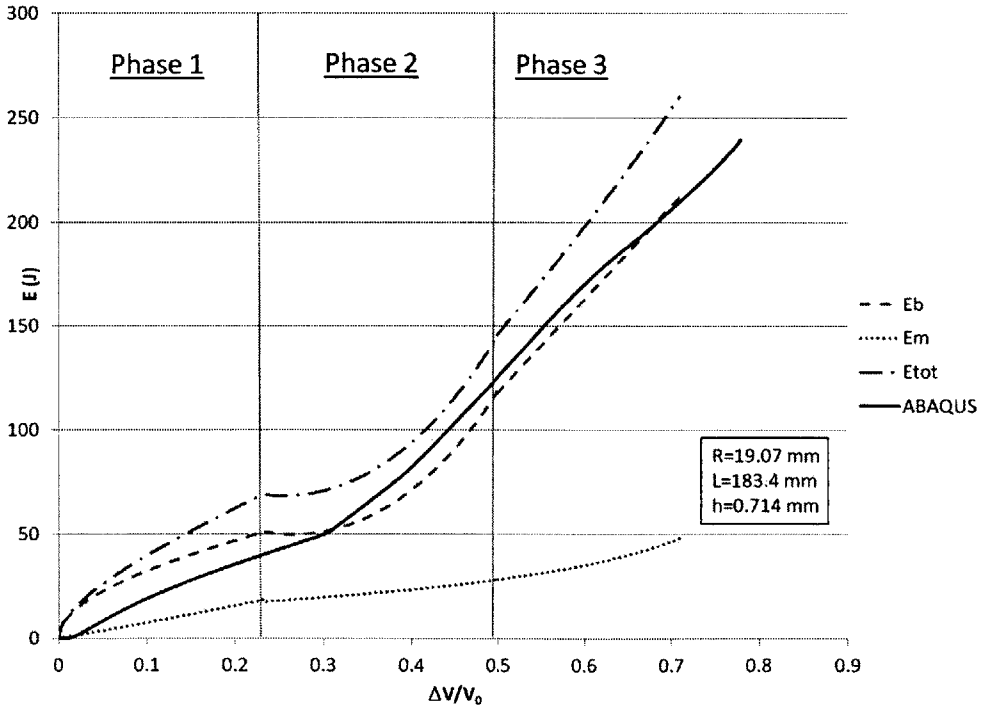

(b) Cylinder with $R/h = 26.7$, $L/R = 9.6$.

Figure 4-18: Comparison of analytic and numerical energy dissipation (with correction factor for linear strain assumption).

Table 4.4: Dimensionless parameter ranges.

Parameter	Range
b_{0_f}	0.7-1.07
ζ_{2_f}	0.28-0.5
ζ_{3_f}	0.16-0.46

are summarized in Table 4.5. The analysis revealed that varying the dimensionless parameters over the full range changed the energy calculations by more than 2.25x (125% error). Therefore, it is clear that the assumption of a single value for all cylinders is not valid.

Table 4.5: Sensitivity of energy dissipation to non-dimensional parameter values.

	b_{0_f}	$\zeta_{2_f} + \zeta_{3_f}$	$E_{tot} = E_b + E_m$
R/h=26.7	0.7	0.62	255 J
L/R=9.6	0.95	0.74	377 J
	1.07	0.86	577 J
R/h=14.3	0.7	0.62	265 J
L/R=10.8	0.95	0.74	394 J
	1.07	0.86	597 J

A total of nine combinations were calculated for each cylinder geometry (only three each are shown in Table 4.5), and the results are presented graphically as 3D surface plots in Fig. 4-19.

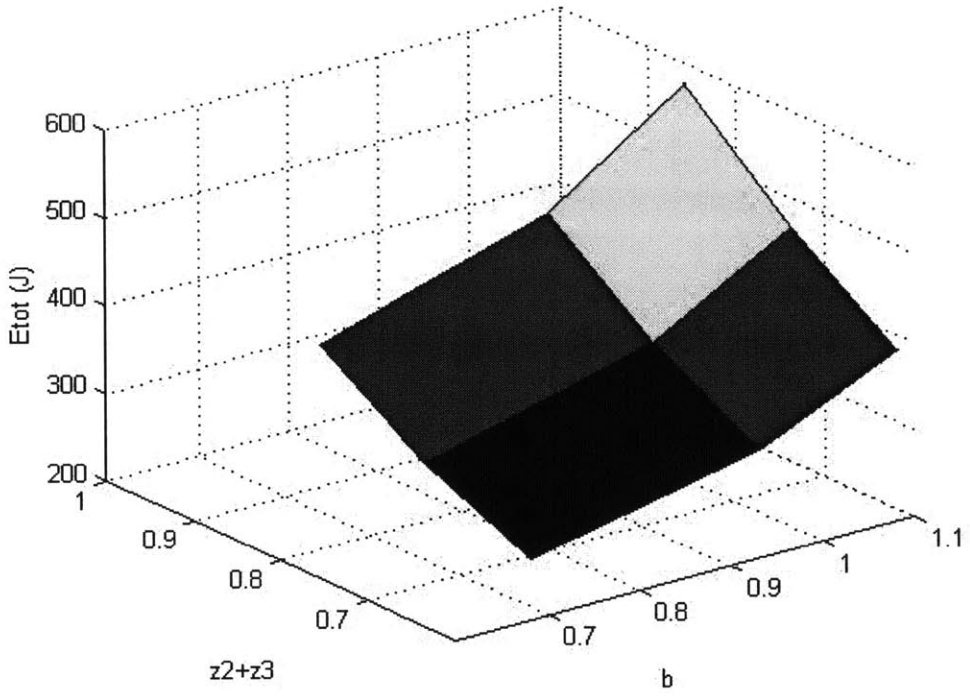

(a) Cylinder with $R/h = 26.7$, $L/R = 9.6$.

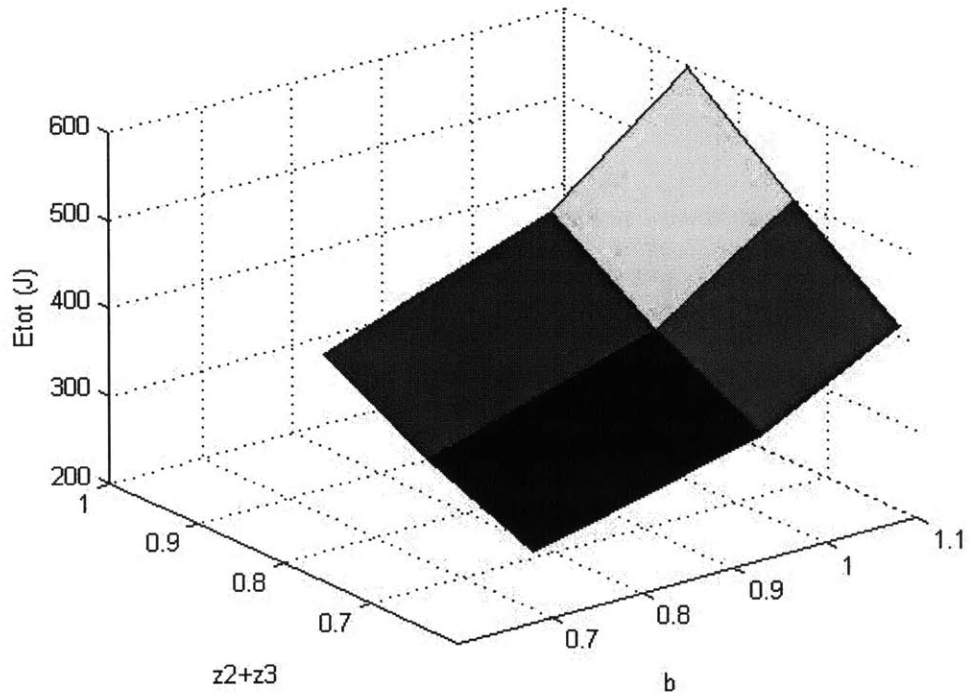

(b) Cylinder with $R/h = 14.3$, $L/R = 10.8$.

Figure 4-19: Variation of energy dissipation over a range of $\bar{b_{0_f}}$ and $\bar{\zeta_{2_f}} + \bar{\zeta_{3_f}}$.

Since a single dimensionless parameter value for all cylinder geometries is not valid, a study was conducted to determine how the parameters vary and what the principal driving factors are. Fourteen different cylinder geometries were analyzed, spanning the R/h and L/R ranges typical of U.S. Navy implodables. For each geometry, an ABAQUS model was created and a static buckling analysis was run to determine the minimum buckling pressure of the cylinder. Then a dynamic analysis was run with that buckling pressure applied. The dimensionless parameters ($\bar{b_{0_f}}$, $\bar{\zeta_{2_f}}$ and $\bar{\zeta_{3_f}}$) were determined from the collapsed cylinder shapes. The data indicated that the non-dimensional parameters are strongly dependent on the geometric ratios R/h and L/R. Figure 4-20 presents the data plotted versus R/h, for different values of L/R. Consistent trends are apparent in the data, so that the plots can be used to determine the proper value of the non-dimensional parameters for any cylinder geometry within the given ranges of R/h and L/R.

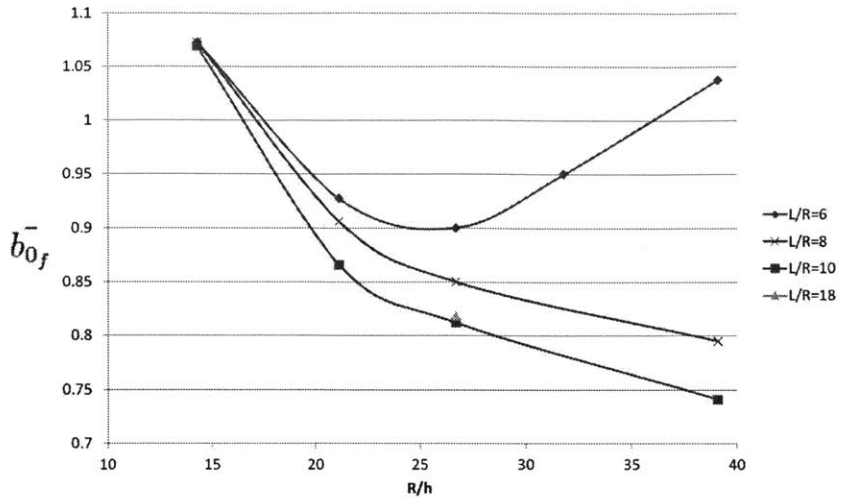

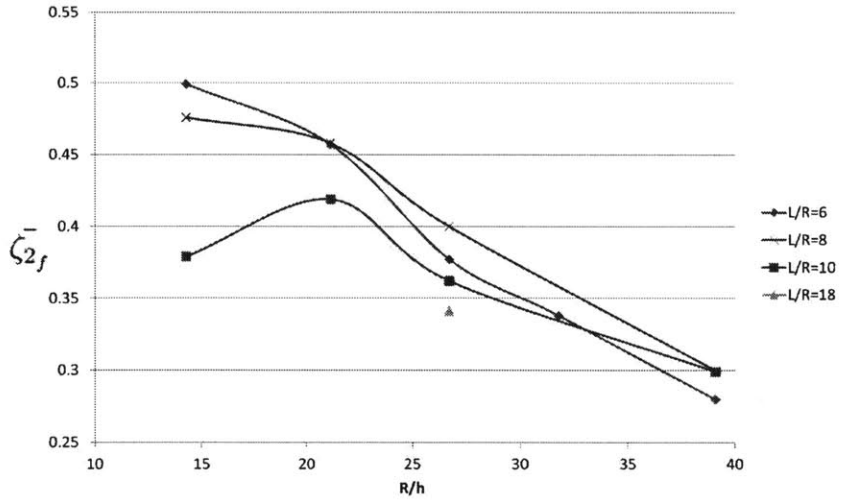

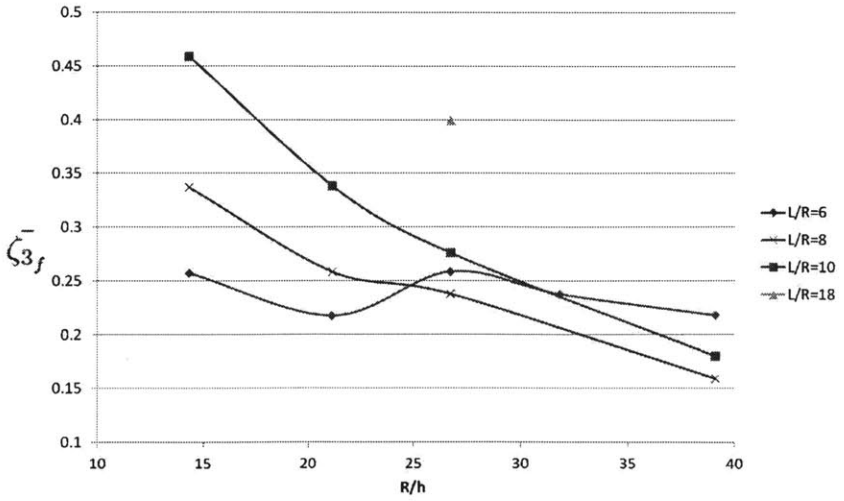

Figure 4-20: $\bar{b_{0_f}}$, $\bar{\zeta_{2_f}}$, and $\bar{\zeta_{3_f}}$ as functions of R/h and L/R.

4.6 Energy Dissipation as Percentage of Total External Work

The overall energy balance for an underwater implosion problem was given by Eq. (2.36). An upper bound on the external work done on the cylinder can be calculated by assuming that the external pressure is constant on the cylinder surface throughout the collapse. With this assumption, the external work may be written as:

$$E_{ext} = W = \int pdV = p\Delta V \tag{4.96}$$

It is informative to calculate the ratio of plastic energy dissipated to external work, since this gives an indication of how much energy remains to potentially be released in the implosion pulse. This ratio was calculated for two example cylinders, and results are shown in Table 4.6.

Table 4.6: Energy dissipation as percentage of external work.

	R/h=26.7 L/R=9.6	**R/h=14.3 L/R=10.8**
p	1.1 MPa	6.4 MPa
E_{tot}	258 J	550 J
W	326 J	775 J
E_{tot}/W	0.79	0.71

These results indicate that plastic energy dissipated is a relatively constant percentage of external work (71%-79%). Of course, the actual external work done on the cylinder will be less than that calculated by Eq. (4.96). The actual pressure on the cylinder surface decreases during collapse because of the corresponding fluid movement, as described in section 1.2. Thus, the ratio of plastic energy dissipated to actual external work will be greater than that shown in Table 4.6. Chapter 5 addresses the fluid-structure interaction and the varying pressure on the cylinder surface.

4.7 Summary and Conclusions

The expressions for plastic energy dissipation derived in this chapter, and summarized in section 4.5, are reasonably accurate compared to numerical simulation results. The final energy values (analytic and numerical) for the two examples presented in Fig. 4-18 are summarized in Table 4.7.

Table 4.7: Comparison of analytic and numerical energy dissipation values.

	R/h=26.7 L/R=9.6	**R/h=14.3 L/R=10.8**
Analytic	258 J	550 J
Numerical	237 J	562 J
% Error	8.9%	2.1%

The % error (calculated as the difference divided by the numerical value) is less for the cylinder with lower R/h, indicating that the analytic solutions are more accurate for thicker-walled cylinders. Furthermore, the analytic solution for the thicker cylinder underestimates the numerical value, while the thinner cylinder overestimates. Recall from Chapter 2 that there are two primary effects that cause error in the analytic solutions: 1) the assumed yield condition causes overestimation of energy dissipation, and 2) neglect of shear causes underestimation of energy dissipation. Suh [4] showed that shear energy dissipation is inversely proportional to R/h (i.e., shear is more significant for thicker-walled cylinders). Thus, it is expected that the analytic solution for a thicker cylinder will be closer to (and possibly even less than) the numerical value than a comparable thinner-walled cylinder. The results in Table 4.7 are consistent with this expectation.

The analytic solutions are strongly dependent on the values of the dimensionless parameters $\bar{b_{0_f}}$, $\bar{\zeta_{2_f}}$ and $\bar{\zeta_{3_f}}$. For a given cylinder geometry, these parameter values may be determined from the graphs in Fig. 4-20. This makes the derived solutions semi-analytic rather than purely analytic, because they rely on information extracted

from numerical simulations.

The semi-analytic solutions are also directly proportional to the material flow stress, σ_0. Therefore, it is critical that an accurate value of flow stress be determined and used for the specific material of the cylinder.

The results (both semi-analytic and numerical) show that plastic energy dissipation constitutes at least 70% of the total external work done on the cylinder. Therefore, less than 30% is available to be released in the implosion pulse. This conclusion is further refined in Chapter 5 by considering the fluid-structure interaction.

Chapter 5

Simplified Fluid-Structure Interaction

The basic nature of fluid-structure interaction (FSI) problems was described in section 1.2. In general, FSI problems such as underwater implosion are too complex for analytic or semi-analytic solutions. In this chapter, a novel explicit time-stepping methodology is introduced, which yields a pseudo-coupled analytic solution for the fluid pressure history and implosion pulse energy.

5.1 Overview of Simplified FSI Methodology

This section provides a brief overview of the simplified FSI approach developed in this thesis. Details of the individual steps are provided in subsequent sections. The goal of this simplified FSI methodology is to obtain an estimate of the energy in the implosion pulse. The overall energy balance for an implosion event is:

$$E_{pulse} = W - E_{int} - E_{air} \tag{5.1}$$

where E_{pulse} is the energy released in the implosion pulse, W is the work done on the cylinder by the fluid, E_{int} is the plastic energy dissipated by the cylinder, and E_{air} is the energy required to compress the internal air. Expressions for E_{int} and E_{air} were developed in chapters 4 and 2, respectively. The difficulty comes in accurately calculating W, because the fluid pressure acting on the cylinder surface varies both spatially and temporally during the implosion event. During implosion, the cylinder structural walls rapidly collapse until they contact the opposite wall and motion stops. As the structure collapses, the surrounding fluid accelerates to follow the structure. The moving fluid creates a dynamic pressure in the vicinity of the cylinder that is negative in sign. The dynamic pressure adds to the constant hydrostatic pressure to give the total fluid pressure acting on the surface.

Recall that at the end of Chapter 4, it was shown that the plastic energy dissipation accounts for about 70-80% of the total available energy of an implosion event (see Table 4.6). However, the analysis in Chapter 4 assumed a constant pressure acting on the cylinder surface and thus overestimated the work done on the cylinder by the fluid (which is equivalent to the total available energy). The analysis in this chapter estimates the dynamic fluid pressure on the surface to give a more accurate estimate of the implosion pulse energy.

It is impossible to analytically calculate the fluid pressure acting on the surface, as a function of time and space, throughout the whole implosion event. However, a reasonable approximation can be obtained during Phase 1, because the pressure varies more slowly and predictably during Phase 1 than during the remainder of the event[1]. The overall energy balance at the end of Phase 1 is:

$$KE = W - E_{int} - E_{air} \tag{5.2}$$

where KE is the kinetic energy of the system (cylinder plus surrounding fluid). It is

[1]Refer to Fig. 1-1 for a typical pressure history of an implosion event.

assumed that all kinetic energy of the system is eventually converted into implosion pulse energy. The maximum kinetic energy during the implosion event occurs just after the end of Phase 1, as shown in Fig. 5-1. The kinetic energy continues to increase slightly beyond the end of Phase 1, because portions of the cylinder are still accelerating inward even though the center section has stopped. The fundamental hypothesis of the simplified FSI methodology is that the kinetic energy at the end of Phase 1 will equal the energy released in the implosion pulse.

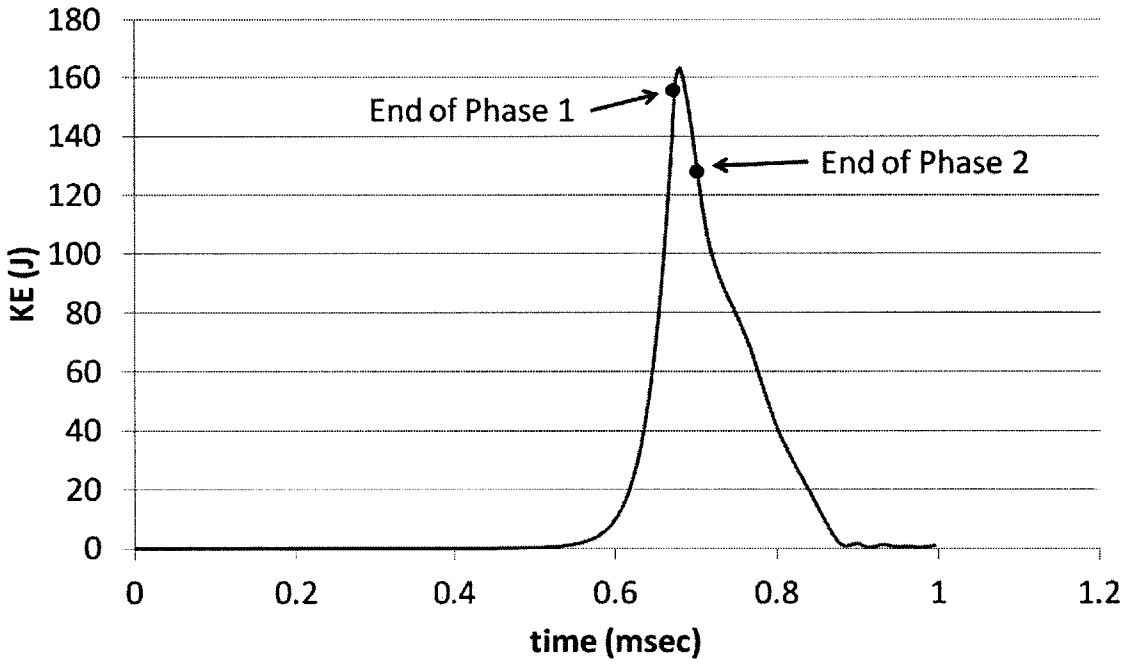

Figure 5-1: Kinetic energy vs. time (from representative ABAQUS simulation).

The difference between the fluid pressure acting on the surface and the varying (diminishing) pressure needed to continue plastic deformation of the cylinder (i.e., the critical pressure, described in detail below) at any instant is called excess pressure. The excess pressure is the driving force that continues to accelerate the cylinder inward. The relationship between the various pressures during Phase 1 is illustrated in Fig. 5-2.

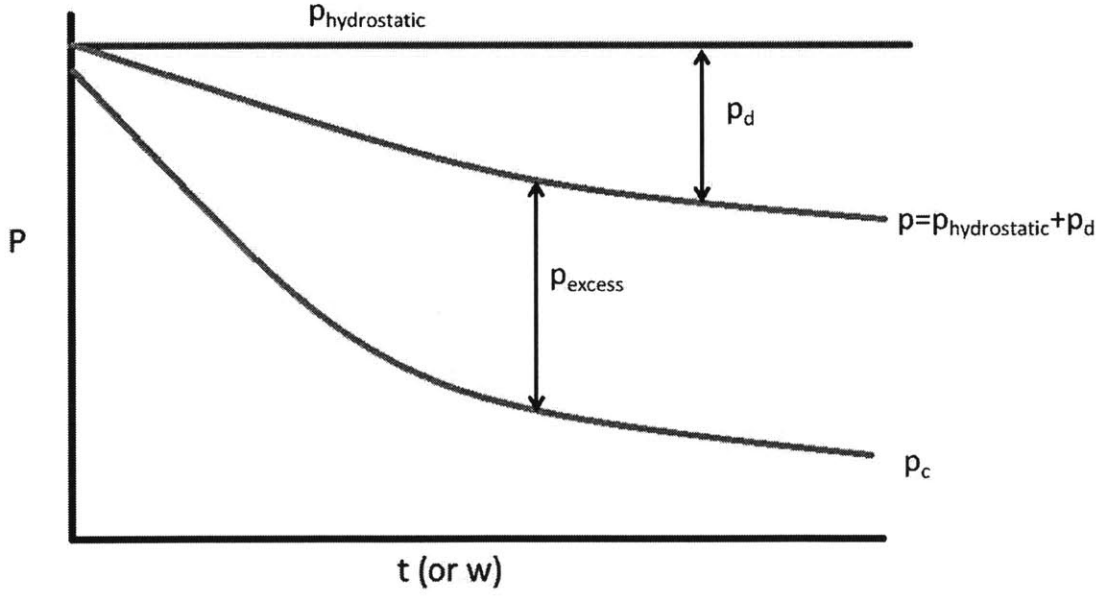

p_d=dynamic fluid pressure
p=actual fluid pressure acting on the surface
p_c=critical pressure for the cylinder
p_{excess}=pressure causing acceleration of cylinder

Figure 5-2: Pressures during cylinder collapse (Phase 1).

The simplified FSI methodology consists of the following steps:

1. Calculate the critical pressure of the cylinder, p_c, using the energy dissipation expressions derived in Chapter 4.

2. Use the explicit time-stepping methodology to estimate the fluid dynamic pressure at any time. The dynamic pressure is caused by fluid velocity. The fluid velocity is found by starting from known initial conditions and assuming constant acceleration (caused by the fluid pressure) over each small time interval.

3. Add the fluid dynamic pressure to the hydrostatic pressure to obtain the total fluid pressure acting on the cylinder surface at any time.

4. Calculate the work done on the cylinder by the fluid during Phase 1:

$$W = \int_0^t p(t)\dot{V}(t)dt \tag{5.3}$$

5. Calculate the kinetic energy of the system from Eq. 5.2. The implosion pulse energy is very nearly equal to this value of kinetic energy.

5.2 Cylinder Critical Pressure

The critical pressure (p_c) of the cylinder is defined as the external pressure required to begin the collapse, and to continue the collapse once it has started. The critical pressure decreases as the displacement (w_0) increases. The quasi-static equation of equilibrium (principle of virtual velocities) is:

$$\dot{E_{ext}} = \dot{E_{int}} + \dot{E_{air}} \tag{5.4}$$

The energy required to compress the internal air (E_{air}) was given by Eq. (2.32) (assuming adiabatic compression). Taking the time derivative of this equation gives:

$$\dot{E_{air}} = -p_{i_0}\left(\frac{V_0}{V}\right)^{\gamma}\dot{V} \tag{5.5}$$

The volume during Phase 1, as a function of $\frac{w_0}{R}$, was given by Eq. (4.84). The time derivative of this expression is:

$$\dot{V} = 2.574R^3L\left[\frac{\cos\left(\frac{\pi w_0}{2R}\right)\left(\frac{\pi \dot{w}_0}{2R}\right)w_0 - \sin\left(\frac{\pi w_0}{2R}\right)\dot{w}_0}{w_0^2}\right] \tag{5.6}$$

The original cylinder volume is $V_0 = 2\pi R^2 L$. Substituting these expressions into Eq. (5.5) gives:

$$\dot{E_{air}} = -p_{i_0}\left(\frac{2\pi}{2\pi - 4 + \frac{2.574\sin\left(\frac{\pi w_0}{2R}\right)}{\frac{w_0}{R}}}\right)^{\gamma}\dot{V} \tag{5.7}$$

By definition, p_c is the pressure that maintains the equilibrium of Eq. (5.4). So:

$$p_c = \frac{\dot{E_b} + \dot{E_m} + \dot{E_{air}}}{\dot{V}} \tag{5.8}$$

The solutions for Phase 1 energy dissipation (E_b and E_m) were given in section 4.5. Taking time derivatives of these expressions gives:

$$\dot{E_b} = 6.22M_0\frac{L}{R}\dot{w}_0 \tag{5.9}$$

and

$$\dot{E_m} = 3.93N_0\frac{R}{L}w_0\dot{w}_0 \tag{5.10}$$

Substituting into Eq. (5.8) and simplifying gives:

$$p_c = \frac{-6.22M_0\frac{L}{R} - 3.93N_0\frac{R}{L}w_0}{2.574RL\left[\frac{\cos\left(\frac{\pi w_0}{2R}\right)\left(\frac{\pi w_0}{2R}\right) - \sin\left(\frac{\pi w_0}{2R}\right)}{\left(\frac{w_0}{R}\right)^2}\right]} + p_{i_0}\left(\frac{2\pi}{2\pi - 4 + \frac{2.574\sin\left(\frac{\pi w_0}{2R}\right)}{\frac{w_0}{R}}}\right)^{\gamma} \quad (5.11)$$

Note that $\dot{V} \leq 0$ for $0 \leq \frac{w_0}{R} \leq 1$. The (-) signs in Eq. (5.11) account for this, so that the resulting pressure is positive. Figure 5-3 plots Eq. (5.11) for an example cylinder. The three individual components (E_b, E_m, and E_{air}) are plotted, along with the total. It is clear from the figure that the majority of the required external pressure is due to bending energy. This is consistent with Fig. 4-18, which showed that bending energy is much more significant than membrane energy. As expected, the critical pressure drops rapidly as the cylinder collapse progresses.

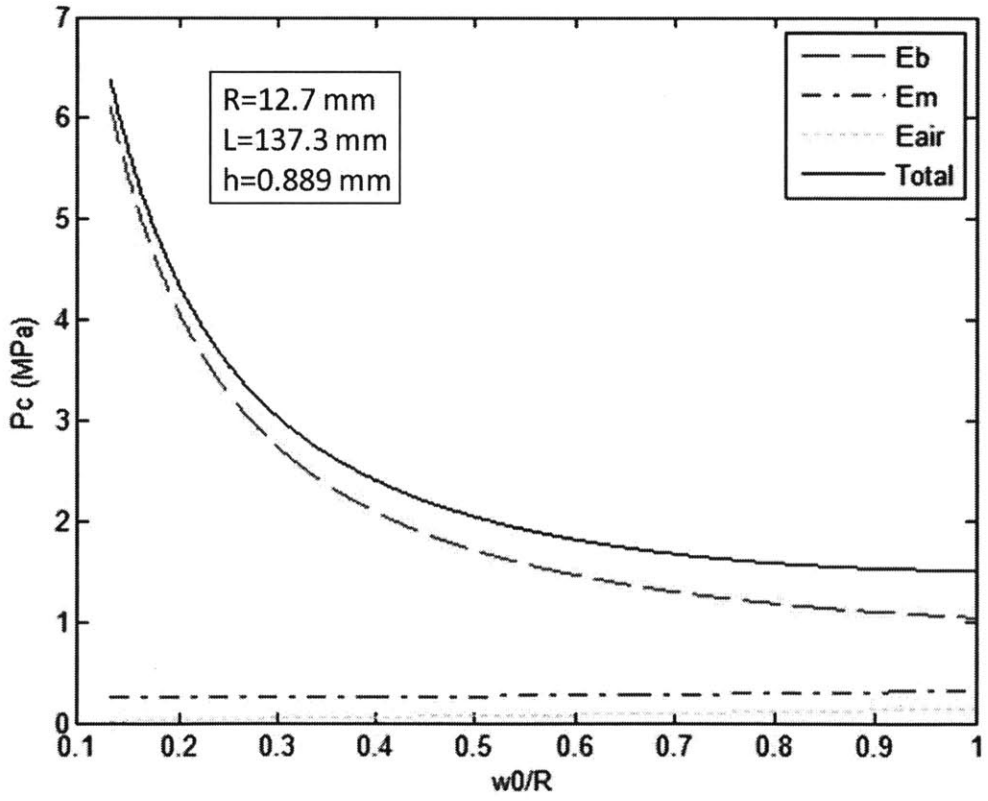

Figure 5-3: Critical pressure (p_c) during Phase 1.

The above analysis (specifically Eq. (5.11)) assumes that the external pressure is spatially uniform. In reality, different portions of the cylinder will have different velocities during collapse, so the dynamic pressure (and consequently the total fluid pressure) will vary over the surface. Therefore, the critical pressure calculated is really the spatial average over the entire cylinder surface.

5.3 Explicit Time-Stepping Methodology

For each infinitesimal piece of cylinder material, the excess pressure will cause acceleration, $\ddot{w}$:

$$p_{excess} = (p - p_c) = m\ddot{w} \tag{5.12}$$

where m is the mass per unit area.

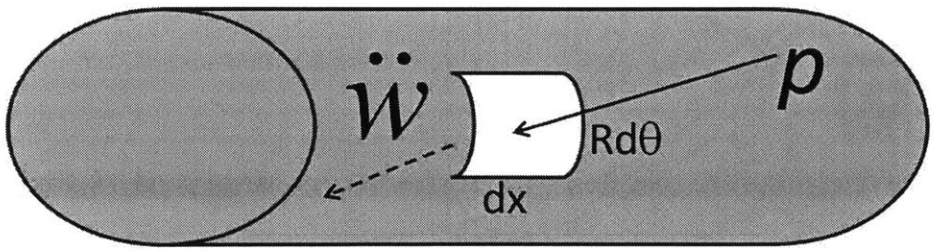

Figure 5-4: Acceleration of infinitesimal material patch.

If the time interval, Δt, is sufficiently small, then the acceleration may be considered constant during the time interval, so that:

$$\dot{w}_n = \dot{w}_{n-1} + \ddot{w}_{n-1}\Delta t \tag{5.13}$$

and

$$w_n = w_{n-1} + \dot{w}_{n-1}\Delta t + \frac{1}{2}\ddot{w}_{n-1}\Delta t^2 \tag{5.14}$$

The assumption of constant acceleration over Δt allows for the explicit calculation of the problem parameters at any time t starting from known initial conditions.

In order to calculate the fluid dynamic pressure from the surface velocity $\dot{w}$, potential flow conditions are assumed. Potential flow theory is valid for incompressible, inviscid, irrotational flows. A flow may be considered incompressible if the Mach number is $\ll 1$. For typical underwater implosion problems, the maximum cylinder surface velocity (which is equal to the maximum fluid velocity, v) is on the order of 100 m/s. The speed of sound in water, c, is about 1500 m/s. Thus, the typical Mach number is:

$$M = \frac{v}{c} = \frac{100}{1500} = 0.07 \ll 1 \tag{5.15}$$

The incompressible assumption is therefore valid throughout the implosion process, except for the brief instant of impact when fluid compression occurs. The effect of viscosity can be measured by calculating the Reynolds number, which is a measure of the ratio of inertial to viscous forces, for a typical flow during implosion. If the Reynolds number is $\gg 1$, the viscous forces are negligible and the flow may be considered inviscid. For a typical implosion flow:

$$Re = \frac{vL}{\nu} = \frac{100m/s * 1m}{10^{-6}m^2/s} = 10^8 \gg 1 \tag{5.16}$$

The inviscid assumption is therefore valid. Finally, the flow during implosion is irrota-

tional. The fluid starts in a state of rest, which is irrotational, and Kelvin's Theorem states that the flow will remain irrotational for all subsequent time. Thus, the potential flow assumptions are valid, except for the brief instant of impact. From fluid potential flow theory, the dynamic pressure at any instant is:

$$p_d = -\rho\left(\frac{\partial\phi}{\partial t} + \frac{1}{2} \mid \nabla\phi \mid^2\right) \tag{5.17}$$

where ρ is the fluid density and ϕ is the fluid potential. By definition, $\nabla\phi$ is equal to the fluid velocity. On the cylinder surface:

$$\nabla\phi = \dot{w} \tag{5.18}$$

Then at every time step:

$$p_{d,n} = -\rho\left(\frac{\partial\phi}{\partial t} + \frac{1}{2}\dot{w}_n^2\right) \tag{5.19}$$

$$p_n = p_{hyd} + p_{d,n} \tag{5.20}$$

$$\ddot{w}_n = \frac{p_n - p_{c,n}}{m} \tag{5.21}$$

With this complete set of equations, it is possible to calculate the surface position, velocity, acceleration, and fluid pressure acting on the surface at any time. As with the cylinder critical pressure, these parameters vary spatially over the cylinder surface. So the values calculated are really spatial averages over the entire cylinder surface. The calculations are straightforward, with the exception of the fluid potential ϕ. Therefore, as a first approximation, the contribution of $\frac{\partial\phi}{\partial t}$ to the dynamic pressure is neglected[2], and the dynamic pressure is calculated as:

$$p_{d,n} = -\frac{1}{2}\rho\dot{w}_n^2 \tag{5.22}$$

[2]This approximation is justified, at least for Phase 1, in Section 5.6.

Fluid Added Mass

Because the surrounding fluid moves with the cylinder walls during collapse, some energy is required to accelerate the fluid. This is accounted for by including the added mass of the fluid with the solid mass of the cylinder walls. Each infinitesimal piece of cylinder material is treated as a flat plate moving in a direction perpendicular to the plane of the plate, as shown in Fig. 5-5.

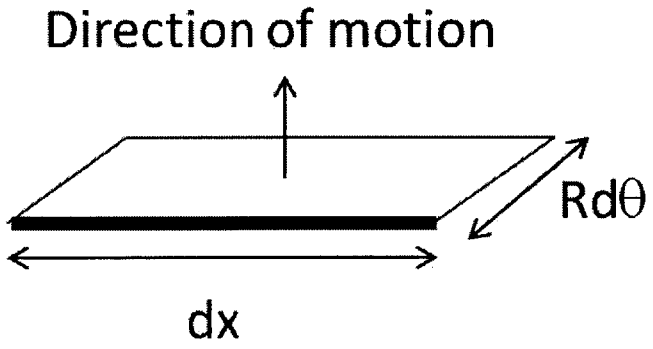

Figure 5-5: Infinitesimal section of cylinder wall approximated as a flat plate.

For such geometry, the added mass of the fluid per unit area (i.e., $dx = Rd\theta = 1$) is given by [35]:

$$m_a = \rho\frac{\pi}{4} \tag{5.23}$$

The mass per unit area for the cylinder material is simply the material density, ρ_s, times the wall thickness, h.

A simple MATLAB routine was written to evaluate Eqs. (5.13), (5.14), (5.20), (5.21), and (5.22) as functions of time t. The routine also calculates the critical pressure and cylinder volume from Eqs. (5.11) and (4.84) at each time interval. The user inputs to the routine are cylinder geometry (L, R, and h), cylinder material properties (σ_0 and ρ_s), fluid density (ρ), initial internal air pressure (p_{i_0}), and hydrostatic pressure (p_{hyd}). The calculations are done both with and without the fluid added mass. Figure 5-6 shows the critical pressure and fluid pressure acting on the cylinder surface vs. time for an example cylinder (the same cylinder represented in Fig. 4-18a).

L=137.3 mm	ρ_s=2700 kg/m^3
R=12.7 mm	ρ=1000 kg/m^3
h=0.889 mm	Ref: p_{i0}=0.1 MPa
σ_0=351 MPa	Ref: p_{hyd}=6.73 MPa

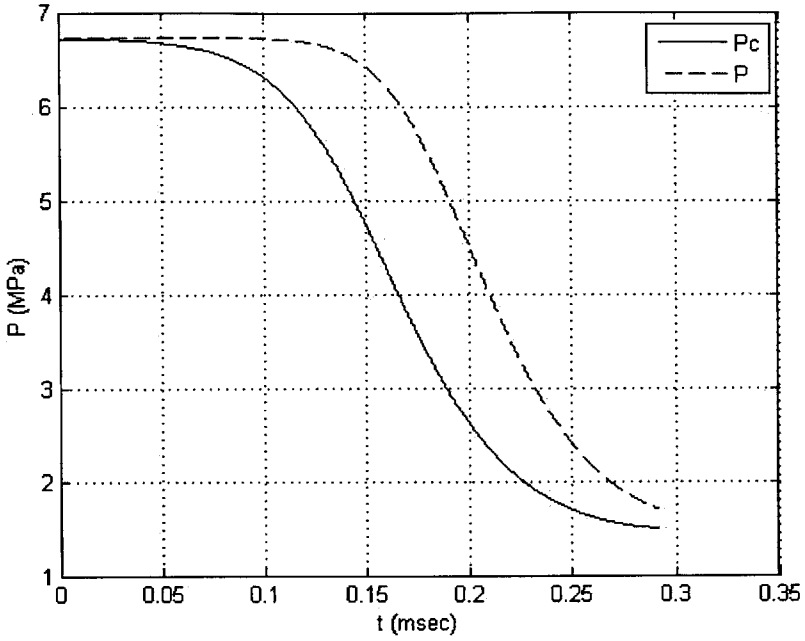

(a) Without added mass.

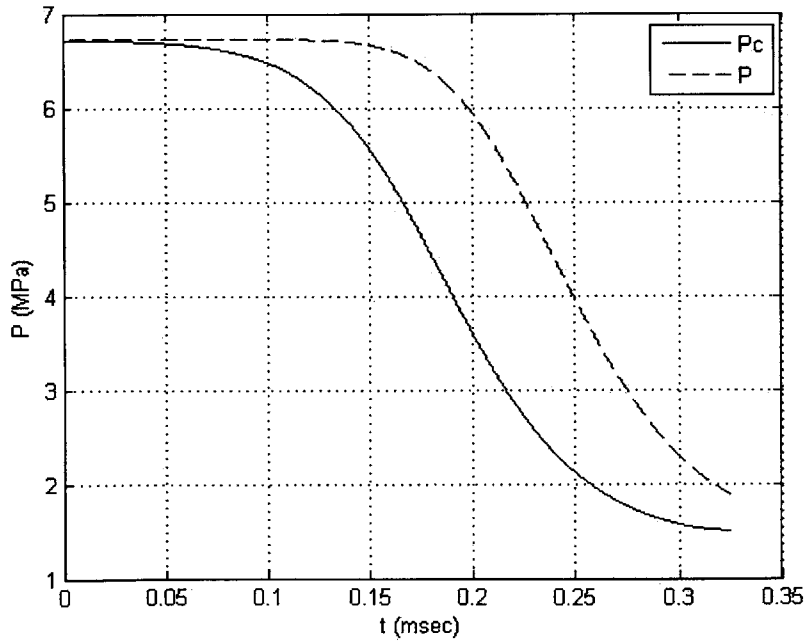

(b) With added mass.

Figure 5-6: Cylinder critical pressure and fluid pressure acting on surface vs. time (Phase 1).

A few observations can be made from Fig. 5-6:

1. Critical pressure is a function of displacement ($\frac{w_0}{R}$). Thus, at the end of Phase 1 the critical pressure is the same both with and without added mass.

2. The cylinder with fluid added mass collapses more slowly because of the increased inertia from the fluid.

3. The cylinder with fluid added mass experiences less of a dynamic pressure drop, corresponding to lower fluid velocity than the case without added mass.

Figure 5-7 shows the pressure behavior vs. displacement for both cases with and without added mass. As noted previously, the critical pressure vs. displacement is identical for the two cases.

Note that the plot starts at a finite value of $w > 0$. This is because the critical pressure goes to infinity as $w \to 0$. The minimum value of w on the plot represents the displacement when the critical pressure first drops below the hydrostatic pressure (i.e., $p_c < p_{hyd}$). The maximum value of w is the cylinder radius. The figure clearly shows that the inclusion of added mass causes less of a dynamic pressure drop for a given displacement.

In order to evaluate the accuracy of this explicit time-stepping methodology, an example is compared to a fully coupled FSI numerical simulation[3]. The numerical simulation had identical cylinder geometry, material properties, and initial pressures as the analytic solution. The numerical fluid pressure was recorded on the cylinder surface at the point where the leading generator intersects the center cross-section. The numerical pressure at this point and the spatially averaged analytic solution pressure are plotted vs. time in Fig. 5-8. Because the start time on the numerical simulation is arbitrary, the numerical plot is shifted horizontally to minimize the difference between the two curves.

[3]The numerical simulation was done by Dr. Ryan Chamberlin, Naval Undersea Warfare Center, Newport, RI.

L=137.3 mm	ρ_s=2700 kg/m^3
R=12.7 mm	ρ=1000 kg/m^3
h=0.889 mm	Ref: p_{i0}=0.1 MPa
σ_0=351 MPa	Ref: p_{hyd}=6.73 MPa

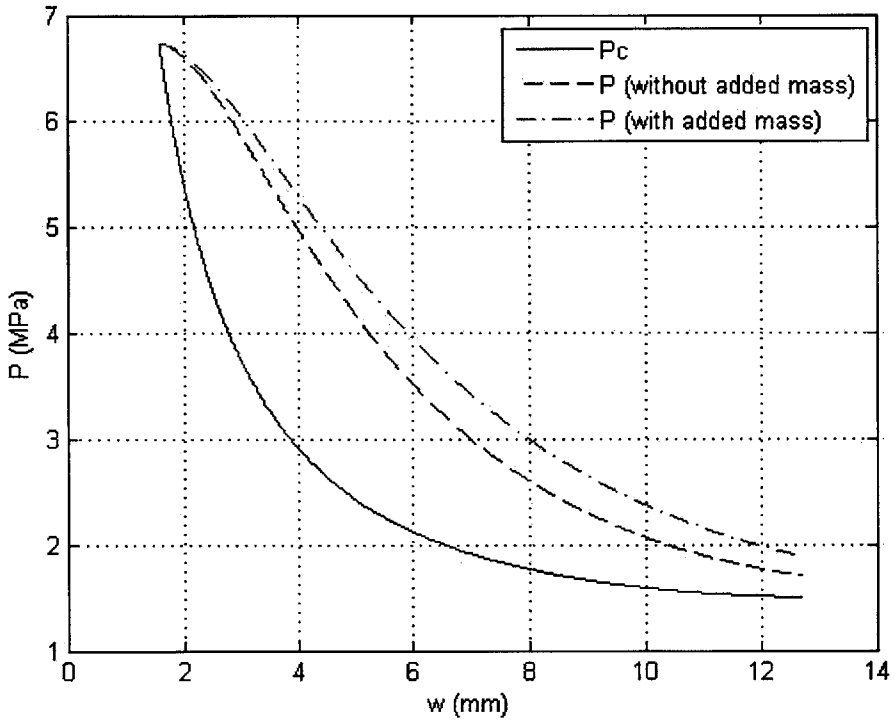

Figure 5-7: Cylinder critical pressure and fluid pressure acting on surface vs. displacement (Phase 1).

L=137.3 mm	ρ_s=2700 kg/m^3
R=12.7 mm	ρ=1000 kg/m^3
h=0.889 mm	Ref: p_{i0}=0.1 MPa
σ_0=351 MPa	Ref: p_{hyd}=6.73 MPa

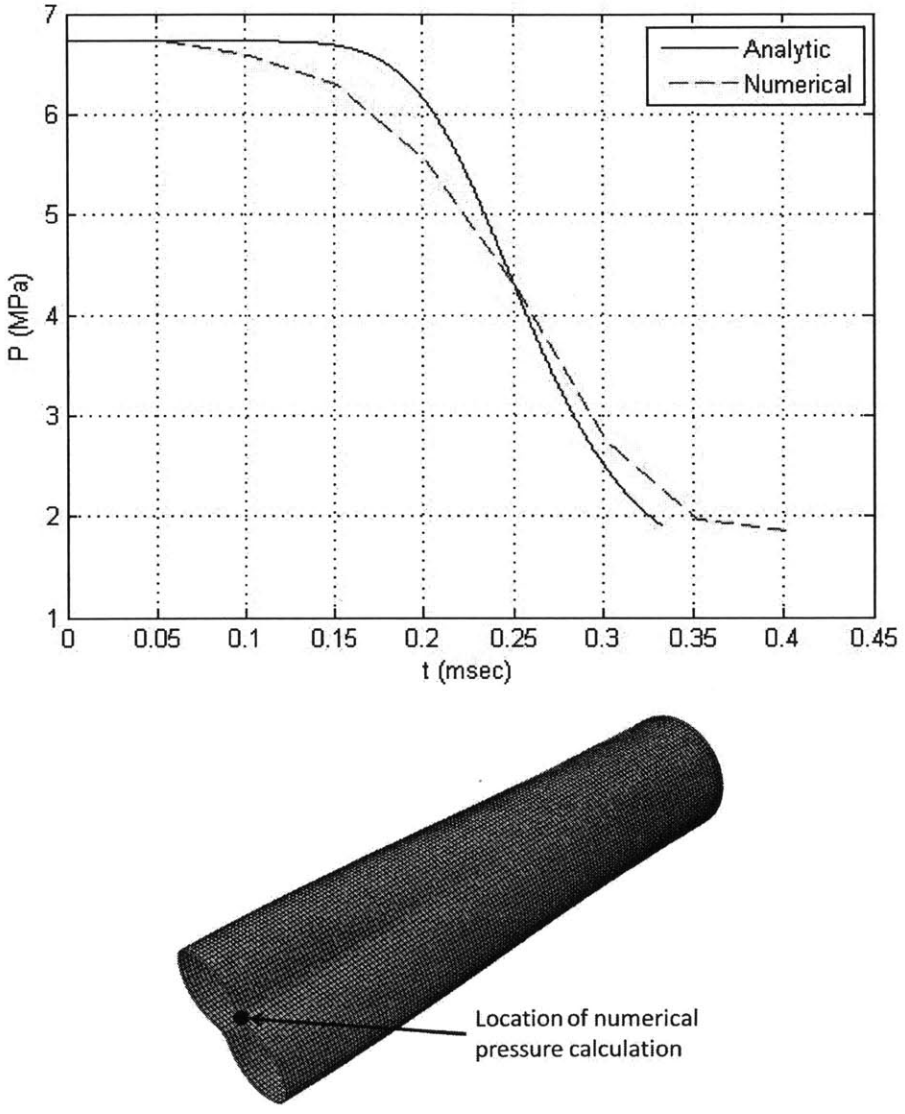

Figure 5-8: Comparison of analytic and numerical solutions for fluid pressure on the cylinder surface.

The following observations can be made from Fig. 5-8:

1. The final pressure values for the analytic and numerical solutions are nearly identical.

2. The analytic solution collapses more rapidly than the numerical simulation. This is likely due to the way in which added mass is approximated in the analytic solution, the spatial averaging inherent in the analytic solution, and the neglect of $\frac{\partial \phi}{\partial t}$ in the calculation of dynamic pressure.

5.4 Kinetic Energy Calculation

Given the analytic solution for fluid pressure, the work done on the cylinder by the fluid at any time may be calculated from Eq. (5.3). Substituting the expressions for E_{int} and E_{air} developed in chapters 4 and 2, respectively, the kinetic energy can then be directly calculated from Eq. (5.2).

Alternatively, the kinetic energy may be calculated by integrating the kinetic energy rate with respect to time:

$$KE = \int_0^t \dot{KE} dt \tag{5.24}$$

The instantaneous rate of change of kinetic energy is equal to the excess pressure times the instantaneous rate of volume change:

$$\dot{KE} = (p - p_c)\,\dot{V} \tag{5.25}$$

Both approaches give identical results for the kinetic energy.

The expressions for W, KE, E_{int} and E_{air} may be easily evaluated as functions of either time or displacement with a simple MATLAB routine. The complete energy

balance during Phase 1 for an example cylinder is plotted vs. displacement in Fig. 5-9.

L=137.3 mm	ρ_s=2700 kg/m^3
R=12.7 mm	ρ=1000 kg/m^3
h=0.889 mm	Ref: p_{i0}=0.1 MPa
σ_0=351 MPa	Ref: p_{hyd}=6.73 MPa

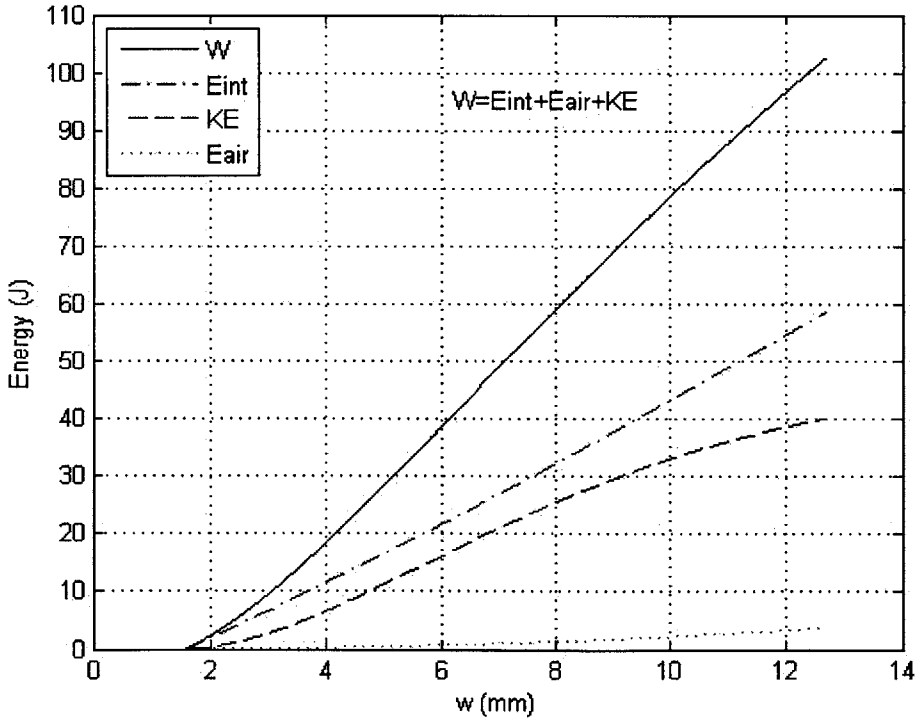

Figure 5-9: Complete energy balance during Phase 1.

For this example, the total work done during Phase 1 is 102.6 J. For comparison, if the external pressure is assumed constant (as it was in chapter 4), then the work done would be 214.7 J. Thus, the assumption of constant external pressure overestimates the work by more than 100% during Phase 1. The simplified FSI method provides a much more accurate estimate of work done on the cylinder by the fluid.

5.5 Validation of the Simplified FSI Methodology

An alternative method of calculating implosion pulse energy using measured fluid pressures was developed by Chamberlin, et al., at the Naval Undersea Warfare Center, Newport, RI [36]. The fluid pressure is recorded (either experimentally or via fully-coupled numerical simulation) at sample points in the fluid adjacent to the cylinder. The resulting pressure histories look similar to the representative implosion signature shown in Fig. 1-1. The intensity of an acoustic pressure wave is:

$$I = \frac{\langle p^2 \rangle}{\rho c} \tag{5.26}$$

where c is the speed of sound in the fluid. The units of intensity are $[\frac{energy}{time.area}]$. The energy flux $[\frac{energy}{area}]$ is then:

$$Flux = \int_{t1}^{t2} \frac{p^2}{\rho c} dt \tag{5.27}$$

where $t1$ and $t2$ are the start and end of the implosion event. Finally, the total energy is calculated by integrating the energy flux over a bounding surface area:

$$E = \int_S \int_{t1}^{t2} \frac{p^2}{\rho c} dt dS \tag{5.28}$$

Chamberlin demonstrated that the bounding surface may be approximated as a sphere with radius equal to the offset of the pressure measurement location. Furthermore, he showed that the energy calculated is largely insensitive to the pressure

measurement location. Thus, any one pressure location can be used to calculate the pulse energy by assuming the pressure is constant on the surface of the sphere with radius equal to the offset. Then the pulse energy is:

$$E = 4\pi R_{ref}^2 \int_{t1}^{t2} \frac{p^2}{\rho c} dt \tag{5.29}$$

where R_{ref} is the offset of the pressure measurement location. In order to validate the hypothesis that pulse energy is equal to the kinetic energy at the end of Phase 1, an example case is evaluated. The example case is identical to that of Fig. 5-9, but with a slightly higher hydrostatic pressure (6.94 MPa vs. 6.73 MPa). The pulse energy was calculated using a numerical simulation pressure history recorded at the cylinder end, 101.6 mm (8R) from centerline. The comparison is shown in Table 5.1.

Table 5.1: Pulse energy compared to Phase 1 kinetic energy.

L=137.3 mm
R=12.7 mm
h=0.889 mm
σ_0=351 MPa
p_{hyd}=6.94 MPa
Pulse Energy (from Eq. 5.29)=**43.95 J**
Phase 1 Kinetic Energy=**41.30 J**
% Difference=**6.0%**

The comparison indicates very close agreement between the two energy values.

5.6 Summary, Limitations and Conclusions

The simplified FSI methodology provides an accurate estimate of implosion pulse energy, given the cylinder geometry (L, R, and h), cylinder material properties (σ_0 and ρ_s), fluid density (ρ), initial internal air pressure (p_{i_0}), and hydrostatic pressure (p_{hyd}). The method gives results comparable (within $< 10\%$) to experiments or numerical

simulations, at a much lower cost (as measured by computational or experimental effort). As expected, the simplified FSI method underestimates the pulse energy, because the kinetic energy at the end of Phase 1 is slightly less than the maximum during the whole implosion event (see Fig. 5-1).

The simplified FSI methodology only calculates the implosion pulse energy. It does not predict the pulse peak pressure or total impulse delivered by the implosion pulse. These quantities require knowledge of the complete pressure history of the implosion event, which cannot be analytically predicted.

The dynamic fluid pressure was calculated using Eq. 5.22, neglecting the effect of the time derivative of the fluid potential, $\frac{\partial \phi}{\partial t}$. During Phase 1, this is a reasonable approximation. During Phase 1, the changes in fluid velocity and pressure occur relatively slowly (compared to Phases 2 and 3). It is therefore expected that the contribution to dynamic pressure of the term $\frac{\partial \phi}{\partial t}$ will be much smaller than the term $\frac{1}{2}\dot{w}^2$, and the first term may be neglected. This is no longer the case once the first contact occurs between cylinder walls (i.e., after Phase 1). When contact occurs, the structural motion abruptly stops and the fluid rapidly decelerates and compresses. This compression of the fluid causes a high pressure wave which propagates away from the cylinder (i.e., the implosion pulse). The changes in fluid velocity and pressure during this period are extremely rapid, and the term $\frac{\partial \phi}{\partial t}$ cannot be neglected. In fact, the presence of fluid compression at the instant of impact violates the assumptions of potential flow theory. Thus, it is critical that the simplified FSI methodology involve only Phase 1 to estimate the implosion pulse energy.

The simplified FSI methodology applies specifically to metallic cylinders that collapse via mode 2, without material fracture. However, the method may be applied to cylinders that fail via higher modes to provide an upper bound on pulse energy. A given cylinder will dissipate the minimum amount of plastic energy deforming into mode 2 compared to higher modes, primarily because the higher modes require more

bending of the material. From Eq. 5.2, the minimum value of E_{int} corresponds to the maximum value of KE, which is equivalent to the pulse energy. So the simplified FSI methodology should provide an upper bound on pulse energy for a given cylinder geometry and pressure, regardless of the actual collapse mode. Note that this conclusion has not yet been tested or validated, and is left as future work.

Chapter 6

Design Recommendations for Implodable Structures

The principal goal of studying underwater implosion is to minimize the effect of the implosion on adjacent structures. The effect of implosion can be minimized in two ways:

1. Prevent implosion from occurring, by designing the implodable with a very high safety factor for the worst-case operating conditions, or

2. Allow that implosion may occur under certain conditions, and design the implodable to minimize the implosion pulse energy or peak pressure when it occurs.

The first method is extremely conservative and results in heavy, expensive implodables. The second method can be implemented by using the knowledge and tools developed in the previous chapters to guide the design of implodable structures, with the goal being to minimize the energy released in the implosion pulse.

In Chapter 5, it was shown that for a simple mode 2 collapse the kinetic energy at the end of Phase 1 is very nearly equal to the implosion pulse energy. The kinetic

energy at the end of Phase 1 is given by Eq. (5.2), repeated here:

$$KE = W - E_{int} - E_{air} \tag{6.1}$$

The external work W is a function of the fluid pressure acting on the cylinder and the change in volume. It is assumed that the implodable specifications require a certain internal volume of gas (otherwise, it would not be considered an implodable volume). Then the external work done during collapse cannot be changed by design[1]. However, the plastic energy dissipation (E_{int}) and energy required for compression of the internal gas (E_{air}) can be changed by design choices. It is clear from Eq. (6.1) that the kinetic energy (and subsequently the implosion pulse energy) can be reduced by increasing either E_{int} or E_{air}. The following sections suggest specific implodable design practices that will increase E_{int} or E_{air} and subsequently decrease the implosion pulse energy.

6.1 Methods to Increase E_{int}

The process of plastic energy dissipation during implosion was discussed in detail in Chapter 4. One way in which the energy dissipation can be increased for a given cylinder (i.e., without changing material or dimensions) is by triggering a higher collapse mode. In general, higher collapse modes will dissipate more energy, mainly because of the increased circumferential bending required. To verify this, the ABAQUS numerical simulation of Chapter 3 was utilized. An example cylinder (with perfect geometry) that naturally collapsed in mode 2 was simulated, and the total plastic energy dissipation was recorded. Then a static buckling analysis was performed on the perfect structure to determine the buckling modes. For this particular example

[1]The analysis of different collapse modes in the next section shows that the external work is nearly independent of collapse mode. External work values are constant within 4%.

cylinder, the first five buckling mode shapes are shown in Fig. 6-1.

(a) Mode 2.

(b) Mode 2A.

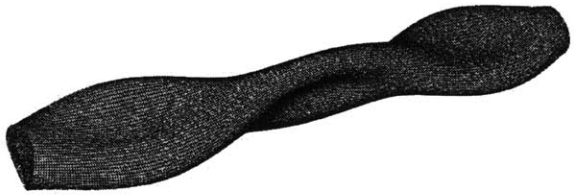

(c) Mode 2B.

(d) Mode 3.

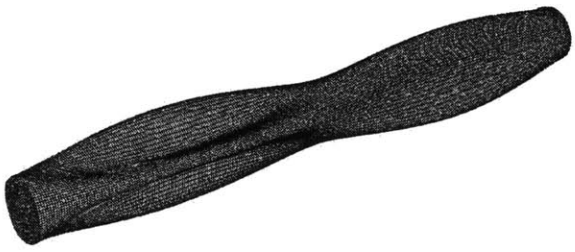

(e) Mode 3A.

Figure 6-1: First five buckling modes for example cylinder.

Modes 2A and 2B have the same 2-lobe cross-sectional shape as mode 2, but the cylinder length is subdivided into 2 or 3 segments rotated 90 degrees relative to each other. Similarly, mode 3A is identical to mode 3 but with the length subdivided into 2 segments. These intermediate modes exist for this cylinder because the length-to-diameter ratio is relatively large ($\frac{L}{R} = 10.8$).

The same cylinder was then subjected to initial geometric imperfections to trigger collapse in higher modes. The geometric imperfections were introduced as individual mode shapes, with maximum magnitude $\Delta = 1$ mm (R=12.7 mm, so $\frac{\Delta}{R} = 0.08$). Dynamic simulations were run with imperfections in each of the first four modes, and resulting energy dissipation and external work are plotted in Fig. 6-2.

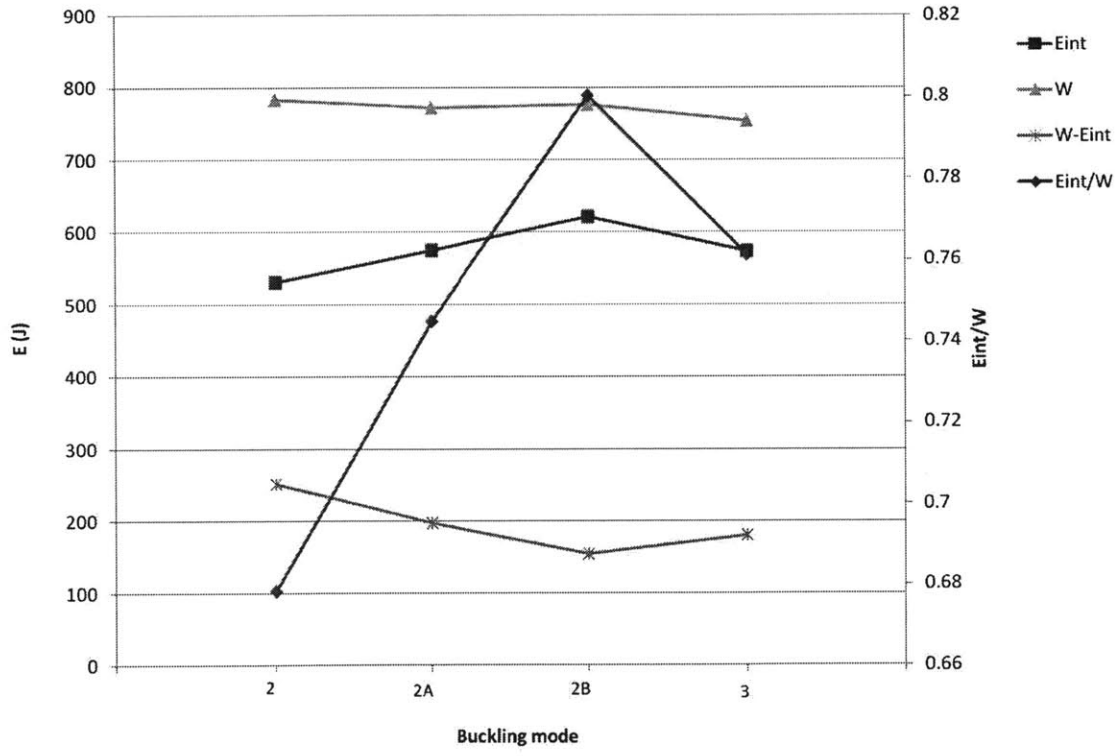

Figure 6-2: Effect of collapse mode on plastic energy dissipation and external work ($\frac{\Delta}{R} = 0.08$).

The external work, W, is nearly independent of collapse mode (within 4%), but the plastic energy dissipation, E_{int}, varies. The energy of the implosion pulse can be roughly approximated as $W - E_{int}$. The ratio $\frac{E_{int}}{W}$ provides another measure of implosion pulse energy (higher $\frac{E_{int}}{W}$ corresponds to lower pulse energy). In this example, mode 2B clearly has the minimum $W - E_{int}$ and maximum $\frac{E_{int}}{W}$, which indicates the minimum implosion pulse energy for this cylinder.

Next, the effect of the imperfection magnitude was investigated for the mode of minimum pulse energy (mode 2B in this case). Seven different values of $\frac{\Delta}{R}$ were evaluated, from 0 (perfect geometry) to 0.08, and results are plotted in Fig. 6-3.

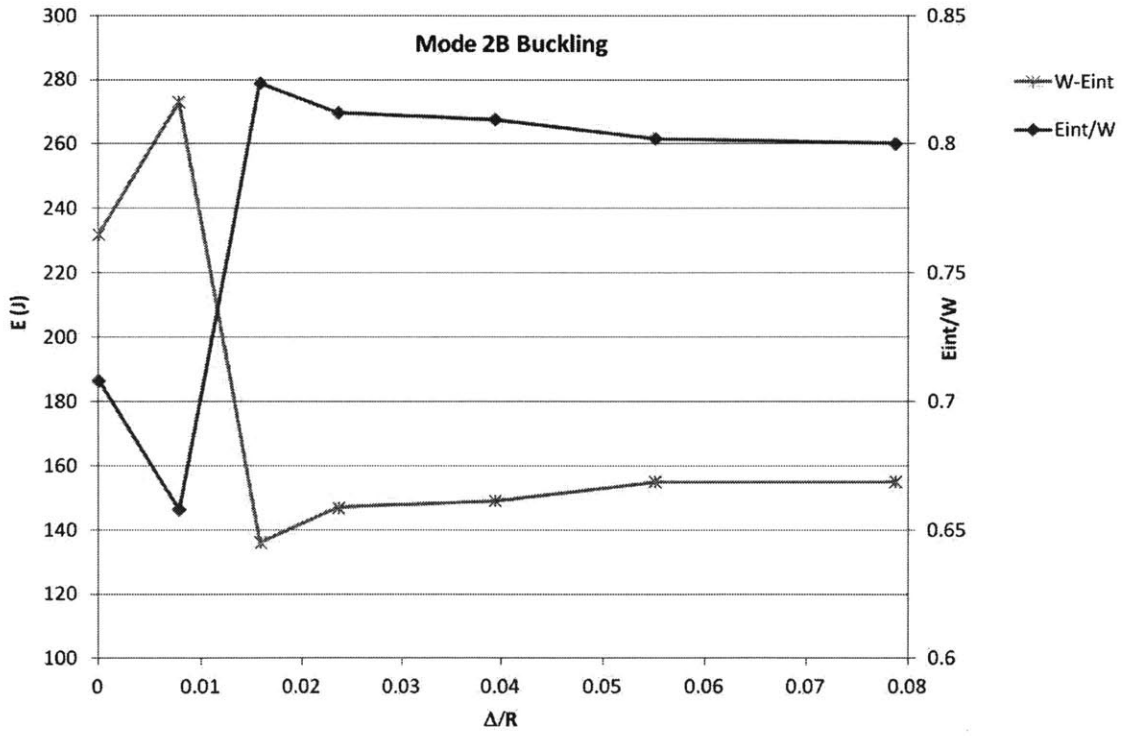

Figure 6-3: Effect of imperfection magnitude on plastic energy dissipation and external work.

The case with $\frac{\Delta}{R} = 0.008$ actually generates a larger implosion pulse than the case with no imperfection. This is because the imperfection is not large enough to trigger the desired collapse mode 2B. Thus, the cylinder still collapses in the natural mode 2, but the imperfection serves to lower the plastic energy dissipation. The result is a larger implosion pulse. The minimum implosion pulse is seen at about $\frac{\Delta}{R} = 0.015$. The pulse energy is essentially constant above that magnitude of imperfection. For this example, the difference between the minimum pulse and the baseline with no imperfection is 96 J, or 41% of the baseline value.

Of course, intentionally causing geometric imperfections in the cylinder reduces the overall strength and resistance to buckling compared to the perfect geometry. In order to minimize the strength reduction, it is desirable to use the minimum imperfection magnitude necessary to achieve the desired mode shape. Figure 6-3 shows that there is a clear minimum value of $\frac{\Delta}{R}$ that forces the desired mode shape and also yields the smallest implosion pulse (in this case, $\frac{\Delta}{R} = 0.015$). For this example, applying the mode 2B imperfection with magnitude $\frac{\Delta}{R} = 0.015$ reduces the collapse pressure from 6.37 MPa to 6.34 MPa, a decrease of only 0.5%.

It may be difficult to manufacture precise mode shape imperfections into a real implodable. A less elegant alternative way to introduce imperfections is to create local weak spots in the structure in such a way as to trigger the desired collapse mode. For example, to trigger mode 3 collapse, the wall thickness of the center cross-section could be thinned slightly at three points spaced 120 degrees apart. This could be done quite simply by grinding flat spots onto the outer cylinder surface, as shown in Fig. 6-4. The flat spots in this figure are greatly exaggerated to be more visible.

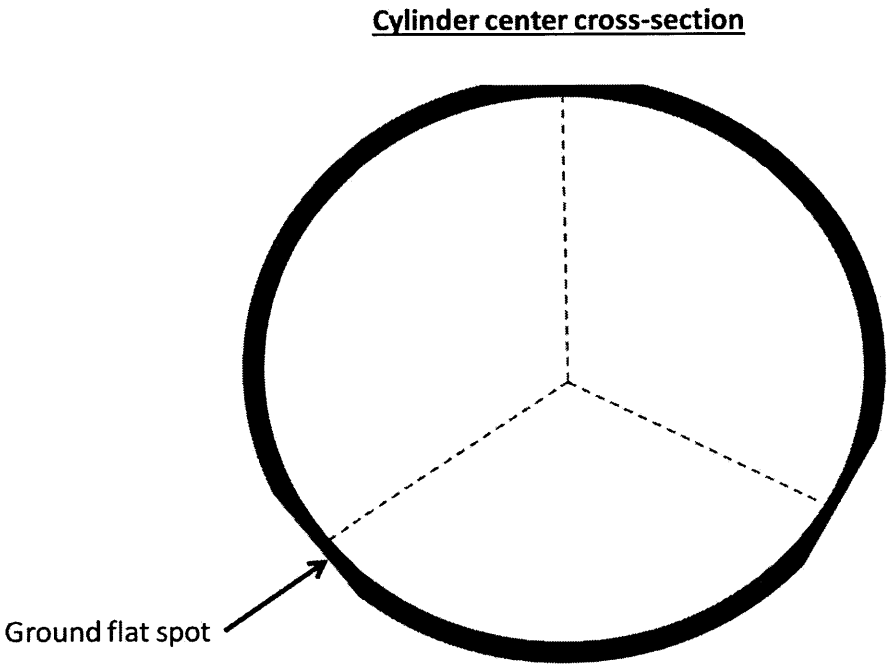

Figure 6-4: Intentional imperfections to trigger mode 3 collapse.

This method will have a greater detrimental effect on the overall collapse strength of the structure than the precise mode shape imperfection method described earlier. Therefore, the effect of the imperfections on the overall structural design must be carefully considered.

Alternatively, a thin layer of energy absorbing material (such as a honeycomb structure) could be added to the inner surface of the cylinder. The energy absorbed by this layer would add to the plastic energy dissipation of the main cylinder structure and reduce the kinetic energy (and therefore the implosion pulse energy) according to Eq. (6.1).

6.2 Methods to Increase E_{air}

The energy required for adiabatic compression of the air was given by Eq. (2.32), repeated here:

$$E_{air,adiabatic} = \frac{p_{i_0} V_0}{\gamma - 1} \left[\left(\frac{V_0}{V} \right)^{\gamma - 1} - 1 \right] \tag{6.2}$$

The energy required is directly related to the initial internal air pressure, p_{i_0}. Thus, if the implodable interior is initially pressurized above atmospheric pressure, then the energy required to cause the same volume change (i.e., complete collapse of the cylinder) will be greater. The effect of increasing internal pressure was evaluated quantitatively using the tools and methodology developed in previous chapters.

Constant Cylinder Geometry

First, the internal pressure was varied while holding the cylinder geometry constant. As the internal pressure of a given cylinder is increased, the initial collapse pressure increases by an equal amount, because buckling and collapse are caused by the differential pressure felt across the cylinder wall. Therefore, for this analysis the external

hydrostatic pressure, p_{hyd}, is varied from the reference value by the same amount as the initial internal pressure, p_{i_0}. The reference condition is an initial internal pressure of 1 atmosphere (0.1 MPa), yielding an implosion pulse energy E_0. The simplified FSI methodology of Chapter 5 was used to calculate the pulse energy over a range of internal pressures for two example cylinders (the same two cylinders previously analyzed in Chapters 4 and 5). The non-dimensional pulse energy ($\frac{E}{E_0}$) is plotted vs. the non-dimensional pressure ($\frac{p_{i_0}}{p_{hyd}}$) in Fig. 6-5. The plot indicates that (as expected) the pulse energy decreases as initial internal pressure increases. There exists a value for p_{i_0} above which the cylinder will not fully implode and the implosion pulse does not occur.

Cylinder A		Cylinder B	
L=137.3 mm	ρ_s=2700 kg/m^3	L=183.4 mm	ρ_s=2700 kg/m^3
R=12.7 mm	ρ=1000 kg/m^3	R=19.07 mm	ρ=1000 kg/m^3
h=0.889 mm	Ref: p_{i0}=0.1 MPa	h=0.714 mm	Ref: p_{i0}=0.1 MPa
σ_0=351 MPa	Ref: p_{hyd}=6.73 MPa	σ_0=351 MPa	Ref: p_{hyd}=1.1 MPa

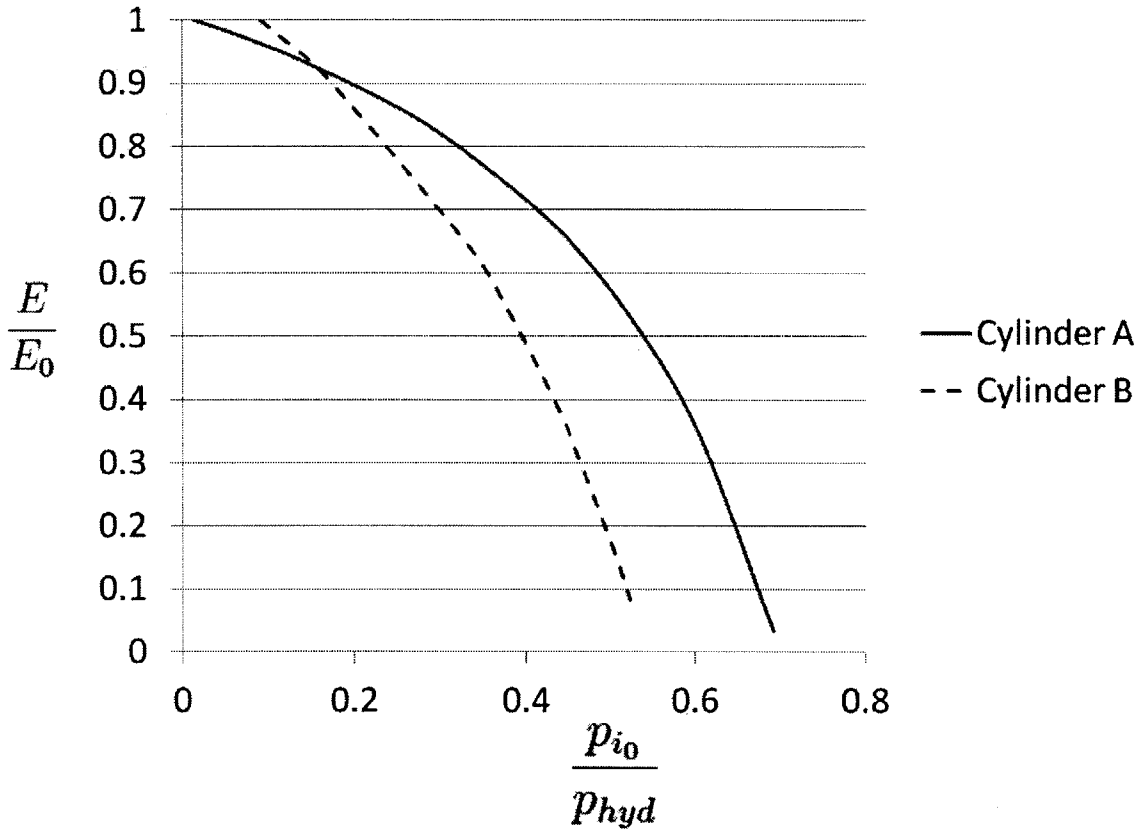

Figure 6-5: Effect of varying internal pressure on implosion pulse energy (constant cylinder geometry).

Constant Hydrostatic Pressure

Second, the internal pressure was varied along with the cylinder wall thickness, h, to maintain a constant initial collapse pressure (or hydrostatic pressure). This is the more realistic approach because in most real applications, an implodable will be designed for a specified operating depth. As the internal pressure is increased, the wall thickness may be correspondingly decreased to maintain the same collapse pressure. The ABAQUS numerical model, described in Chapter 3, was used to evaluate the buckling pressure of the two example cylinders over a range of wall thicknesses. The buckling pressure was subtracted from the constant hydrostatic pressure to give the required internal pressure for each thickness. The reference condition is the original wall thickness (h_0) with an internal pressure of 1 atmosphere (0.1 MPa). The non-dimensional pressure ($\frac{p_{i0}}{p_{hyd}}$) is plotted vs. the non-dimensional thickness ($\frac{h}{h_0}$) in Fig. 6-6. The two example cylinders show a nearly identical inverse relationship.

Cylinder A		Cylinder B	
L=137.3 mm	ρ_s=2700 kg/m^3	L=183.4 mm	ρ_s=2700 kg/m^3
R=12.7 mm	ρ=1000 kg/m^3	R=19.07 mm	ρ=1000 kg/m^3
h=0.889 mm	Ref: p_{i0}=0.1 MPa	h=0.714 mm	Ref: p_{i0}=0.1 MPa
σ_0=351 MPa	Ref: p_{hyd}=6.73 MPa	σ_0=351 MPa	Ref: p_{hyd}=1.1 MPa

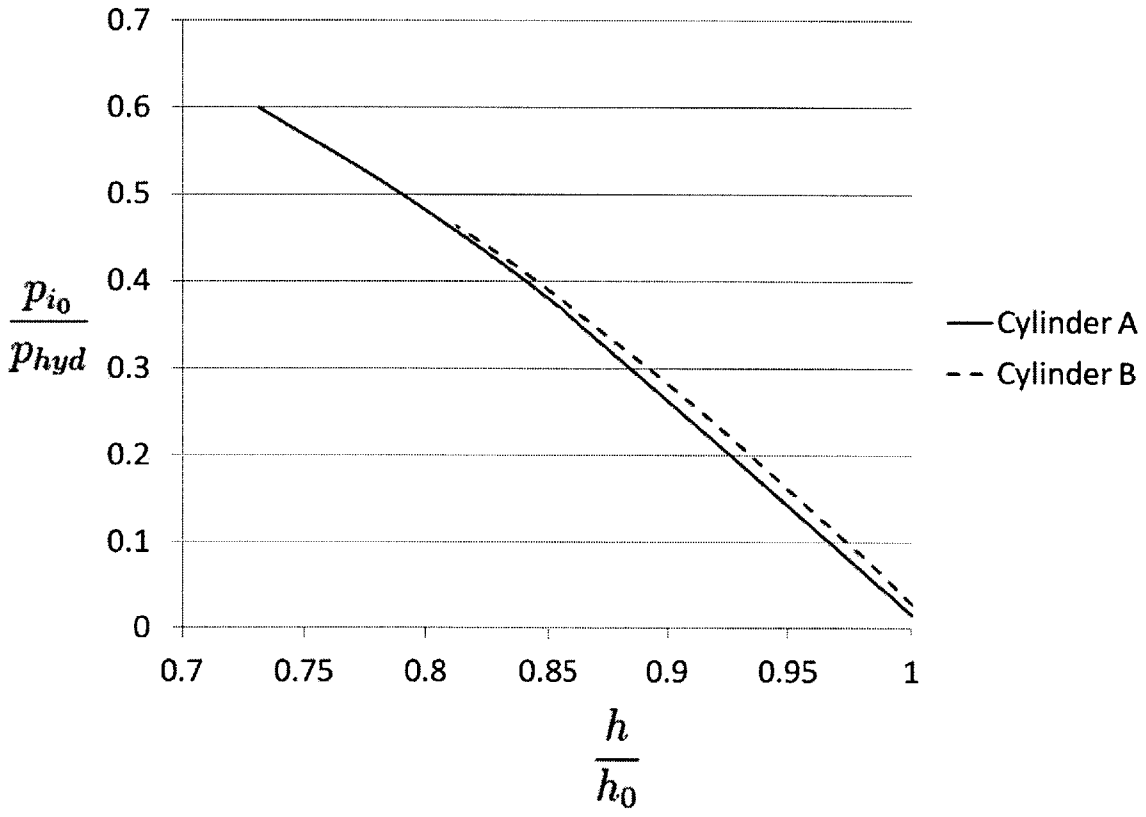

Figure 6-6: Internal pressure vs. cylinder wall thickness (constant hydrostatic pressure).

The simplified FSI method of Chapter 5 was then used to calculate the pulse energy over a range of wall thicknesses and corresponding internal pressures for the two example cylinders. The non-dimensional pulse energy ($\frac{E}{E_0}$) is plotted vs. the non-dimensional pressure ($\frac{p_{i_0}}{p_{hyd}}$) and non-dimensional thickness ($\frac{h}{h_0}$) in Fig. 6-7. The plots indicate that the pulse energy decreases as initial internal pressure increases and wall thickness decreases. There exists a value for p_{i_0} above which the cylinder will not fully implode and the implosion pulse does not occur.

Cylinder A		Cylinder B	
L=137.3 mm	ρ_s=2700 kg/m^3	L=183.4 mm	ρ_s=2700 kg/m^3
R=12.7 mm	ρ=1000 kg/m^3	R=19.07 mm	ρ=1000 kg/m^3
h=0.889 mm	Ref: p_{i0}=0.1 MPa	h=0.714 mm	Ref: p_{i0}=0.1 MPa
σ_0=351 MPa	Ref: p_{hyd}=6.73 MPa	σ_0=351 MPa	Ref: p_{hyd}=1.1 MPa

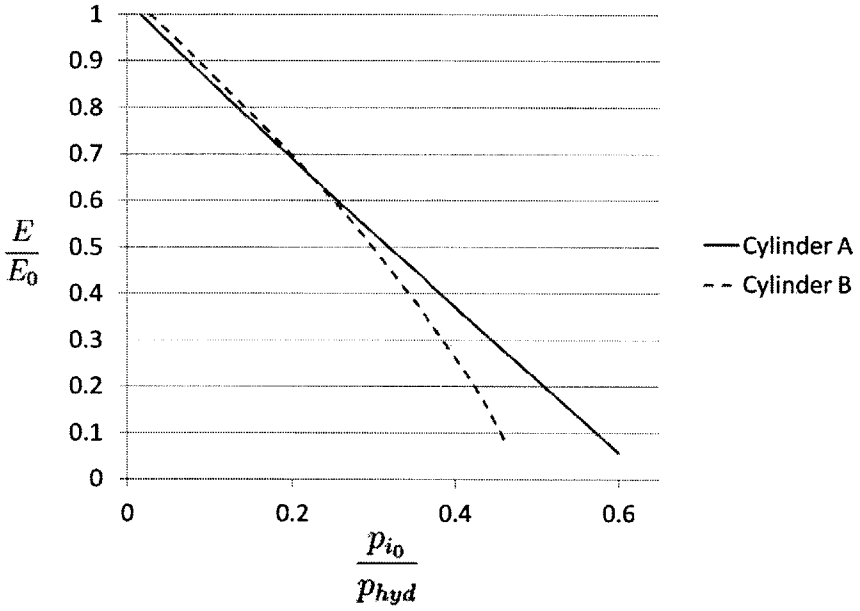

(a) Energy vs. internal pressure.

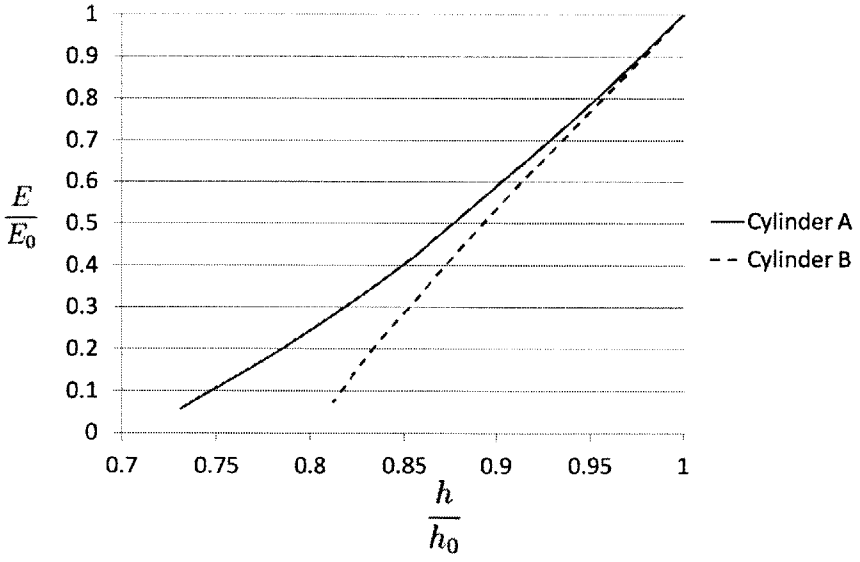

(b) Energy vs. thickness.

Figure 6-7: Effect of varying internal pressure and thickness on implosion pulse energy (constant hydrostatic pressure).

Limitations on Internal Pressure

The previous analysis shows that increasing the initial internal pressure, accompanied by either a corresponding increase in collapse pressure or a corresponding decrease in wall thickness, lowers the implosion pulse energy. If the internal pressure is high enough, complete implosion can be prevented. However, there are practical limits to the internal pressure. First, the contents of the implodable (electronics, sensors, propulsion systems, etc.) must be able to survive and operate in the pressurized atmosphere. If the implodable is to be manned, then the human response to pressure, and the necessary subsequent decompression, must be considered. Second, internal pressure causes structural stresses opposite in sign from the stress caused by external pressure. In some cases, the stress from internal pressure could be design-limiting.

An alternative way to increase E_{air} is by changing the composition of the gas, which changes the ratio of specific heats (γ). From Eq. (6.2), it follows that a higher value of γ gives a higher value of E_{air}, for the same volume ratio. The noble gases helium, neon, argon, krypton, xenon, and radon all have $\gamma = 1.67$, compared to air with $\gamma = 1.4$. For all the example cylinders analyzed in this work, the volume ratio at the end of Phase 1 was approximately $\frac{V_0}{V} = 1.3$. For this volume ratio, increasing γ from 1.4 to 1.67 increases E_{air} by 3.7%. Therefore, using a noble gas instead of air as the internal medium would cause a slight increase in E_{air} and a corresponding decrease in implosion pulse energy.

In summary, the maximum reduction in pulse energy will be realized when a noble gas medium is used in combination with the highest possible internal pressure, limited by the considerations discussed above.

6.3 Use of Flexible Material Inside Cylinder

The final design recommendation of this thesis is discussed qualitatively only; no quantitative analysis has been done to date. The recommendation seeks to reduce the peak pressure reached during the implosion, rather than reduce the implosion pulse energy.

A representative fluid pressure history from an implosion event is shown in Fig. 6-8.

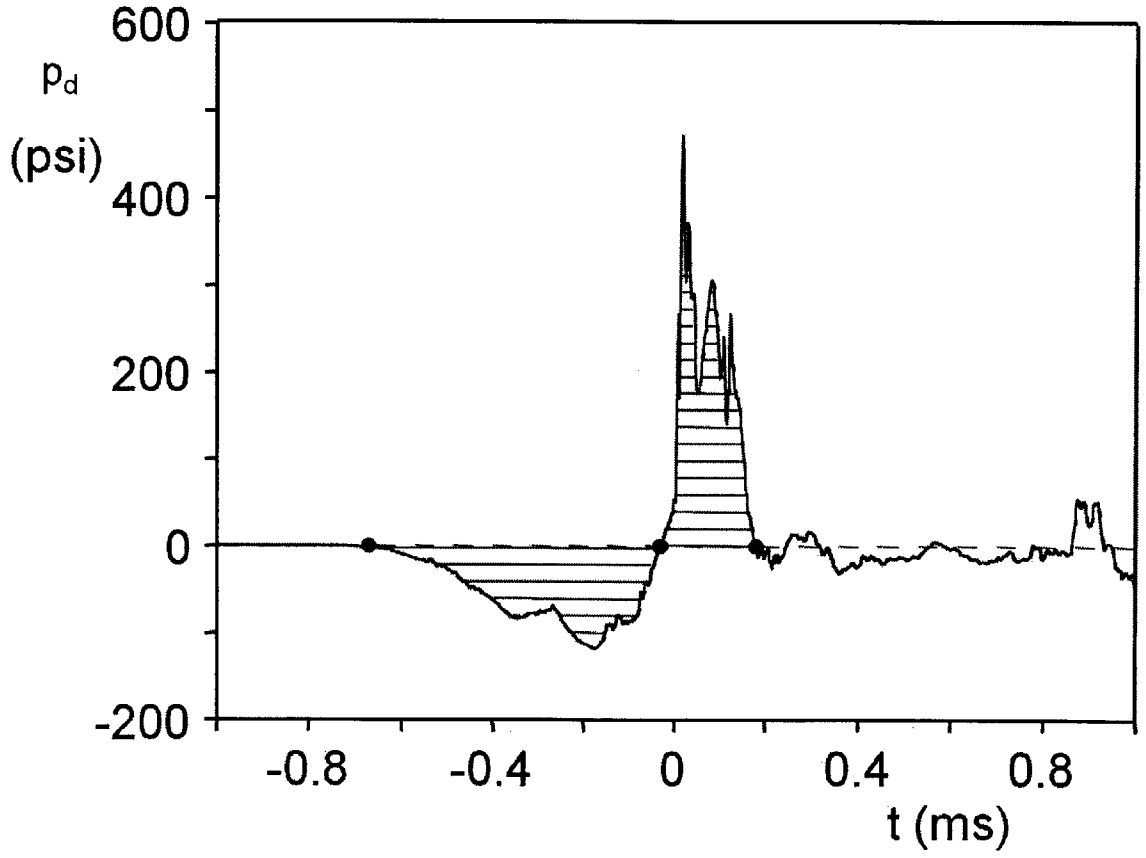

Figure 6-8: Typical dynamic pressure history for an underwater implosion event.

The large pressure spike is caused by compression of the fluid when the in-rushing motion abruptly stops. The magnitude of the pressure spike is closely related to the deceleration of the solid surface and accompanying fluid. The fluid dynamic pressure (assuming potential flow conditions) is given by Eq. (5.17), repeated here:

$$p_d = -\rho\left(\frac{\partial\phi}{\partial t} + \frac{1}{2} \mid \nabla\phi \mid^2\right) \tag{6.3}$$

As noted before, the potential flow assumptions are not strictly valid at the instant of impact, because of fluid compressibility. However, Eq. (6.3) still gives an estimate of dynamic pressure if compressibility is neglected. During Phase 1 collapse, the second term on the right-hand side of Eq. (6.3) is much larger than the first term, resulting in the large negative dynamic pressure just before impact. At the instant of impact, $\frac{\partial\phi}{\partial t}$ acquires a large negative value while $\mid \nabla\phi \mid^2$ drops significantly. The result is that the first term dominates the second, giving a large positive value of dynamic pressure. Thus, the magnitude of the pressure spike can be reduced by reducing the magnitude of $\frac{\partial\phi}{\partial t}$ at the instant of impact, which in turn is reduced by slowing the deceleration of the solid surface and accompanying fluid.

One way to reduce the surface deceleration is to add a layer of flexible material, such as rubber or polyurea, to the inside of the metallic cylinder. This layer serves to cushion the impact between opposite cylinder walls by converting some system kinetic energy into elastic stored energy. The stored elastic energy may be permanently stored if the structure remains fully crushed, or it may be released if there is a slight rebound. In either case, the finite (albeit small) duration of the elastic process serves to lengthen the overall duration of the energy conversion process, which effectively reduces the deceleration of the surface. The total energy transmitted in the implosion pulse is the same as if the flexible layer were not present; however, the pulse power (energy/time) is lower because the pulse duration is longer.

The flexible lining material could be applied uniformly to the inner surface of the cylinder to provide cushioning at every point of contact. However, analysis shows that the peak pressure occurs very close to the end of Phase 1. Therefore, only the region of the cylinder which experiences the first contact must be cushioned to achieve the bulk of the benefit. If the specific collapse mode is known, then the flexible lining can be optimized by only applying in the areas of first contact. Figure 6-9 shows an example of a uniformly applied lining, as well as a lining optimized for mode 2 collapse.

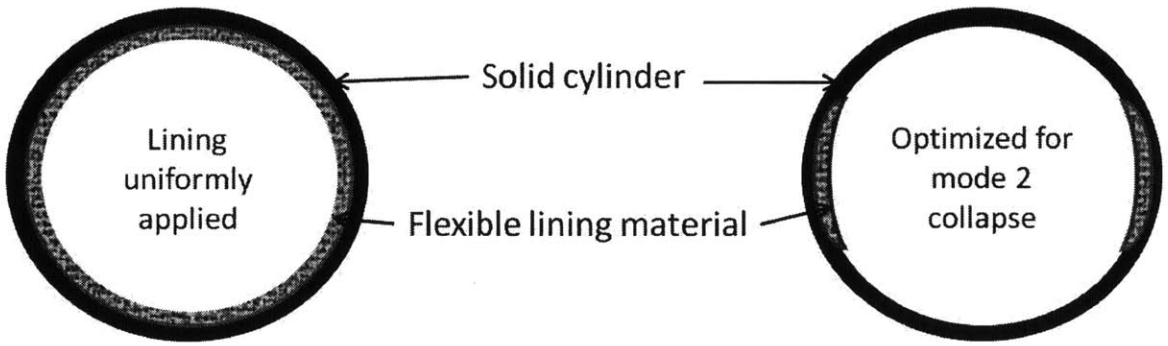

Figure 6-9: Flexible cylinder lining to reduce implosion severity.

The semi-analytic tools and methods developed in this work are not able to quantitatively evaluate this design recommendation. A fully-coupled numerical simulation is required to fully evaluate its effectiveness in reducing the peak pressure of the implosion pulse. The details of lining optimization are left as future work.

Chapter 7

Conclusions and Future Work

This chapter summarizes the results and conclusions of the present research and provides recommendations for future work.

7.1 Conclusions

The underwater implosion problem was analyzed using an energy balance approach, with the principle of virtual velocities as a foundation. The primary goal of the research was to develop tools and methods to accurately estimate the severity of an implosion pulse (quantified by the pulse energy), given a cylinder geometry, material properties, and external hydrostatic pressure. A secondary goal was to apply the knowledge gained through the research to make design recommendations to minimize the implosion severity.

Assumptions

A number of assumptions and simplifications, summarized in the following list, were required to make the problem tractable. The assumptions are described in detail in Chapter 2.

1. The material was modeled as rigid-perfectly plastic, with flow stress σ_0.

2. The bending and membrane effects were separated by assuming a rectangular, limited interaction yield condition.

3. Shear energy dissipation is neglected.

4. The 3D kinematics of implosion are simplified into single degree of freedom models for all three collapse phases. The circumferential shape is described by the stationary hinge model in Phase 1, and by a new moving hinge model in Phases 2 and 3. The longitudinal shape is assumed to be triangular or linear in all phases.

5. The internal air compression is treated as adiabatic and uniform throughout the cylinder.

6. Only symmetric mode 2 collapse, without fracture, is considered.

ABAQUS Numerical Simulations

A numerical model of a hydrostatically-loaded cylinder was developed. The model did not include fluid effects. The model was used to investigate the kinematics of cylinder collapse and to guide the assumptions used in the analytic energy derivations. The simulations also calculated plastic energy dissipation, for comparison to the analytic solutions.

Plastic Energy Dissipation

Expressions for the plastic energy dissipation (bending and membrane) for all three phases were developed. In all cases, the energy expression was a function of a single time-like parameter, though the parameters were different for each phase. The Phase 2 and 3 results were semi-analytic, because they required estimates of non-dimensional

parameters extracted from numerical simulations ($\bar{b_{0_f}}$, $\bar{\zeta_{2_f}}$, and $\bar{\zeta_{3_f}}$). The derived energy expressions match numerical simulations within 10%. The error is significantly less for thicker-walled cylinders (i.e., cylinders with lower R/h). In all cases analyzed, the plastic energy dissipation constituted at least 70% of the total external work done on the cylinder.

Simplified FSI Methodology

A simplified fluid-structure interaction methodology was developed to evaluate the effects of the surrounding fluid and calculate the implosion pulse energy. The methodology uses an explicit time-stepping approach, with the assumption of constant pressure and corresponding acceleration over very small time intervals. The simplified FSI methodology provides an accurate estimate of implosion pulse energy, given the cylinder geometry (L, R, and h), cylinder material properties (σ_0 and ρ_s), fluid density (ρ), initial internal air pressure (p_{i_0}), and hydrostatic pressure (p_{hyd}). The results for a specific example cylinder are within 6% of fully-coupled numerical simulation results.

Implodable Design Recommendations

Three general implodable design recommendations, summarized in the following list, were made based on the results of the energy derivations and simplified FSI methodology. The intent of the first two recommendations is to reduce the implosion pulse energy. The intent of the final recommendation is to reduce the magnitude of the implosion pressure spike.

1. Increase the plastic energy dissipation for a given cylinder geometry and hydrostatic pressure. This can be done by designing the implodable so that it preferentially collapses into higher modes that dissipate more energy, or by

adding a layer of energy-absorbing material to the inner cylinder surface.

2. Increase the energy absorbed by the internal air. This can be done through a combination of increasing initial pressure and/or utilizing a gas with a higher ratio of specific heats (γ) than air.

3. Reduce the deceleration of the cylinder at the instant of impact between opposite cylinder walls. This can be done through the use of a flexible cushioning material on the inner cylinder surface.

The effectiveness of these design improvements will vary with each specific implodable's unique set of design specifications and constraints. However, these recommendations can be applied, in some degree, to all implodables to reduce the effect of implosion on an adjacent structure.

7.2 Future Work

Three areas of future work directly related to this research were identified.

Analytic (or Semi-Analytic) Solutions for Higher Modes

As shown in Chapter 6, the collapse mode affects the plastic energy dissipation, which is inversely related to the energy transmitted in the implosion pulse. The analytic energy solutions and the simplified FSI methodology developed in this work apply specifically to symmetric mode 2 cylinder collapse.

The entire analysis process described in Chapters 2, 4, and 5 could be repeated for other symmetric collapse modes. First, a viable set of kinematic assumptions and models must be developed that accurately represents the higher mode collapse shape. Then the plastic energy dissipation could be calculated, following the same process

used for mode 2. Finally, a simplified FSI methodology, using explicit time-stepping, could be developed, just as it was for Phase 2.

Analytic or semi-analytic solutions will always be limited to symmetric, predictable collapse modes. This is because an essential part of the analytic solution process is accurately predicting the kinematic behavior during collapse. For this reason, analytic or semi-analytic solutions cannot be used to investigate UNDEX-induced implosion, which is inherently asymmetric.

Optimization of the Flexible Cylinder Lining Concept

As discussed in Chapter 6, a flexible or energy-absorbing cylinder lining would serve to reduce the severity of the implosion pulse. The cost of this improvement will be additional weight, as well as reduction in internal usable volume of the cylinder. The lining could be optimized with regards to weight and thickness by targeting the regions of the cylinder where first contact will occur during collapse. A fully-coupled numerical simulation is required to fully evaluate the cylinder lining concept and its effectiveness in reducing the peak pressure of the implosion pulse.

Improvement of the FSI Solution

In Chapter 5, it was shown that the potential flow assumptions are valid throughout the implosion process, except for the brief instant of impact between opposite cylinder walls. The dynamic fluid pressure was estimated by neglecting the term $\frac{\partial \phi}{\partial t}$, though this assumption was not formally justified. In order to fully evaluate the fluid behavior, it is necessary to calculate the fluid potential function $\phi = \phi(x, y, z, t)$. Once the potential function is known, then the fluid velocity ($\vec{v} = \nabla\phi$) and dynamic pressure ($p_d = -\rho\left(\frac{\partial \phi}{\partial t} + \frac{1}{2} \mid \nabla\phi \mid^2\right)$) can be found at any location and time.

From potential flow theory, the governing partial differential equation (PDE) is

the Laplace equation:

$$\nabla^2\phi = \phi_{xx} + \phi_{yy} + \phi_{zz} = 0 \tag{7.1}$$

A boundary value problem (BVP) is formulated by specifying boundary conditions on the boundary of the fluid domain. In the case of underwater implosion problems, the fluid boundary is the solid cylinder surface. If the normal velocity $v_n = \frac{\partial\phi}{\partial n}$ is specified on the cylinder surface, then the BVP is of the Neumann form. A conceptual solution methodology for the Neumann BVP is outlined in the following steps:

1. Solve the structural deformation problem, assuming the loading is constant hydrostatic pressure and neglecting the effects of the fluid. The desired output is the velocity field of the structural surface. This was accomplished by the ABAQUS numerical simulation described in Chapter 3.

2. Use the surface velocity from step 1 as the boundary condition for the BVP. Solve the BVP for $\phi(x, y, z, t)$. Use ϕ to calculate the dynamic pressure, $p_d(x, y, z, t)$.

3. Add the resulting dynamic pressure function to the constant hydrostatic pressure and repeat the structural solution with the total pressure. Continue iterating until the solution converges.

Of course, the difficulty in this process is analytically solving the BVP for $\phi(x, y, z, t)$. Preliminary work was done on this problem and is presented in Appendix C. The solution was not continued in this research because of time constraints and because of uncertainty as to the usefulness of the results[1].

If deemed worthwhile, future work could be pursued to further develop an analytic solution for $\phi(x, y, z, t)$. The result could be used to 1) justify the Phase 1 dynamic pressure assumption, and 2) provide insight into the fluid behavior (velocity and pressure) at any location and time.

[1]The usefulness of an analytic solution, which will necessarily include simplifying assumptions, is questionable when fully-coupled FSI numerical simulations are available (but computationally expensive).

Appendix A

Effect of Linear Longitudinal Deformation Assumption on Energy Dissipation

In Section 2.5.3, the longitudinal deformation profile during collapse was discussed. It was assumed that the longitudinal profile is linear or triangular. In order to validate this assumption, the accuracy of the resulting energy calculation is evaluated for a specific example case.

The longitudinal deformation profile for an example cylinder at the end of Phase 1 is shown in Fig. A-1. The actual shape (from ABAQUS simulation) is plotted, along with the linear approximation and a best-fit polynomial curve. The actual shape is very closely matched by a third-order polynomial function. The linear approximation underestimates the displacement near the cylinder center, and overestimates the displacement near the cylinder ends.

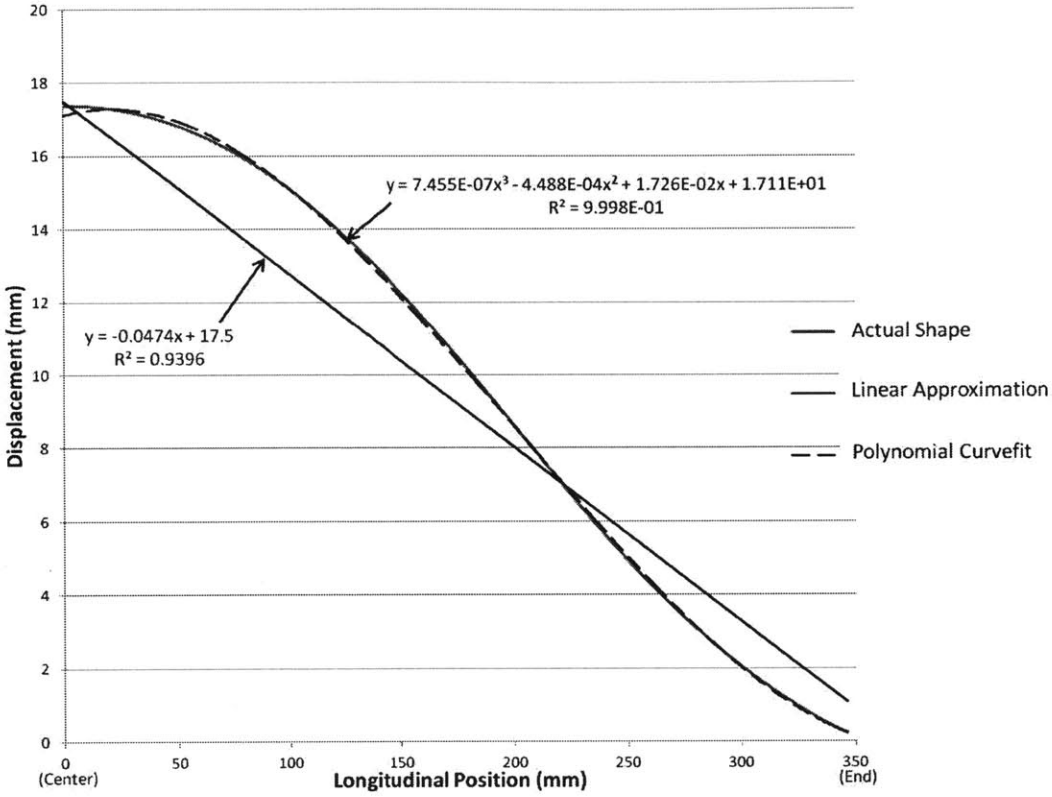

Figure A-1: Longitudinal deformation profile at the end of Phase 1 for an example cylinder.

In Chapter 4, it was demonstrated that the contribution of bending energy is much larger than membrane energy. Therefore, it is only necessary to consider bending energy to assess the accuracy of the linear profile assumption. The bending energy during Phase 1, as a function of $\alpha(x)$, was given by Eq. (4.17), repeated here:

$$E_{b,tot} = 2\int_0^L 8M_0\left(\alpha(x) - \frac{\pi}{4}\right)dx \tag{A.1}$$

where $\alpha(x)$ is dependent on the assumed longitudinal profile.

Assuming a linear longitudinal profile, the bending energy during Phase 1 was given by Eq. (4.18), repeated here:

$$E_{b,tot} = 6.22M_0L\frac{w_0}{R} \tag{A.2}$$

At the end of Phase 1, $w_0 = R$, so that $E_{b,tot} = 6.22M_0L$. If the more accurate third-order polynomial function from Fig. A-1 is used, then the total bending energy at the end of Phase 1 is given by:

$$E_{b,tot} = \frac{M_0}{R}\left(2.317 * 10^{-6}L^4 - 1.859 * 10^{-3}L^3 + 1.073 * 10^{-1}L^2 + 212.704L\right) \tag{A.3}$$

For this example cylinder, $L = 347.9$ mm and $R = 19.07$ mm. Substituting these values into Eqs. (A.2) and (A.3) gives the following results:

Table A.1: Effect of longitudinal profile on Phase 1 bending energy.

Linear Profile	$E_{b,tot} = 2164M_0$
Cubic Profile	$E_{b,tot} = 2237M_0$
Percent Difference	3.4%

Appendix B

Significance of Internal Air

In order to determine the significance of E_{air} in the overall energy balance of implosion, an example problem is considered. The specific example is the cylinder represented in Fig. 4-18a, with the following dimensions: R=12.7 mm, L=137.3 mm, and h=0.889 mm. For this cylinder, the total plastic energy dissipation (from the semi-analytic solution) is 550 J (Table 4.7). The energy required to compress the internal air (assuming adiabatic compression) is found from Eq. (2.32), repeated here:

$$E_{air,adiabatic} = \frac{p_{i_0} V_0}{\gamma - 1} \left[\left(\frac{V_0}{V} \right)^{\gamma - 1} - 1 \right] \tag{B.1}$$

For this example, $p_{i_0} = 0.1$ MPa, $V_0 = 138,235$ mm^3, and $V = 14,597$ mm^3. Substituting these values into Eq. (B.1) gives:

$$E_{air} = 50.4\text{J} \tag{B.2}$$

Thus, for this example:

$$\frac{E_{air}}{E_{int}} = \frac{50.4}{550} = 9.2\% \tag{B.3}$$

An alternative way to evaluate the significance of internal air is to look at the kinetic energy history for an implosion event. Figure B-1 shows the kinetic energy

history for an example implosion, both with and without the inclusion of internal air.

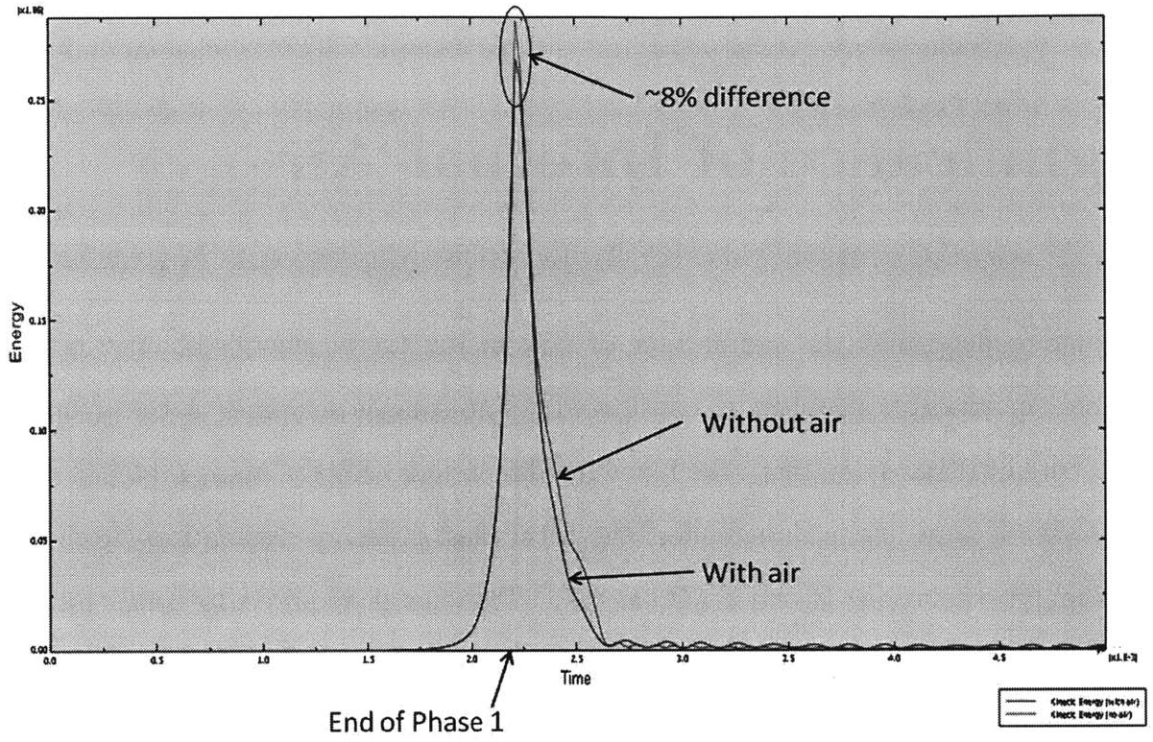

Figure B-1: Effect of internal air on kinetic energy.

The figure shows that the internal air reduces the peak kinetic energy of the system by about 8%. In effect, the air acts as a damper to slow the collapse of the cylinder, which in turn will reduce the magnitude of the implosion pulse. In Chapter 5, it was demonstrated that the peak kinetic energy of the system is about equal to the energy of the implosion pulse. Therefore, neglecting the internal air will result in overestimating the pulse energy by about 8%.

It should be noted that the analysis in this appendix assumes an initial internal air pressure of 1 atmosphere (0.1 MPa). The magnitude of E_{air} can be increased by increasing the initial pressure or by using a gas other than air, as discussed in section 6.2.

Appendix C

Analytic Solution for $\phi(x, y, z, t)$

Assuming potential flow conditions exist, the potential function $\phi(x, y, z, t)$ satisfies the Laplace equation:

$$\nabla^2\phi = \phi_{xx} + \phi_{yy} + \phi_{zz} = 0 \tag{C.1}$$

subject to the boundary condition $\nabla\phi = \vec{v}$ on the cylinder surface. In order to make the problem tractable, the 3D geometry of the cylinder is projected onto a 2D (x-y) plane, and all displacement and velocity is assumed to be normal to the plane (i.e., in the z direction). The domain $D(x, y, t)$ defines the region of the cylinder projection, or more specifically the region of non-zero velocity, on the x-y plane ($-L \leq x \leq L$, $-R \leq y \leq R$). The domain is a function of time because after the instant of first contact, there is an expanding region of zero velocity in the center of the cylinder.

The boundary condition can then be expressed as:

$$\phi_z|_{z=0} = \begin{cases} F(x, y, t) \text{ on } D(x, y, t) \\ 0 \text{ otherwise} \end{cases} \tag{C.2}$$

where $F(x, y, t)$ is the normal velocity of the projected cylinder surface. This bound-

ary value problem has the following general solution:

$$\phi(x,y,z,t) = \iint_{-\infty}^{\infty} \tilde{\phi}_{(k_x,k_y,t)} e^{i(k_x x + k_y y)} e^{-\sqrt{k_x^2+k_y^2}z} dk_x dk_y \tag{C.3}$$

Applying this general solution, the boundary condition becomes:

$$\phi_z|_{z=0} = \iint_{-\infty}^{\infty} -\sqrt{k_x^2+k_y^2}\tilde{\phi}_{(k_x,k_y,t)} e^{i(k_x x + k_y y)} dk_x dk_y \tag{C.4}$$

In order to evaluate the coefficients $\tilde{\phi}_{(k_x,k_y,t)}$, we make use of the Fourier transform integral. The general form of the Fourier transform integral is:

$$g(x,y) = \left(\frac{1}{2\pi}\right)^2 \iint_{-\infty}^{\infty} G(k_x,k_y) e^{i(k_x x + k_y y)} dk_x dk_y \tag{C.5}$$

The inverse Fourier transform integral is:

$$G(k_x,k_y) = \iint_{-\infty}^{\infty} g(x,y) e^{-i(k_x x + k_y y)} dx dy \tag{C.6}$$

In this case,

$$G(k_x,k_y) = -\sqrt{k_x^2+k_y^2}\tilde{\phi}_{(k_x,k_y,t)} \tag{C.7}$$

and

$$(2\pi)^2 g(x,y) = \begin{cases} F(x,y,t) \text{ on } D(x,y,t) \\ 0 \text{ otherwise} \end{cases} \tag{C.8}$$

Therefore:

$$-\sqrt{k_x^2+k_y^2}\tilde{\phi}_{(k_x,k_y,t)} = \left(\frac{1}{2\pi}\right)^2 \iint_{\mathbf{D}} F(x,y,t) e^{-i(k_x x + k_y y)} dx dy \tag{C.9}$$

or

$$\tilde{\phi}_{(k_x,k_y,t)} = -\frac{1}{4\pi^2\sqrt{k_x^2+k_y^2}} \iint_{\mathbf{D}} F(x,y,t) e^{-i(k_x x + k_y y)} dx dy \tag{C.10}$$

Substituting this expression into the general solution gives:

$$\phi(x,y,z,t) = \iint_{-\infty}^{\infty} -\frac{1}{4\pi^2\sqrt{k_x^2+k_y^2}} \left[\iint_{\mathbf{D}} F(\acute{x},\acute{y},t)e^{-i(k_x\acute{x}+k_y\acute{y})}d\acute{x}d\acute{y}\right] e^{i(k_xx+k_yy)}e^{-\sqrt{k_x^2+k_y^2}z}dk_xdk_y \tag{C.11}$$

If $F(x,y,t)$ is known from the structural deformation solution, then Eq. (C.11) can be evaluated for $\phi(x,y,z,t)$.

The infinite integrals in Eq. (C.11) can be bounded to the range over which k_x and k_y are significant. In order to determine this range, the integral

$$\int_{-L}^{L}\int_{-R}^{R} Fe^{-i(k_xx+k_yy)}dxdy$$

must be evaluated over a range of k_x and k_y. To evaluate the integral, the following simple function was chosen for $F(x,y,t)$:

$$F(x,y,t) = \left[1-\left(\frac{x}{L}\right)^2\right]\left[1-\left(\frac{y}{R}\right)^2\right](At^2+Bt) \tag{C.12}$$

This function is a simplification of the actual velocity profiles obtained using the ABAQUS numerical simulation. The integral was numerically evaluated over the range $-\frac{10}{L} \le k_x \le \frac{10}{L}$ and $-\frac{10}{R} \le k_y \le \frac{10}{R}$, and the results are plotted in Fig. C-1.

The plot shows that the value of the integral is only significant when $|k_x| \le \frac{10}{L}$ and $|k_y| \le \frac{2}{R}$. Thus, the infinite integrals in Eq. (C.11) may be replaced with these limits.

The time dependence of $F(x,y,t)$ does not appear in the general solution for ϕ, so the spatial and temporal dependencies may be separated as follows:

$$\phi(x,y,z,t) = \phi(x,y,z)T(t) \tag{C.13}$$

where $T(t)$ is determined (or approximated) from the structural solution.

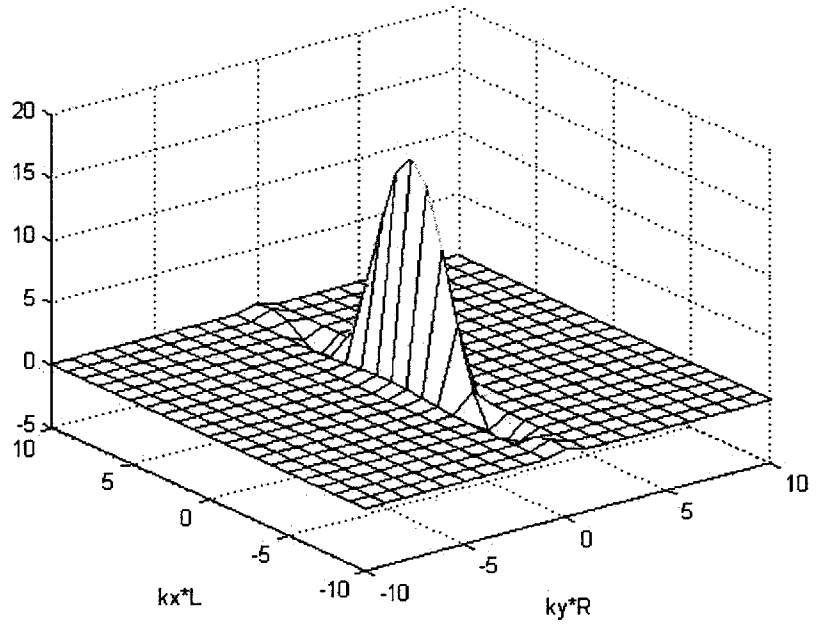

Figure C-1: Range of significance of k_x and k_y.

Improved Boundary Condition

The function $F(x, y, t)$ describes the velocity of point (x,y,0) with respect to time. The function is valid until the time when the velocity of that point becomes 0 (because of contact). In order to make the solution valid over the period of contact, the Heaviside step function is introduced.

$$H(x) = \begin{cases} 0, & x < 0 \\ 1, & x \geq 0 \end{cases} \tag{C.14}$$

The Heaviside step function can be smoothly approximated by:

$$H(x) \approx \frac{1}{1 + e^{-2kx}} \tag{C.15}$$

where k is a constant defining the sharpness of the step transition (a larger value of k represents a sharper step transition at x=0).

If $\tau^*(x,y)$ is a function that defines the time of contact for point (x,y,0), so that $\tau^*(0,0)$=the time of first contact at the center of the cylinder (i.e., the end of Phase 1), then the boundary condition, Eq. (C.2), can be written as:

$$\phi_z(x,y,0,t) = F(x,y,t)\left[1 - H(t-\tau^*(x,y))\right] = F(x,y,t)\left[1 - \frac{1}{1+e^{-2k(t-\tau^*(x,y))}}\right] \tag{C.16}$$

The general solution for $\phi(x,y,z,t)$ is then:

$$\phi(x,y,z,t) = \int_{-\frac{2}{R}}^{\frac{2}{R}} \int_{-\frac{10}{L}}^{\frac{10}{L}} -\frac{1}{4\pi^2\sqrt{k_x^2+k_y^2}} \left[\iint_{\mathbf{D}} F(\acute{x},\acute{y},t)\left[1 - \frac{1}{1+e^{-2k(t-\tau^*(\acute{x},\acute{y}))}}\right] * \ldots \right.$$
$$\left. \ldots * e^{-i(k_x\acute{x}+k_y\acute{y})} d\acute{x}d\acute{y}\right] e^{i(k_x x+k_y y)} e^{-\sqrt{k_x^2+k_y^2}z} dk_x dk_y \tag{C.17}$$

where:

- $F(x,y,t) = \phi_z|_{z=0}$ on $\mathbf{D}$
- $\tau^*(x,y)$ = function that defines when $\phi_z|_{x,y,0} = 0$
- k = factor that defines the sharpness of the step transition to zero velocity

The factor k is directly related to the stiffness or flexibility of the cylinder inner surface (see Section 6.3 for a discussion on use of flexible cylinder linings). Figure C-2 plots the approximate Heaviside step function (Eq. (C.15)) for several values of k. In order to evaluate Eq. (C.17), a value of k must be chosen that is appropriate to the physical conditions of the actual cylinder.

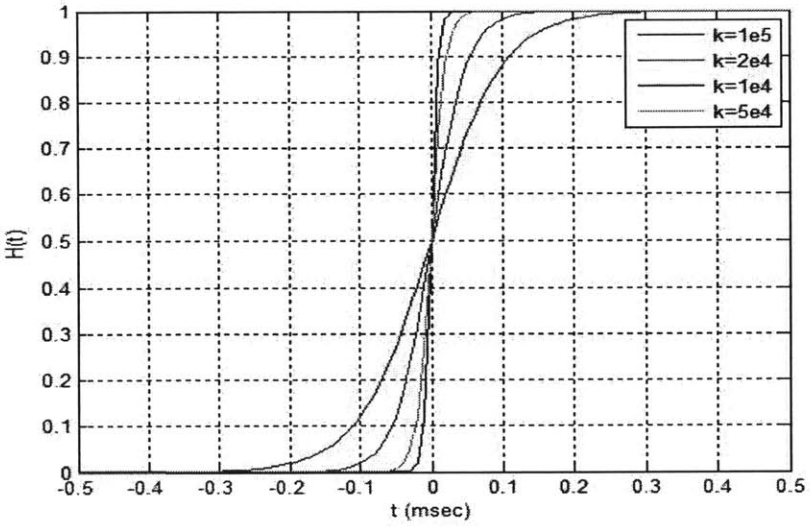

Figure C-2: Heaviside step function for various values of k.

Appendix D

MATLAB Listings

Cylinder Critical Pressure

```
%Pcrit.m

%Calculates and plots the quasistatic critical pressure (Pc) as a ...
    function of w0

clear
%User Inputs
sigma=351;%material flow stress (MPa)
R=12.7;%cylinder radius (mm)
L=137.3;%cylinder length (mm)
t=0.889;%cylinder thickness (mm)
Pext=6.73;%external hydrostatic pressure (MPa)
P0=0.1;%initial internal air pressure (MPa)

M=sigma*t^2/4;%fully plastic bending moment
N=sigma*t;%fully plastic membrane force
```

```
w=[.1:.01:R];

Pc1=-(6.22*M*L/R)/(2.574*R^3*L)./((cos(pi/2*w/R)*pi/2/R.*w-sin(pi/2*w...
    /R))./w.^2);%Pc due to bending energy
Pc2=-(.491*8*w/L*N*R)/(2.574*R^3*L)./((cos(pi/2*w/R)*pi/2/R.*w-sin(pi...
    /2*w/R))./w.^2);%Pc due to membrane energy
Pc3=P0*(2*pi./(2*pi-4+2.574*sin(pi/2*w/R)./(w/R))).^1.4;%Pc due to ...
    air compression

Pc=Pc1+Pc2+Pc3;%Total Pcrit

%Non-dimensional critical pressure
Pc1bar=Pc1*R^2/sigma/t^2;
Pc2bar=Pc2*R^2/sigma/t^2;
Pc3bar=Pc3*R^2/sigma/t^2;
Pcbar=Pc*R^2/sigma/t^2;

wbar=w/R;

i=find(Pc<Pext,1);%index of Pc corresponding to first value < Pext

%Plot results
figure(1)
plot(wbar(i:length(wbar)),Pc1(i:length(Pc1)),'r--',wbar(i:length(wbar...
    )),Pc2(i:length(Pc2)),'b-.',wbar(i:length(wbar)),Pc3(i:length(Pc3...
    )),'c:',wbar(i:length(wbar)),Pc(i:length(Pc)),'k-')
xlabel('w0/R')
ylabel('Pc (MPa)')
legend('Eb','Em','Eair','Total')
title('Quasistatic Pc during Phase 1')
```

Explicit Time-Stepping Procedure

```
%pres_it.m

%Routine to calculate and plot iterative steps of P and Pc during ...
   Phase 1
%units:length=mm, pressure=MPa, time=sec, density=tonne/mm^3
%Assumes constant acceleration, a=(P-Pc)/m, over each time interval ...
   delta t

clear
clf

%User inputs
L=137.3;%cylinder length
R=12.7;%cylinder radius
h=0.889;%cylinder thickness
sigma=351;%material flow stress (MPa)
M=sigma*h^2/4;%fully plastic bending moment
N=sigma*h;%fully plastic membrane force

%Iterative calcs are done with and without added mass.  Variables ...
   with 'a' include added mass
delt=.0000001;  %time step delta t (sec)
roh=1e-9;%density of water (tonne/mm^3)
rohs=2.7e-9;%density of cylinder material (tonne/mm^3)
m=rohs*h;%mass/area of cylinder material (tonne/mm^2)
ma=rohs*h+roh*pi/4;%mass/area of cylinder material + added mass of ...
   water(tonne/mm^2)
Pint=0.1;%initial internal air pressure (MPa)
```

```
w(1)=1.61;%initial deflection, to account for fact that Pc goes to ...
    infinity at w=0 (i value from Pcrit.m)
wa(1)=w(1);%initial deflection with added mass included
wdot(1)=0;%initial velocity
wadot(1)=0;%initial velocity with added mass

Pd(1)=-roh/2*wdot(1)^2;%initial dynamic pressure
Pad(1)=-roh/2*wadot(1)^2;

P(1)=6.73;%initial external pressure (MPa)
Pa(1)=6.73;
Pc(1)=(-6.22*M*L/R-.491*8*N*R/L*w(1))/(2.574*R^3*L*(cos(pi/2*w(1)/R)*...
    pi/2/R*w(1)-sin(pi/2*w(1)/R))/w(1)^2)+Pint*(2*pi*w(1)/R/(2*pi-4+2...
    .574*sin(pi/2*w(1)/R)))^1.4;%cylinder critical pressure
Pac(1)=(-6.22*M*L/R-.491*8*N*R/L*wa(1))/(2.574*R^3*L*(cos(pi/2*wa(1)/...
    R)*pi/2/R*wa(1)-sin(pi/2*wa(1)/R))/wa(1)^2)+Pint*(2*pi*wa(1)/R...
    /(2*pi-4+2.574*sin(pi/2*wa(1)/R)))^1.4;

t(1)=0;
ta(1)=0;

KE(1)=0;%kinetic energy
KEdot(1)=0;
We(1)=0;%external work
Wedot(1)=0;

KEa(1)=0;
KEadot(1)=0;
Wea(1)=0;
Weadot(1)=0;

%iterations without added mass
for i=2:50000;
```

```
    t(i)=t(i-1)+delt*1000;%t=msec
    w(i)=w(i-1)+wdot(i-1)*delt+delt^2/2*(P(i-1)-Pc(i-1))/m;%...
        displacement at step i
    KE(i)=KE(i-1)+(KEdot(i-1)*delt)/1000;%KE=Joules
    We(i)=We(i-1)+Wedot(i-1)*delt/1000;
    if w(i)>=R%check if contact has occurred yet
        break
    else
    wdot(i)=wdot(i-1)+delt*(P(i-1)-Pc(i-1))/m;%velocity at step i

    Pd(i)=-roh/2*wdot(i)^2;%dynamic pressure at step i
    P(i)=P(1)+Pd(i);
    Pc(i)=(-6.22*M*L/R-.491*8*N*R/L*w(i))/(2.574*R^3*L*(cos(pi/2*w(i)...
        /R)*pi/2/R*w(i)-sin(pi/2*w(i)/R))/w(i)^2)+Pint*(2*pi/(2*pi...
        -4+2.574*sin(pi/2*w(i)/R)/(w(i)/R)))^1.4;

    V(i)=R^2*L*(2*pi-4+2.574*sin(pi/2*w(i)/R)/(w(i)/R));%cylinder ...
        volume at step i
    Vdot(i)=2.574*R^3*L*wdot(i)/w(i)^2*(pi/2*w(i)/R*cos(pi/2*w(i)/R)-...
        sin(pi/2*w(i)/R));
    KEdot(i)=-(P(i)-Pc(i))*Vdot(i);
    Wedot(i)=-P(i)*Vdot(i);
    end
end

%iterations with added mass
for i=2:50000;
    ta(i)=ta(i-1)+delt*1000;
    wa(i)=wa(i-1)+wadot(i-1)*delt+delt^2/2*(Pa(i-1)-Pac(i-1))/ma;%...
        displacement at step i
    Epa(i)=(6.22*M*(wa(i)-wa(1))/R*L+.2455*8*N*R/L*(wa(i)-wa(1))^2)...
        /1000;%total plastic energy dissipated (J)(subtract initial ...
        wa, because it is elastic)
```

```
    Eair(i)=1/.4*Pint*2*pi*R^2*L*((2*pi/(2*pi-4+2.574*sin(pi/2*wa(i)/...
        R)/wa(i)*R))^.4-1)/1000;%energy required to compress air
    KEa(i)=KEa(i-1)+(KEadot(i-1)*delt)/1000;%KE=Joules (includes ...
        energy of both solid and water)
    Wea(i)=Wea(i-1)+Weadot(i-1)*delt/1000;
    if wa(i)>=R%check if contact has occurred yet
        break
    else
    wadot(i)=wadot(i-1)+delt*(Pa(i-1)-Pac(i-1))/ma;%velocity at step ...
        i
    Pad(i)=-roh/2*wadot(i)^2;%dynamic pressure at step i
    Pa(i)=Pa(1)+Pad(i);
    Pac(i)=(-6.22*M*L/R-.491*8*N*R/L*wa(i))/(2.574*R^3*L*(cos(pi/2*wa...
        (i)/R)*pi/2/R*wa(i)-sin(pi/2*wa(i)/R))/wa(i)^2)+Pint*(2*pi...
        /(2*pi-4+2.574*sin(pi/2*wa(i)/R)/(wa(i)/R)))^1.4;
    Va(i)=R^2*L*(2*pi-4+2.574*sin(pi/2*wa(i)/R)/(wa(i)/R));%cylinder ...
        volume at step i
    Vadot(i)=2.574*R^3*L*wadot(i)/wa(i)^2*(pi/2*wa(i)/R*cos(pi/2*wa(i...
        )/R)-sin(pi/2*wa(i)/R));
    KEadot(i)=-(Pa(i)-Pac(i))*Vadot(i);
    Weadot(i)=-Pa(i)*Vadot(i);
    end
end

deltaV=Va(2)-Va(length(Va));%total change in volume
Wextmax=deltaV*Pa(1)/1000%external work, assuming constant P

KEsum=Wea-Epa-Eair;

%Numerical simulation data, for comparison
tNUWC=[0+.052:.05:.35+.052];%shifted by 0.052 to best match analytic ...
    solution
pNUWC=[6.73 6.58 6.3 5.54 4.25 2.74 1.96 1.85];
```

```
%various plots of results

figure(1)
plot(w(1:length(w)-1),Pc,'k',w(1:length(w)-1),P,'b--',wa(1:length(wa)...
   -1),Pa,'r-.')
xlabel('w (mm)')
ylabel('P (MPa)')
legend('Pc','P (without added mass)','P (with added mass)')
grid on

figure(2)
plot(t(1:length(t)-1),Pc,'k',t(1:length(t)-1),P,'b--')
xlabel('t (msec)')
ylabel('P (MPa)')
legend('Pc','P')
title('Without added mass')
grid on

figure(3)
plot(wa(1:length(wa)-1),Pac,'r',wa(1:length(wa)-1),Pa,'b')
xlabel('w (mm)')
ylabel('P (MPa)')
legend('Pc','P')
title('With added mass')
grid on

figure(4)
plot(ta(1:length(ta)-1),Pa,'b-',tNUWC,pNUWC,'r--')
xlabel('t (msec)')
ylabel('P (MPa)')
legend('Analytic','Numerical')
grid on
```

```
figure(5)
plot(ta,Wea,'r',ta,KEa,'b')
xlabel('t (msec)')
ylabel('Energy (J)')
legend('Wext','KE','Location','NorthWest')
title('With added mass')
grid on

figure(6)
plot(wa,Wea,'k-',wa,Epa,'r-.',wa,KEsum,'b--',wa,Eair,'m:')
xlabel('w (mm)')
ylabel('Energy (J)')
legend('W','Eint','KE','Eair','Location','NorthWest')
text(6.2,95,'W=Eint+Eair+KE')
axis([0 14 0 110])
grid on
```

Bibliography

[1] R. S. Price and V. K. Shuler, "Sounds from implosions of steel cylinders under water," Tech. Rep. NOLTR 74-168, Naval Ordnance Laboratory White Oak, Sep 1974.

[2] M. Diwan, "Underwater implosions of large format photo-multiplier tubes," *Nuclear Instruments and Methods in Physics Research, Section A: Accelerators, Spectrometers, Detectors and Associated Equipment*, vol. 670, pp. 61–7, 2012.

[3] S. Kyriakides, "Implosion experiments." Presentation at ONR Implosion Program Review, Apr 2011.

[4] M. S. Suh, *Plastic analysis of dented tubes subjected to combined loading.* PhD thesis, Massachusetts Institute of Technology, May 1987.

[5] A. C. Palmer and J. H. Martin, "Buckle propagation in submarine pipelines," *Nature*, vol. 254, no. 5495, pp. 46–48, 1975.

[6] L. Rayleigh, "On the pressure developed in a liquid during the collapse of a spherical cavity," *Phil.Mag*, vol. 34, no. 200, pp. 94–98, 1917.

[7] J. D. Isaacs and A. E. Maxwell, "The ball-breaker, a deep water bottom signalling device," *J.Marine Res*, vol. 11, pp. 63–68, 1952.

[8] R. J. Urick, "Implosions as sources of underwater sound," *Journal of the Acoustical Society of America*, vol. 35, no. 12, pp. 2026–2027, 1963.

[9] S. Fukuda, Y. Fukuda, and T. Hayakawa, "The super-kamiokande detector," *Nuclear Instruments and Methods in Physics Research, Section A: Accelerators, Spectrometers, Detectors and Associated Equipment*, vol. 501, p. 418, 2003.

[10] T. Wierzbicki and S. U. Bhat, "Initiation and propagation of buckles in pipelines," *Int.J.Solids Struct.(UK)*, vol. 22, no. 9, p. 985, 1986.

[11] S. Kyriakides, M. K. Yeh, and D. Roach, "On the determination of the propagation pressure of long circular tubes," *Transactions of the ASME Journal of Pressure Vessel Technology*, vol. 106, pp. 150–9, May 1984.

[12] M. S. HooFatt and T. Wierzbicki, "Damage of plastic cylinders under localized pressure loading," *Int.J.Mech.Sci.(UK)*, vol. 33, no. 12, p. 999, 1991.

[13] M. S. HooFatt, *Deformation and rupture of cylindrical shells under dynamic loading.* PhD thesis, Massachusetts Institute of Technology, June 1992.

[14] J. J. Cor and T. F. Miller, "Theoretical analysis of hydrostatic implodable volumes with solid inner structures," *Journal of Fluids and Structures*, vol. 25, no. 2, pp. 284–303, 2009.

[15] J. J. Cor and T. F. Miller, "Theoretical analysis of hydrostatic implodable cylindrical volumes with solid inner structures," *Journal of Fluids and Structures*, vol. 26, no. 2, pp. 253–273, 2010.

[16] S. E. Turner, "Underwater implosion of glass spheres," *Journal of the Acoustical Society of America*, vol. 121, pp. 844–852, 2007.

[17] J. M. Brett and G. Yiannakopolous, "A study of explosive effects in close proximity to a submerged cylinder," *International Journal of Impact Engineering*, vol. 35, no. 4, pp. 206–225, 2008.

[18] C. F. Hung, B. J. Lin, J. Hwang-Fuu, and P. Y. Hsu, "Dynamic response of cylindrical shell structures subjected to underwater explosion," *Ocean Engineering*, vol. 36, no. 8, pp. 564–577, 2009.

[19] R. H. Cole, *Underwater explosions.* New York: Dover Publications, 1965.

[20] M. Moubachir and J.-P. Zolesio, *Moving Shape Analysis and Control : Applications to Fluid Structure Interactions.* Boca Raton, FL: Chapman and Hall/CRC, 2006.

[21] L. G. Olson and K. J. Bathe, "Analysis of fluid-structure interactions. a direct symmetric coupled formulation based on the fluid velocity potential," *Computers and Structures*, vol. 21, no. 1-2, pp. 21–32, 1985.

[22] J. Mackerle, "Fluid-structure interaction problems, finite element and boundary element approaches: A bibliography (1995-1998)," *Finite Elements in Analysis and Design*, vol. 31, no. 3, pp. 231–240, 1999.

[23] R. van Loon, P. D. Anderson, F. N. van de Vosse, and S. J. Sherwin, "Comparison of various fluid-structure interaction methods for deformable bodies," *Computers and Structures*, vol. 85, no. 11-14, pp. 833–843, 2007.

[24] Department of the Navy, *Joint Fleet Maintenance Manual (COMFLTFORCOMINST 4790 REV A CH-6)*, 2011.

[25] A. S. D. Rallu, *A multiphase fluid-structure computational framework for underwater implosion problems.* PhD thesis, Stanford University, June 2009.

[26] S. E. Turner and J. M. Ambrico, "Underwater implosion of cylindrical metal tubes," *Journal of Applied Mechanics*, vol. 80, p. 011013 (11 pp.), Jan 2013.

[27] A. M. Beese, M. Luo, Y. Li, Y. Bai, and T. Wierzbicki, "Partially coupled anisotropic fracture model for aluminum sheets," *Engineering Fracture Mechanics*, vol. 77, p. 1128, May 2010.

[28] T. Wierzbicki and M. S. HooFatt, "Damage assessment of cylinders due to impact and explosive loading," *International Journal of Impact Engineering*, vol. 13, no. 2, p. 215, 1993.

[29] S. U. Bhat and T. Wierzbicki, "Length of the transition zone in unconfined buckle propagation," *Journal of Offshore Mechanics and Arctic Engineering*, vol. 109, no. 2, pp. 155–162, 1987.

[30] J. Y. Dyau and S. Kyriakides, "On the localization of collapse in cylindrical shells under external pressure," *International Journal of Solids and Structures*, vol. 30, no. 4, pp. 463–482, 1993.

[31] S. Kyriakides and T. A. Netto, "On the dynamics of propagating buckles in pipelines," *International Journal of Solids and Structures*, vol. 37, no. 46-47, pp. 6843–6867, 2000.

[32] Dassault Systemes Simulia Corp., Providence, RI, *Abaqus Analysis User's Manual: Section 11.6 Surface-based fluid modeling*, 6.10 ed., 2010.

[33] Dassault Systemes Simulia Corp., Providence, RI, *Abaqus Analysis User's Manual: Section 30.4.5 Acoustic and shock loads*, 6.10 ed., 2010.

[34] T. Wierzbicki and W. Abramowicz, "On the crushing mechanics of thin-walled structures," *Journal of Applied Mechanics, Transactions ASME*, vol. 50, no. 4 a, p. 727, 1983.

[35] J. N. Newman, *Marine Hydrodynamics*. Cambridge, MA: Massachusetts Institute of Technology, 1977.

[36] R. E. Chamberlin, "Investigation of the fundamental drivers in implosion dynamics." Presentation at ONR Implosion Program Review, Dec 2012.